Coevolutionary Dynamics in Structured Populations of Three Species

Bartosz Szczesny

Department of Applied Mathematics

University of Leeds

Submitted in accordance with

the requirements for the degree of

Doctor of Philosophy

May 2014

The candidate confirms that the work submitted is his/her own, except where work which has formed part of jointly authored publications has been included. The contribution of the candidate and the other authors to this work has been explicitly indicated below. The candidate confirms that appropriate credit has been given within the thesis where reference has been made to the work of others.

Contents of Chapters 2, 4 and 5 appear in jointly authored publications:

Szczesny, B., Mobilia, M. & Rucklidge, A.M.,
When does cyclic dominance lead to stable spiral waves?,
EPL, **102**, 28012 (2013).

Szczesny, B., Mobilia, M. & Rucklidge, A.M.,
Characterization of spiraling patterns in spatial rock–paper–scissors games,
PRE, **90**, 032704 (2014).

The co-authors contributed to writing of the above publications and to analysis and discussion of the results obtained by the candidate.

Szolnoki, A., Mobilia, M., Jiang, L.L.,
Szczesny, B., Rucklidge, A.M. & Perc, M.,
Cyclic dominance in evolutionary games: A review,
accepted to *Journal of the Royal Society Interface*, (2014).

Work directly attributable to the candidate can be found in Sections III.B-D of the above review publication. The candidate, MM and ARM discussed the structure and contents of Sections III.B-D written by MM.

Acknowledgements

To my supervisors, Mauro Mobilia and Alastair M. Rucklidge,
for guidance through the puzzling world of academic research.

To Steve Tobias, for advice on the Ginzburg–Landau equation.

To Tobias Galla, for collaboration on early stages of the project.

Sections of this research were undertaken on ARC1, part of the
high performance computing facilities at the University of Leeds.

Abbreviations

AI	absolute instability (phase)
BS	bound states (phase)
CGLE	complex Ginzburg-Landau equation
ETD	exponential time differencing
ETD1	exponential time differencing of 1st order
ETD2	exponential time differencing of 2nd order
EI	Eckhaus instability (phase)
GPL	GNU Public License
JPEG	joint photographic experts group
LMC	lattice Monte Carlo
MIT	Massachusetts Institute of Technology
ODE	ordinary differential equation
PDE	partial differential equation
PNG	portable network graphics
PPM	portable pixel map
RPS	rock-paper-scissors
SA	spiral annihilation (phase)

Abstract

Inspired by the experiments with the three strains of *E. coli* bacteria as well as the three morphs of *Uta stansburiana* lizards, a model of cyclic dominance was proposed to investigate the mechanisms facilitating the maintenance of biodiversity in spatially structured populations. Subsequent studies enriched the original model with various biologically motivated extension repeating the proposed mathematical analysis and computer simulations.

The research presented in this thesis unifies and generalises these models by combining the birth, selection-removal, selection-replacement and mutation processes as well as two forms of mobility into a generic metapopulation model. Instead of the standard mathematical treatment, more controlled analysis with inverse system size and multiscale asymptotic expansions is presented to derive an approximation of the system dynamics in terms of a well-known pattern forming equation. The novel analysis, capable of increased accuracy, is evaluated with improved numerical experiments performed with bespoke software developed for simulating the stochastic and deterministic descriptions of the generic metapopulation model.

The emergence of spiral waves facilitating the long term biodiversity is confirmed in the computer simulations as predicted by the theory. The derived conditions on the stability of spiral patterns for different values of the biological parameters are studied resulting in discoveries of interesting phenomena such as spiral annihilation or instabilities caused by nonlinear diffusive terms.

Contents

Figures

FIGURES

Listings

Tables

Chapter 1

Introduction

> Over 90 percent (...) of all the species that have ever lived (...) on this planet are (...) extinct. We didn't kill them all.
>
> George Carlin

This chapter contains a broad introduction of the biological motivations behind the postgraduate research presented in this thesis. More technical introductions of the mathematical and computational methods can be found in Chapters 2 and 3 dedicated to those subjects. This introductory chapter concludes by summarising the analytical and numerical improvements made over previous studies with the resulting discoveries of novel phenomena.

1.1 Cyclic Dominance in Structured Populations

The 125th anniversary of Science magazine was celebrated by a publication of articles discussing the 125 most compelling questions facing scientists. One of the top 25 questions featured in that special collection asked "What Determines Species Diversity?" (Pennisi, 2005) with excerpts from the article given below.

1. INTRODUCTION

> Countless species of plants, animals, and microbes fill every crack and crevice on land and in the sea. (...) In some places and some groups, hundreds of species exist, whereas in others, very few have evolved (...). Biologists are striving to understand why. The interplay between environment and living organisms and between the organisms themselves play key roles in encouraging or discouraging diversity (...). But exactly how these and other forces work together to shape diversity is largely a mystery. (...) Future studies should continue to reveal large-scale patterns of distribution and perhaps shed more light on the origins of mass extinctions and the effects of these catastrophes on the evolution of new species. From field studies of plants and animals, researchers have learned that habitat can influence morphology and behavior (...), for example, as separated populations become reconnected, homogenizing genomes that would otherwise diverge. Molecular forces, such as low mutation rates (...) influence the rate of speciation, and in some cases, differences in diversity can vary within an ecosystem: edges of ecosystems sometimes support fewer species than the interior.

Biological diversity, or biodiversity, is often interpreted as the measure of variation of genes expressed in the number of unique life forms in current existence (Harper & Hawksworth, 1994). A large number of organisms found in a biodiverse habitat forms the components of a system in which different species interact through exchange of organic matter and energy. If such interactions between the biological agents are understood as a complex system, the biodiversity can be considered as a mechanism which supports the existence of life by increasing the adaptability to changes in the ecosystem (Darwin, 1859; Harper & Hawksworth, 1994). When the cumulative gene pool becomes depleted through an extinction of species, some of the biological diversity is lost, with the evolutionary solutions to successful survival in certain environmental conditions becoming no longer accessible. On the other hand, it is also advantageous to remove the unsuccessful strategies from the gene pool by the elimination of some species which makes extinctions a natural process of self-correction. What should be considered is

Figure 1.1: Mutually exclusive interactions self-organise lichen in the tundra to a state of high biodiversity in a form of a spiral wave. Reproduced from [BiophysikBildergalerie], see Mathiesen *et al.* (2011) for details.

the rate at which such processes are occurring in order to avoid mass extinctions which are usually an effect of natural disasters or rapid changes in the climate.

The notion that the next mass extinction is likely to be caused by human impact on the environment has gained a lot of attention in recent years with much talk about sustainability and calls for ecosystem engineering (Cardinale *et al.*, 2012; Chapin III *et al.*, 2000; Myers *et al.*, 2000). While noble in nature, these issues originate mainly from the fear of potential negative effects which loss of biodiversity can have on humanity. The gradual disappearance of the so-called "ecosystem services", such as food, fuel or climate regulation, seems to be the greatest concern amongst the majority of conservationists. This is certainly true in the case of insects whose extinctions are not widely reported (Dunn, 2005) except for some species which, coincidentally, happen to play a major role in pest control and crop pollination.

Amongst the many mechanism of maintenance of biodiversity (Chesson, 2000), cyclic dominance was proposed as a facilitator of species coexistence in ecosystems (Claussen & Traulsen, 2008; Dawkins, 1989; May & Leonard, 1975). In such situations, the species form a circular chain of interactions by dominating and being dominated at the same time. These processes are similar to those of the paradigmatic rock-paper-scissors (RPS) game in which rock crushes scissors, scissors cut paper and paper wraps rock. Such mutually exclusive interaction are

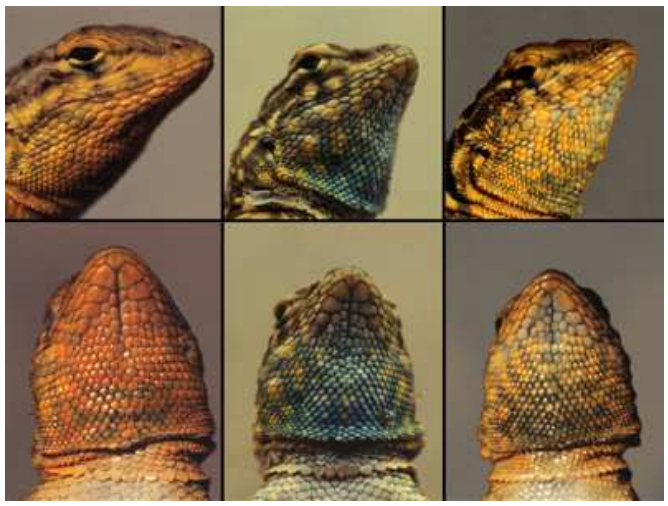

Figure 1.2: Orange, blue and yellow throat colouring in *Uta stansburiana* lizards. See caption of Figure 1.3 for description of mating behaviour. Reproduced from [LizardLand].

found to increase the biological diversity in habitats constrained to two spatial dimensions as shown in Figure 1.1 (Boerlijst & van Ballegooijen, 2010; Cameron *et al.*, 2009; Heilmann *et al.*, 2010; Mathiesen *et al.*, 2011). In particular, real-life examples of structured populations of three-species were reported in Californian lizards *Uta stansburiana*, depicted in Figure 1.2, which exhibit competitive rock-paper-scissors dynamics (Corl *et al.*, 2010; Dickinson & Koenig, 2003; Sinervo & Lively, 1996; Sinervo *et al.*, 2000; Smith, 1996; Zamudio & Sinervo, 2000). The peculiar mating habits of the side-blotched lizards gained a lot of attention, eventually making their way into the popular culture as shown in Figure 1.3.

While the field studies on the lizards proved the existence of cyclic dominance between three species in nature, they were also time consuming with an oscillatory time period of approximate four years (Sinervo & Lively, 1996). A more controlled experiment, involving time and length scales suitable for laboratory work, could enable a convenient way to study such dynamics. Fortunately, with recent advancements in microbial sciences, a similar rock-paper-scissors behaviour was found in the communities of *E. coli* bacteria (Kerr *et al.*, 2002, 2006; Kirkup & Riley, 2004; Morlon, 2012; Nahum *et al.*, 2011; Nowak & Sigmund, 2002) and such dynamics was the biological motivation behind this postgraduate research.

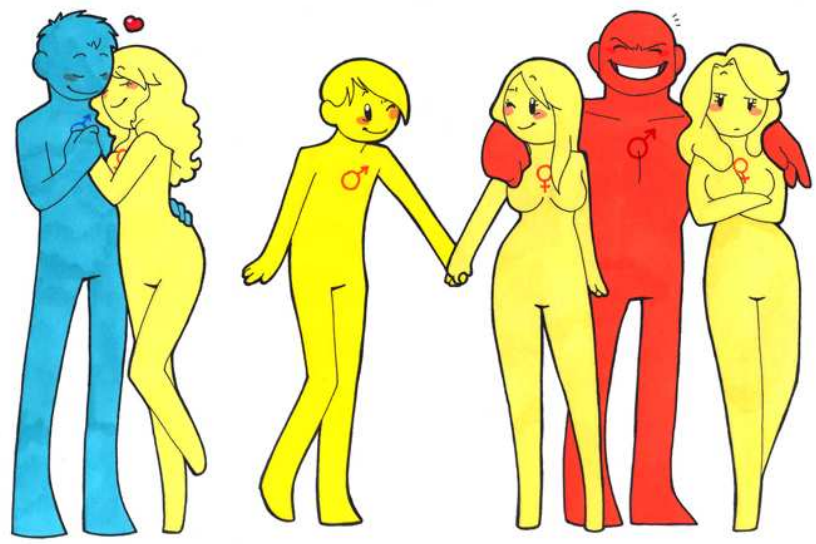

Figure 1.3: Side-blotched lizards cartoon from a comic about strange mating habits of animals. The strong red/orange throated lizards defend large territories and mate with many females. They dominate the blue throated lizards which form stronger bonds with fewer females. As a result, these females do not mate with the yellow throated lizard which itself looks like a female. However, the yellow throated lizards breed easily with the females of the red/orange throated lizards by sneaking into their large territories. In other words, orange beats blue, blue beats yellow and yellow beats orange. Reproduced from [HumonComics].

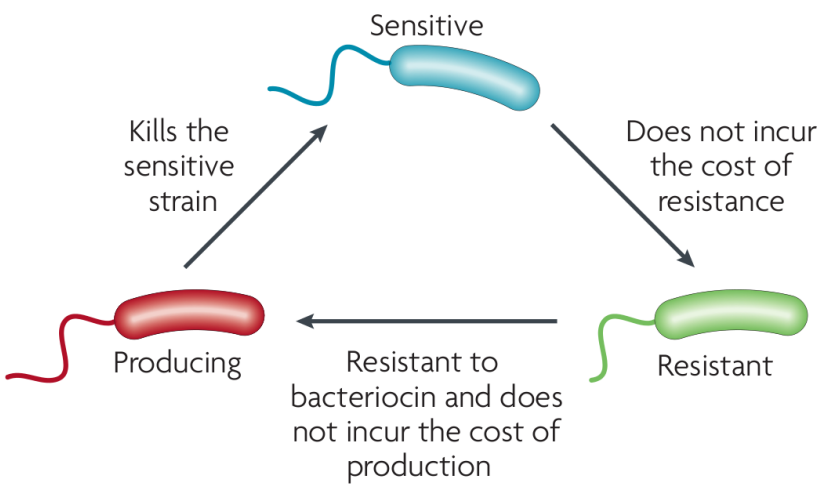

Figure 1.4: Toxin based cyclic dominance between producing, sensitive and resistant strains of *E. coli* bacteria. See text for the description of the dynamics. Reproduced from Hibbing *et al.* (2010).

The system is modelled in the framework of evolutionary game theory with rock-paper-scissors interactions. The three species forming the microbial community are the colicin-producing, colicin-sensitive and colicin-resistant strains shown in Figure 1.4. The strain sensitive to the toxic colicin devotes all of its resources to reproduction possessing the largest birth rate. The resistant species produces an immunity protein sacrificing a part of its reproduction capabilities. The toxic bacteria, produce both the colicin and the antidote thus having the lowest birth rate. Therefore, there are three strategies concerning immunity and reproduction with the cyclic dominant model where the producing strain poisons the sensitive, the sensitive outgrows the resistant and the resistant outgrows the producing. This misleadingly simple dynamics can lead to complex behaviour when applied to a finite population of interacting individuals and the resulting emergent phenomena are studied in the remaining chapters of this thesis.

1.2 Advancements of Previous Studies

The aim of the postgraduate research presented in this thesis was to unify and generalise the models of cyclic dominance in structured populations of three species within a coherent mathematical and computational framework. In order to advance the studies of the original model (Reichenbach *et al.*, 2007a), and the closely related research it inspired (Cremer, 2008; Frey, 2010; Jiang *et al.*, 2011, 2012; Peltomäki & Alava, 2008; Reichenbach & Frey, 2008; Reichenbach *et al.*, 2007b, 2008; Rulands *et al.*, 2013), it was necessary to reconsider the proposed techniques of mathematical analysis and simulation. As a result, the understanding of previously reported effects was corrected and expanded while new phenomena were also discovered. The findings were interpreted and communicated to the scientific community via a peer-reviewed publication and this thesis serves as a more detailed description of the analysis summarised in Szczesny *et al.* (2013) and Szczesny *et al.* (2014) with supplementary material provided in Szczesny *et al.* (2012). In addition, the results of the postgraduate research are included in a review on cyclic dominance in evolutionary games (Szolnoki *et al.*).

The model presented here is a generic model inspired by bacterial dynamics incorporating many biological interactions such as different forms of mobility, predatory selection and mutation, unifying some of the most common extensions of the original rock-paper-scissors system (Reichenbach *et al.*, 2007a). The novel approach to the analysis of this model consists of three different descriptions of the underlying dynamics with a mathematically tractable and coherent framework of transitions between them. Such framework allows for tracking of the entire spatial and temporal dynamics in arbitrary detail and for long times. It proves that a connection between theoretical predictions and numerical experiments can be realised even for complex models of population dynamics, and that such connection can lead to discoveries of new phenomena as well as clarifications of well-known results.

The stochastic model of previous studies consisted of a lattice of single occupancy sites, populated by individuals representing the bacteria. The single occupancy meant that the demographic noise associated with such finite system prevented any meaningful coarse-graining of the microscopic dynamics despite the

macroscopic descriptions being presented alongside the stochastic model. Therefore, the generic metapopulation model implements a lattice of subpopulations with an adjustable carrying capacity (Lugo & McKane, 2008; McKane & Newman, 2004). This allows for a controlled derivation leading to the deterministic equations via the standard techniques of the inverse system size expansion (Gardiner, 1985; Van Kampen, 2007). Such derivation presents a significant improvement over the naive proposal of deterministic models based on the mass action law which neglects the nonlinear terms resulting from spatial interactions.

The discovery of spiral patterns in the original model prompted a mapping of the macroscopic description onto a specific amplitude equation. This mapping was achieved via the centre manifold and near identity transformations based on assumptions which cannot be satisfied. The chosen amplitude equation was the two-dimensional complex Ginzburg–Landau equation (CGLE), a celebrated pattern forming system exhibiting spiral waves. The existing literature on the 2D CGLE was then used to characterise the dynamics of the patterns in the original model. This procedure was followed by the subsequent studies of closely related models. However, the postgraduate research presented in this thesis questions the validity of the predictions based on such mapping and proposes an alternative controlled perturbative treatment. In such analysis, an asymptotic multiscale expansion is performed around the bifurcation responsible for the formation of the spiral waves (Miller, 2006). Subsequently, a smooth departure from the onset of bifurcation is possible through an additional parameter motivated by the mutation of bacteria reported in the experiments with *E. coli*. Therefore, the CGLE is derived close to the onset of the bifurcation such that the theoretical predictions can then be tested away from the onset in the regime of previous studies.

The spiral patterns of the original and the related models were characterised by a derivation based on localised perturbations (van Saarloos, 2003). This predictions are shown to be valid only for a specific set of parameters and an alternative approach utilising a plane wave Ansatz is proposed to find the correct wavelengths and velocities of the spiral waves. In addition, the analysis of the convective instability of the waves is presented (Hoyle, 2006) and its predictions are confirmed in numerical simulations.

The application of the two aforementioned expansions to a problem of this complexity was not attempted before and presents considerable algebraic challenges. Nevertheless, this approach is a combination of standard methods and their complexity is overcome with computer algebra systems. In contrast, the simulations of the generic metapopulation model are arguably the most innovative part of this research with a complete departure from the algorithms used in the previous studies. As with the mathematical analysis, the numerical framework presented here insists on rigorous coherence between stochastic and deterministic descriptions of the bacterial dynamics by employing exact computer simulations. This allows for validation of the numerical experiments by performing simulations of the same system with two different techniques and cross-checking the generated outputs which must be identical in certain limiting cases.

During the postgraduate research, the Gillespie algorithm (Gillespie, 1976) was extended to simulate two-dimensional structured populations of bacteria with a large number of individuals and possible reactions showing complete agreement with the deterministic predictions. These statistically exact experiments are a significant improvement on the usual lattice Monte Carlo simulations. As a result, no additional rescalings or renormalisations are required to compare the theoretical results with the numerical experiments.

To complement the stochastic simulations, the macroscopic equations and the CGLE are solved numerically with accurate pseudo-spectral methods (Cox & Matthews, 2002) instead of relying on preconfigured software packages. The insight gained from developing the bespoke algorithms allowed for a better understanding of the interplay between the diffusion constants, domain sizes and other simulations parameters. Some research concentrated on this interplay reporting effects on the pattern formation linked to the maintenance of biodiversity. This research takes a different approach by first showing how these effects can be explained and predicted with the knowledge of the numerical methods. The aim of such approach is to isolate effects of numerical simulations in order to study the intrinsic dynamics of the generic metapopulation model.

Chapter 2

Mathematical Methods

The following sections in this chapter contain the details of the mathematical framework modelling the bacterial dynamics described in Chapter 1. The framework consists of three complementary equations, which approximate the interactions between the bacteria at varying levels of complexity. The starting point of the derivations is an individual based stochastic model of a metapopulation, formulated in terms of a Markov chain and described in Section 2.2. The inverse system size expansion, also known as the van Kampen expansion (Van Kampen, 2007), is then applied to such stochastic description. As a result, partial differential equations (PDEs) are derived as an approximation of the stochastic dynamics in the limit of large system size. Section 2.3 contains the discussion of the deterministic model, followed by a multi-scale asymptotic expansion (Miller, 2006). The second expansion yields an amplitude equation approximating the behaviour of the PDEs and can be recognised as the two-dimensional complex Ginzburg–Landau equation (CGLE). Finally, certain aspects of the pattern forming nature of the CGLE, such as the Eckhaus instability, are studied with controlled derivations (Hoyle, 2006). The results of the analysis, complemented by the existing literature on the CGLE, serve as a guide to understanding the dynamics of the deterministic and stochastic descriptions of the generic metapopulation model.

2.1 Mathematical Introduction

Mathematical modelling of populations is an interesting problem which may help understanding the maintenance of biodiversity as well as its loss leading to extinction of species. In the language of mathematical biology, the extinctions occur when the system dynamics drifts into an absorbing state. Since this situation is guaranteed in finite models discussed below, the scaling of extinctions times with the system size is usually considered. For example, in certain nonspatial models, the time to extinction scales linearly with the population size. However, when space is added, the coexistence time is proportional to the exponent of the population size implying prolonged biodiversity (Reichenbach *et al.*, 2007a).

Early descriptions of population dynamics considered continuous nonspatial systems modelled with ordinary differential equations (ODEs) which were appropriate for populations with a large number of individuals (Lotka, 1920; Volterra, 1926, 1928). However, when that number was insufficient for the assumed coarse-graining to be accurate, the discrete and finite nature of the dynamics remained hidden by this deterministic approach. The need to capture those missing characteristics focused the research onto a microscopic description based on stochastic processes. Such model was adequate to capture the effects of the intrinsic fluctuations caused by the finite sizes of the populations and was used to derive the macroscopic ODEs in the limit of infinite population where the demographic noise vanishes (Black & McKane, 2012; Van Kampen, 2007). This approach provided individual based models (Grimm, 1999) which were accurate not only in the limit of finite system size but also reduced to the aforementioned macroscopic models in the continuum limit. The effects of the demographic noise due to the discreteness of the populations could now be studied in detail. The inclusion of this intrinsic stochasticity corrected the previous results obtained with ODEs and showed a rather different, nondeterministic nature of biological ecosystems (Durrett & Levin, 1994; McKane & Newman, 2004, 2005; Traulsen *et al.*, 2005).

Both the individual and population level models were primarily concerned with well-mixed systems. The assumed mixing meant that any number of biological agents can interact with complete disregard of the spatial structure of their habitat. While this zero-dimensional model was suitable in some cases, it was

necessary to develop more realistic spatially extended descriptions. In addition to stochastic effects, the spatial structure of the populations was shown to be important (Durrett, 1999; Durrett & Levin, 1994, 1998; Kareiva *et al.*, 1990). For example, in the experiments with *E. coli* bacteria, spatial structure facilitated maintenance of biodiversity by changing the final state of the system. When all species were kept in a flask, i.e. a well-mixed system, all sensitive bacteria were poisoned by the toxic strain which in turn was outgrown by the resistant bacteria. However, when placed on a two dimensional habitat of agar plates, the bacteria coexisted for the entire period of the experiment as shown in Figure 5.15. Subsequently, the deterministic modelling focused on partial differential equations while complementary stochastic reaction-diffusion systems were proposed for microscopic models. As in the nonspatial case, the PDEs could be derived from the stochastic dynamics as the two descriptions were again equivalent in the limit of large system size.

As with the addition of stochasticity caused by the finite population size, the inclusion of mobility of the individuals resulted in new and rich dynamics. The spatial structure of the system was shown to impact on the underlying dynamics and biodiversity (Reichenbach *et al.*, 2007a). In addition, interactions between different strains of bacterial species may cause them to self-organise into complex patterns emerging from random initial conditions (Koch & Meinhardt, 1994) including spiral waves (Boerlijst & Hogeweg, 1991). Such pattern formation helps to maintain the biodiversity of the ecosystem by allowing the strains to coexist without extinctions. However, the patterns can be destroyed in certain conditions resulting in the loss of biodiversity while the true role of demographic noise in such processes is yet to be determined. One of aims of theoretical biology is to study ecosystems using various mathematical and computational approaches in order to understand the stability of these patterns as a function of biological parameters. Therefore, it is important to incorporate an appropriate level of spatial structure into the mathematical models to make such analysis possible. One such model is based on a metapopulation, an assembly of well-mixed systems residing on a lattice or a network as shown in Figure 2.1 (Eriksson *et al.*, 2013; Kareiva *et al.*, 1990). The interactions between the individuals are restricted to a single subpopulation while their movement is allowed between the patches.

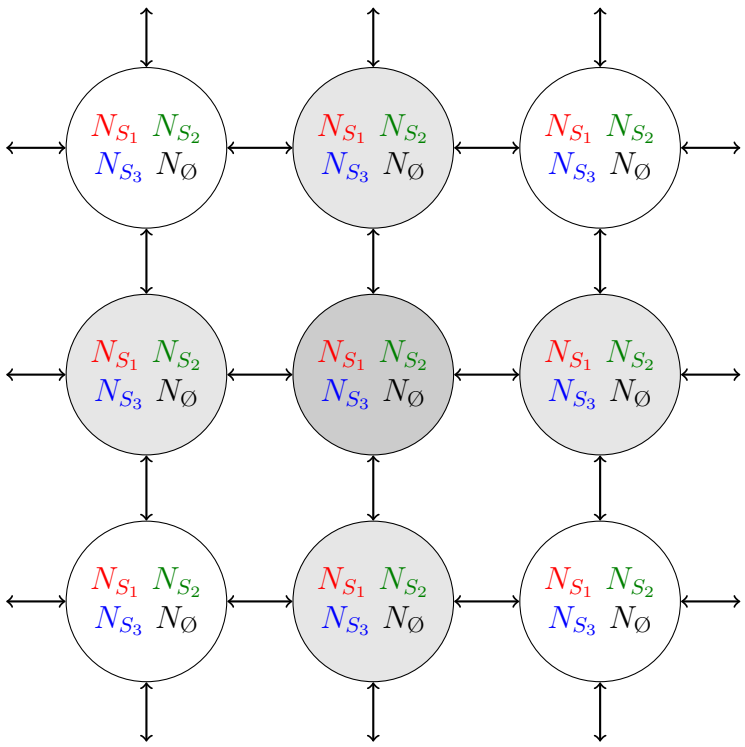

Figure 2.1: A diagram depicting a small section of the periodic square lattice of bacterial metapopulation. Each circle is a well-mixed subpopulation of carrying capacity N. The migrations occur in 4-neighbourhood, e.g. the neighbourhood of the middle pat ch, coloured in darker grey, are the four patches coloured in lighter grey (Boerlijst & Hogeweg, 1991). See Section 2.2 for details.

An advantage of such model is the possibility of a system size expansion which can be achieved for the entire lattice (Lugo & McKane, 2008). In comparison to other models which allow only one individual per site, larger sizes of the subpopulations enable a more controlled expansion.

It should be noted that choosing a lattice as an underlying spatial structure is an appropriate description of the local interactions within the neighbourhood which are physical and not social in nature. Therefore, network structures are not studied in this thesis, while the most promising extensions of the model consider the individuals interacting within a certain radius (Ni *et al.*, 2010).

2.2 Stochastic Model

The generic stochastic system consists of L^2 subpopulations placed on a square $(L \times L)$ periodic lattice, labelled by a vector $\boldsymbol{\ell} = (\ell_1, \ell_2) \in \{1, \ldots, L\}^2$ as depicted in Figure 2.1. Each patch is a well-mixed population of species S_1, S_2, S_3 and empty spaces $\emptyset$ with their respective numbers in patch $\boldsymbol{\ell}$ denoted as $N_{1,\boldsymbol{\ell}}$, $N_{2,\boldsymbol{\ell}}$, $N_{3,\boldsymbol{\ell}}$ and $N_{\emptyset,\boldsymbol{\ell}}$. All populations have a limited carrying capacity N such that $N = N_{\emptyset,\boldsymbol{\ell}} + N_{1,\boldsymbol{\ell}} + N_{2,\boldsymbol{\ell}} + N_{3,\boldsymbol{\ell}}$. Inside one patch, each species undergoes the following reactions

$$S_i + \emptyset \xrightarrow{\beta} 2S_i \tag{2.1}$$

$$S_i + S_{i+1} \xrightarrow{\sigma} S_i + \emptyset \tag{2.2}$$

$$S_i + S_{i+1} \xrightarrow{\zeta} 2S_i \tag{2.3}$$

$$S_i \xrightarrow{\mu} S_{i\pm1}. \tag{2.4}$$

Here, the index of the species $i \in \{1, 2, 3\}$ and it is ordered cyclically such that $S_{3+1} = S_1$ and $S_{1-1} = S_3$. The cyclic dominance interactions, summarised in (2.2) and (2.3), take the form of selection-removal process at rate σ and selection-replacement at rate ζ. If empty space is available, the reproduction occurs at rate β as stated in (2.1) while there are also two mutation reactions for each species at rate μ as given in (2.4).

It should be emphasised that all of the reactions happen in each subpopulation between the individuals who are currently inside it. Such system is then allowed to exchange individuals via migration between two neighbouring patches. The migration happens either when two individuals exchange their habitat at rate δ_E or when one diffuses into a previously unoccupied empty space at rate δ_D. These two kinds of diffusion are usually modelled as happening at the same rate, however, the generic metapopulation model presented here considers them as different processes. This leads to the appearance of nonlinear diffusive terms in the partial differential equations describing the dynamics of the system which vanish only for the special case $\delta_D = \delta_E$ considered in previous studies. Therefore, these rates have been divorced in order to observe any effects of such nonlinear mobility (He *et al.*, 2011).

Reference	β	σ	ζ	μ	δ_D ?† δ_E	$N^{\ddagger}$	$L^{\ddagger}$	$NL^2/10^6$
Reichenbach *et al.* (2007a)	✓	✓	✗	✗	=	1	200	0.04
Reichenbach *et al.* (2007b)	✓	✓	✗	✗	=	1	1000	1.00
Reichenbach *et al.* (2008)	✓	✓	✗	✗	=	1	200	0.04
Reichenbach & Frey (2008)	✓	✓	✓	✗	=	1	100	0.01
Peltomäki & Alava (2008)	✓	✗	✓	✗	=	1	200	0.04
Cremer (2008)	✓	✓	✗	✓	=	1	-	-
He *et al.* (2011)	✓	✓	✗	✗	=, $\neq$	1	256	0.07
Jiang *et al.* (2011)	✓	✓	✗	✗	=	1	1000	1.00
Jiang *et al.* (2012)	✓	✓	✗	✗	=	1	512	0.26
Rulands *et al.* (2013)	✓	✓	✓	✗	=	8	60	0.03
Szczesny *et al.* (2013, 2014)	✓	✓	✓	✓	=, $\neq$	1024	512	268.44

Table 2.1: Comparison of previous studies to the postgraduate research presented in this thesis, also published in Szczesny *et al.* (2013, 2014). † Symbols = and $\neq$ refer to studies with $\delta_D = \delta_E$ and $\delta_D \neq \delta_E$ respectively. ‡ Maximum values of N and L in a single simulation are reported with the resulting value of NL^2.

Two neighbouring populations will be denoted with $\boldsymbol{\ell}$ and $\boldsymbol{\ell}'$ where the site $\boldsymbol{\ell}'$ is considered to be in the 4-neighbourhood of $\boldsymbol{\ell}$ i.e. above, below, left and right of site $\boldsymbol{\ell}$, as explained by Figure 2.1. In addition, the summation over all of the neighbour sites will be denoted as $\boldsymbol{\ell}' \in \boldsymbol{\ell}$. Formally, the migration reactions can be written as

$$\left[S_i\right]_{\boldsymbol{\ell}}\left[\emptyset\right]_{\boldsymbol{\ell}'} \xrightarrow{\delta_D} \left[\emptyset\right]_{\boldsymbol{\ell}}\left[S_i\right]_{\boldsymbol{\ell}'} \tag{2.5}$$

$$\left[S_i\right]_{\boldsymbol{\ell}}\left[S_{i\pm1}\right]_{\boldsymbol{\ell}'} \xrightarrow{\delta_E} \left[S_{i\pm1}\right]_{\boldsymbol{\ell}}\left[S_i\right]_{\boldsymbol{\ell}'} \tag{2.6}$$

where the square brackets with subscript position emphasise the two different subpopulations between which the migrations take place.

Most previous studies of similar models considered single occupancy sites by setting $N = 1$ while some simulated metapopulations with $N = 8$ (Rulands *et al.*, 2013). Since the derivation of the deterministic description of the model assumes $\frac{1}{\sqrt{N}} \ll 1$, such low values of the subpopulation carrying capacity do not allow for significant elimination of noise. This claim is confirmed by the control experiments in Section 5.6 where stochastic and deterministic simulations are validated by direct comparison whose satisfactory level is achieved for $N \geq 256$ as shown in Figure 5.13. It should be noted that in the case of single occupancy, the on-site reactions cannot occur in the metapopulation model presented in this thesis. In previous studies, these reactions involved individuals from neighbouring sites while the nonlinear terms arising due to such modelling were ignored in the deterministic equations. Apart from these differences, the generic model can be considered similar to the original model proposed in Reichenbach *et al.* (2007a) in the specific case of $\zeta = \mu = 0$ and $\delta_D = \delta_E$. Other aspects of the dynamics with $\zeta \neq 0$, $\mu \neq 0$ and $\delta_D \neq \delta_E$ were investigated respectively in Reichenbach & Frey (2008), Cremer (2008) and He *et al.* (2011) and are thus generalised in this work. The detailed comparison between the previous studies and the generic model is summarised in Table 2.1. It is also worth mentioning that similar models were also studied in one spatial dimension (He *et al.*, 2010; Rulands *et al.*, 2011).

2.2.1 Master Equation

The Master equation describes the probabilistic time evolution of the metapopulation lattice (Reichl, 2009; Van Kampen, 2007). Firstly, the transition probabilities for each reaction (2.1), (2.2), (2.3), (2.4) occurring inside the patch are defined by combining their rates with appropriate combinatorial factors

$$T^{\beta}_{i,\boldsymbol{\ell}} = \beta \frac{N_{i,\boldsymbol{\ell}} N_{\emptyset,\boldsymbol{\ell}}}{N^2} \tag{2.7}$$

$$T^{\sigma}_{i,\boldsymbol{\ell}} = \sigma \frac{N_{i,\boldsymbol{\ell}} N_{i+1,\boldsymbol{\ell}}}{N^2} \tag{2.8}$$

$$T^{\zeta}_{i,\boldsymbol{\ell}} = \zeta \frac{N_{i,\boldsymbol{\ell}} N_{i+1,\boldsymbol{\ell}}}{N^2} \tag{2.9}$$

$$T^{\mu}_{i,\boldsymbol{\ell}} = \mu \frac{N_{i,\boldsymbol{\ell}}}{N}. \tag{2.10}$$

The combinatorial factors, such as $\frac{N_{i,\boldsymbol{\ell}}N_{i+1,\boldsymbol{\ell}}}{N^2}$, define the probability of individuals of species S_i and S_{i+1} to interact within a subpopulation at site $\boldsymbol{\ell}$. The same argument applies to birth and hopping reactions where $\frac{N_{i,\boldsymbol{\ell}}N_{\emptyset,\boldsymbol{\ell}'}}{N^2}$ denotes the probability of species S_i encountering an empty space. Migration between two patches, stated in (2.5) and (2.6), can be defined in a similar way by writing

$$D^{\delta_D}_{i,\boldsymbol{\ell},\boldsymbol{\ell}'} = \delta_D \frac{N_{i,\boldsymbol{\ell}}N_{\emptyset,\boldsymbol{\ell}'}}{N^2} \tag{2.11}$$

$$D^{\delta_E}_{i,\boldsymbol{\ell},\boldsymbol{\ell}'} = \delta_E \frac{N_{i,\boldsymbol{\ell}}N_{i\pm1,\boldsymbol{\ell}'}}{N^2}. \tag{2.12}$$

Before stating the full Master equation, which can be thought of as an equation describing the flow of probabilities in and out of a particular state, it is convenient to introduce the step up and step down operators. These act on a given state or transition by increasing or decreasing the numbers of individuals such that

$$\mathbb{E}^{\pm}_{i,\boldsymbol{\ell}}\, T^{\beta}_{i,\boldsymbol{\ell}} = \beta \frac{(N_{i,\boldsymbol{\ell}} \pm 1)\; N_{\emptyset,\boldsymbol{\ell}}}{N^2}. \tag{2.13}$$

Here, the number of species S_i in population $\boldsymbol{\ell}$ is altered by ± 1 in the expression for the transition probability $T^{\beta}_{i,\boldsymbol{\ell}}$. Since increasing or decreasing $N_{i,\boldsymbol{\ell}}$ and $N_{\emptyset,\boldsymbol{\ell}}$ will be a common operation in the analysis, the definition of such operators shortens the notation and allows for writing the total transition operator for reactions within each subpopulation as

$$\begin{aligned}\mathbb{T}_{i,\boldsymbol{\ell}} = &\left[\mathbb{E}^{+}_{i+1,\boldsymbol{\ell}} - 1\right] T^{\sigma}_{i,\boldsymbol{\ell}} + \left[\mathbb{E}^{-}_{i,\boldsymbol{\ell}}\mathbb{E}^{+}_{i+1,\boldsymbol{\ell}} - 1\right] T^{\zeta}_{i,\boldsymbol{\ell}} \\ &+ \left[\mathbb{E}^{-}_{i,\boldsymbol{\ell}} - 1\right] T^{\beta}_{i,\boldsymbol{\ell}} + \left[\mathbb{E}^{-}_{i,\boldsymbol{\ell}}\mathbb{E}^{+}_{i+1,\boldsymbol{\ell}} + \mathbb{E}^{-}_{i,\boldsymbol{\ell}}\mathbb{E}^{+}_{i-1,\boldsymbol{\ell}} - 2\right] T^{\mu}_{i,\boldsymbol{\ell}}.\end{aligned} \tag{2.14}$$

The general form of the $[\mathbb{E}^{\pm}_{\cdots} - 1]T^{\cdots}_{\cdots}$ terms comes from the gains and losses of probability to find the system in a particular state. For example, considering the birth reaction of N_1, the system with N_1 individuals gains probability of occurrence with transitions from state with $N_1 - 1$ individuals while losing the probability by transitioning into $N_1 + 1$ state.

Similarly, the total migration operator summarising the diffusions reads

$$\begin{aligned}\mathbb{D}_{i,\boldsymbol{\ell},\boldsymbol{\ell}'} = &\left[\mathbb{E}^{+}_{i,\boldsymbol{\ell}}\mathbb{E}^{-}_{i,\boldsymbol{\ell}'} - 1\right] D^{\delta_D}_{i,\boldsymbol{\ell},\boldsymbol{\ell}'} \\ &+ \left[\mathbb{E}^{+}_{i,\boldsymbol{\ell}}\mathbb{E}^{-}_{i+1,\boldsymbol{\ell}}\mathbb{E}^{-}_{i,\boldsymbol{\ell}'}\mathbb{E}^{+}_{i+1,\boldsymbol{\ell}'} - 1\right] D^{\delta_E}_{i,\boldsymbol{\ell},\boldsymbol{\ell}'}.\end{aligned} \tag{2.15}$$

Therefore, the Master equation for the probability $P(\mathbf{N}, t)$ of a system occupying a certain state $\mathbf{N}$ at time t can be written down by summing the operators over all species and subpopulations

$$\frac{dP(\mathbf{N},t)}{dt} = \sum_{i=1}^{3}\sum_{\boldsymbol{\ell}}^{\{1,\dots,L\}^2}\left[\mathbb{T}_{i,\boldsymbol{\ell}} + \sum_{\boldsymbol{\ell}'\in\boldsymbol{\ell}}\mathbb{D}_{i,\boldsymbol{\ell},\boldsymbol{\ell}'}\right] P(\mathbf{N},t). \tag{2.16}$$

Here, $\mathbf{N}$ is a collection of numbers of species $N_{i,\boldsymbol{\ell}}$ and empty spaces $N_{\emptyset,\boldsymbol{\ell}}$ in all subpopulations defining uniquely the state of the whole system. Later, $\boldsymbol{\eta}$ is used to symbolise a similar collection of stochastic fluctuations η_i defined below in Section 2.2.2 discussing the system size expansion.

2.2.2 System Size Expansion

To proceed with the inverse system size expansion in the carrying capacity N (Van Kampen, 2007), new rescaled variables need to be defined. The normalised abundances of species are equal to $s_{i,\boldsymbol{\ell}} = N_{i,\boldsymbol{\ell}}/N$ while the fluctuations $\eta_{i,\boldsymbol{\ell}}$ around the fixed point s^* are defined to scale with $\sqrt{N}$ such that

$$\eta_{i,\boldsymbol{\ell}} = \sqrt{N}\,(s^* - s_{i,\boldsymbol{\ell}}) \tag{2.17}$$

which after differentiating with respect to time becomes

$$\frac{d\eta_{i,\boldsymbol{\ell}}}{dt} = -\sqrt{N}\frac{ds_{i,\boldsymbol{\ell}}}{dt}. \tag{2.18}$$

With this Ansatz, it is now possible to write the Master equation in terms of the fluctuations for a redefined probability $\Pi(\boldsymbol{\eta}, t)$. It should be noted that the time taken for a change in the normalised species abundances $s_{i,\boldsymbol{\ell}}$ scales with N

as each reaction changes the abundances by $\frac{1}{N}$ on average. As a result, it takes longer to achieve the same percentage change in $s_{i,\boldsymbol{\ell}}$ for increasing values of N, creating discrepancies with the continuous equations for which N is not relevant. Therefore, a rescaled time $t \to Nt$ is introduced such that $\frac{d}{dt} \to \frac{1}{N}\frac{d}{dt}$ in order to obtain sensible time scales in the dynamics. Dropping the dependence of $\Pi(\boldsymbol{\eta}, t)$ on all $\eta_{i,\boldsymbol{\ell}}$ and t to ease the notation, the right hand side of (2.16) reads

$$\frac{d\Pi}{dt} = \frac{1}{N}\frac{\partial \Pi}{\partial t} - \sum_{i=1}^{3}\sum_{\boldsymbol{\ell}}^{\{1,\dots,L\}^2} \frac{1}{\sqrt{N}}\frac{ds_{i,\boldsymbol{\ell}}}{dt}\frac{\partial \Pi}{\partial \eta_{i,\boldsymbol{\ell}}}. \tag{2.19}$$

The left hand side of (2.16) is written in a similar way after the introduction of s_i and η_i. The step up and step down operators are now expanded in their differential form which, up to the order $\mathcal{O}(\frac{1}{N})$, are

$$\mathbb{E}^{\pm}_{i,\boldsymbol{\ell}} = 1 \pm \frac{1}{\sqrt{N}}\frac{\partial}{\partial \eta_{i,\boldsymbol{\ell}}} + \frac{1}{2}\frac{1}{N}\frac{\partial^2}{\partial \eta^2_{i,\boldsymbol{\ell}}}. \tag{2.20}$$

The consecutive application of the operators can be obtained by multiplying their differential forms. For example, the application of $\mathbb{E}^{+}_{i,\boldsymbol{\ell}}\mathbb{E}^{-}_{i,\boldsymbol{\ell}'}$ gives

$$\mathbb{E}^{+}_{i,\boldsymbol{\ell}}\mathbb{E}^{-}_{j,\boldsymbol{\ell}'} = 1 + \frac{1}{\sqrt{N}}\left(\frac{\partial}{\partial \eta_{i,\boldsymbol{\ell}}} - \frac{\partial}{\partial \eta_{j,\boldsymbol{\ell}'}}\right) + \frac{1}{2}\frac{1}{N}\left(\frac{\partial}{\partial \eta_{i,\boldsymbol{\ell}}} - \frac{\partial}{\partial \eta_{j,\boldsymbol{\ell}'}}\right)^2. \tag{2.21}$$

After some lengthy algebra, outlined in Section A.1, terms at the same order of N can be collected on both sides of the Master equation (2.16). Leading terms appear at order $\mathcal{O}\big(\frac{1}{\sqrt{N}}\big)$ describing the time evolution of the normalised species densities $s_{i,\boldsymbol{\ell}}$. Ignoring the migration terms for now, collecting only the on-site reactions, ordinary differential equations also referred to as the replicator equations are obtained. After dropping the vector labels $\boldsymbol{\ell}$ and introducing $\mathbf{s} = (s_1, s_2, s_3)$ and $r = s_1 + s_2 + s_3$, the ODEs describing changes in one patch read

$$\begin{aligned}\frac{ds_i}{dt} &= s_i[\beta(1-r) - \sigma s_{i-1} + \zeta(s_{i+1} - s_{i-1})] \\ &\quad + \mu(s_{i-1} + s_{i+1} - 2s_i) = \mathcal{F}_i(\mathbf{s}).\end{aligned} \tag{2.22}$$

At this point, it is possible to remove one of the rates from the equation by rescaling the time. However, all rates will be retained explicitly throughout the subsequent derivations while the birth rate β will be set to unity in the final results of Chapter 5 without the loss of generality.

Before considering the full PDEs for the whole spatial system, the general dynamics of the replicator ODEs for one subpopulation will be briefly described. The equations, analysed in Section A.2, possess a single fixed point

$$\mathbf{s}^* = s^* \begin{bmatrix} 1 \\ 1 \\ 1 \end{bmatrix} = \frac{\beta}{3\beta + \sigma} \begin{bmatrix} 1 \\ 1 \\ 1 \end{bmatrix} \tag{2.23}$$

which is globally stable for mutation rates $\mu > \mu_H$ where

$$\mu_H = \frac{\beta\sigma}{6(3\beta + \sigma)}. \tag{2.24}$$

Below the critical value of μ_H (2.24), the system undergoes a supercritical Hopf bifurcation developing a stable limit cycle with an approximate frequency

$$\omega_H \approx \frac{\sqrt{3}\beta(\sigma + 2\zeta)}{2(3\beta + \sigma)} \tag{2.25}$$

and leaving the fixed point unstable. As mentioned before, other variants of the model were considered previously in the literature. It should be noted that retaining only the zero-sum interactions (2.3) with $\beta = \sigma = \mu = 0$ results in degenerate bifurcation and centres while the models considering the birth (2.1) and selection (2.2) processed with $\zeta = \mu = 0$ lead to heteroclinic orbits.

Reintroducing the previously ignored migration terms into the repilcator equation (2.22), the full coupled ODEs describing the dynamics in the entire metapopulation lattice can be obtained and used as a guide to state the following PDEs

$$\begin{aligned} \partial_t s_i = {} & \mathcal{F}_i(\mathbf{s}) + \delta_D \nabla^2 s_i \\ & + (\delta_D - \delta_E)\Big(s_i \nabla^2 (s_{i+1} + s_{i-1}) - (s_{i+1} + s_{i-1})\nabla^2 s_i\Big) \end{aligned} \tag{2.26}$$

```
pde_s1 :=
beta*s1*(1 - s1 - s2 - s3) - sigma*s1*s3 + zeta*s1*(s2 - s3)
+ mu*(s2 + s3 - 2*s1) + delta_d*lap_s1
+ (delta_d - delta_e) * (s1*(lap_s2 - lap_s3) - (s2 + s3)*lap_s1)
```

Listing 2.1: Simplified solution from the `REDUCE` script provided in Section A.1 deriving the PDEs (2.26) from the Master equation (2.16). Here, the prefix `lap_` indicates the Laplacian operator. Only the first equation for $\partial_t s_1$ is shown in this listing and the remaining PDEs can be obtained through cyclic permutations.

where the discrete Laplacian in the ODEs is replaced by a continuous one

$$\nabla^2 = \partial^2_{x_1} + \partial^2_{x_2} \tag{2.27}$$

by defining the continuous spatial coordinate $\mathbf{x} = [0, L]$ such that

$$\nabla^2 s_i \equiv \sum_{\boldsymbol{\ell}' \in \boldsymbol{\ell}} s_{i,\boldsymbol{\ell}'} - 4 s_{i,\boldsymbol{\ell}}. \tag{2.28}$$

It is important to mention that an alternative definition of the continuous limit was proposed in previous studies (Reichenbach *et al.*, 2008). Such procedure involves shrinking the domain size to unit area in the limit of vanishing lattice spacing and the introduction of rescaled diffusion constants $D_D \sim \delta_D / L^2$ and $D_E \sim \delta_E / L^2$. However, no such rescaling is performed here to allow for the same values of δ_D, δ_E and L to be used in both stochastic and deterministic simulations.

It should be noted that apart from the nonspatial replicator equation $\mathcal{F}_i(\mathbf{s}_{\boldsymbol{\ell}})$ (2.22) and a linear diffusive term $\delta_D \nabla^2 s_{i,\boldsymbol{\ell}}$ there are also some additional nonlinear diffusive terms. These are one of the novelties of the model which vanish in the case of $\delta_D = \delta_E$ assumed in a majority of previous studies.

The manual derivation of PDEs (2.26) requires some considerable algebraic manipulations providing plenty of opportunities for introducing unintentional errors. Therefore, the computer algebra system `REDUCE` (Hearn, 2004) is utilised to derive the equations and part of its output related to the PDEs (2.26) can be seen in Listing 2.1. The full listing of the `REDUCE` notebook capable of performing the system size expansion can be found in Section A.1.

2.3 Deterministic Model

The macroscopic PDEs (2.26) derived in Section 2.2.2 serve as a deterministic description of the generic metapopulation model in the limit of large system size. The equations can be approximated by the CGLE which is derived via a controlled asymptotic expansion in Section 2.3.3 while the mapping onto the CGLE performed in previous studies is reproduced in Section 2.3.2 for comparison.

2.3.1 Linear Transformations

Before performing the mapping and the asymptotic expansion outlined in Sections 2.3.2 and 2.3.3, the PDEs (2.26) are subject to some linear transformations. After the origin is moved to the position of the fixed point (2.23) via $(\mathbf{s}-\mathbf{s}^*)$, the system is transformed into the Jordan normal form with new variables $\mathbf{u} = (u_1, u_2, u_3)$ replacing $\mathbf{s} = (s_1, s_2, s_3)$. This is achieved by constructing a transformation matrix with the real and imaginary parts of the conjugate eigenvectors and the third real eigenvector of the Jacobian matrix as implemented in Section A.2. The two transformations can be summarised in the following way

$$\mathbf{u} = \frac{1}{\sqrt{6}} \begin{bmatrix} -1 & -1 & -2 \\ -\sqrt{3} & \sqrt{3} & 0 \\ \sqrt{2} & \sqrt{2} & \sqrt{2} \end{bmatrix} (\mathbf{s} - \mathbf{s}^*). \tag{2.29}$$

The equations for the new variable $\mathbf{u}$ can now be expressed in the Jordan normal form where the linear part of the replicator equation (2.22) reads

$$\frac{d\mathbf{u}}{dt} = \begin{bmatrix} \epsilon & -\omega_H & 0 \\ \omega_H & \epsilon & 0 \\ 0 & 0 & -\beta \end{bmatrix} \mathbf{u}. \tag{2.30}$$

The benefit of the linear transformation to variable $\mathbf{u}$ can now be observed. The transformations expose the decoupling of u_3 component from the oscillations in the u_1-u_2 plane happening at Hopf frequency ω_H (2.25). This suggests that the dynamics of three species abundances is confined to two dimensions which simplifies subsequent derivations.

2.3.2 Mapping

Before describing the asymptotic expansion of the PDEs (2.26) resulting in the derivation of the CGLE, the approximate mapping of the replicator equation (2.22) onto the CGLE is detailed below. This mapping procedure, used in previous studies, is included here for completeness and to contrast it with the multiscale expansion carried out in this thesis. It should be noted that a different matrix

$$\begin{bmatrix} \sqrt{3} & 0 & -\sqrt{3} \\ -1 & 2 & -1 \\ 1 & 1 & 1 \end{bmatrix} \tag{2.31}$$

was used in previous studies to obtain the Jordan normal form (Frey, 2010).

The technique starts with proposing an approximation to the centre manifold equation which confines the dynamics to two dimensions. In contrast with the mapping, the asymptotic expansion requires no such uncontrolled approximation and the manifold equation appears in the results of the derivation. The first order approximation is a plane perpendicular to the radial eigenvector $\boldsymbol{u} = (1, 1, 1)$. In addition, the terms in u_1, u_2 and $u_1 u_2$ can be safely ignored since their coefficient vanish in the derivation. Therefore, the proposed approximate equation of the manifold, valid for $u_1, u_2 \ll 1$, reads

$$u_3 = M(u_1, u_2) = M_{20} u_1^2 + M_{02} u_2^2. \tag{2.32}$$

The constant coefficients M_{20} and M_{02} are found by comparing terms of the same order in the following relation

$$\partial_t u_3 = \partial_{u_1} M(u_1, u_2) \partial_t u_1 + \partial_{u_2} M(u_1, u_2) \partial_t u_2 \tag{2.33}$$

where all u_3 are now replaced with the centre manifold equation $M(u_1, u_2)$ (2.32). This step enables redefinition of u_3 in terms of u_1 and u_2 which reduces the dimensionality of the dynamics. The solutions produce

$$M_{20} = M_{02} = \frac{\sigma(3 + \sigma)}{4(3 + 2\sigma - 6\mu(3 + \sigma))} \tag{2.34}$$

which gives the approximate equation for the manifold and the expression for the u_3 component. This expression is then substituted into the nonspatial replicator equations for u_1 and u_2 reducing the dynamics to two dimensions.

After confining the dynamics onto the surface of the manifold, the near identity transformations are proposed. These nonlinear transformations map (u_1, u_2) to a new variable $\mathbf{z} = z_1 + iz_2$ in the following way

$$z_1 = u_1 + C_{20}u_1^2 + C_{11}u_1u_2 + C_{02}u_2^2 \tag{2.35}$$

$$z_2 = u_2 + K_{20}u_1^2 + K_{11}u_1u_2 + K_{02}u_2^2. \tag{2.36}$$

Similarly to the manifold Ansatz (2.32), the transformations are valid only when $u_1, u_2 \ll 1$. The coefficients of the transformations are chosen such that the macroscopic ODEs assume the form of the nonspatial CGLE. Such mapping is achieved by the removal of the quadratic terms in the original ODEs which at this stage are expressed in terms of $\mathbf{u}$ after aforementioned transformations. Subsequently, inverse transformations $(u_1, u_2) \to (z_1, z_2)$ are calculated by assuming a power series expansion in components of $\mathbf{u}$. After the linear and quadratic terms are found by inspection, the inverse transformations read

$$\begin{aligned} u_1 = {} & z_1 - C_{20}z_1^2 - C_{11}z_1z_2 - C_{02}z_2^2 \\ & + C_{30}z_1^3 + C_{21}z_1^2z_2 + C_{12}z_1z_2^2 + C_{03}z_2^3 \end{aligned} \tag{2.37}$$

$$\begin{aligned} u_2 = {} & z_2 - K_{20}z_1^2 - K_{11}z_1z_2 - K_{02}z_2^2 \\ & + K_{30}z_1^3 + K_{21}z_1^2z_2 + K_{12}z_1z_2^2 + K_{03}z_2^3. \end{aligned} \tag{2.38}$$

The cubic coefficients have to be computed algebraically and their expression in terms of other coefficients are listed below for completeness

$$C_{30} = 2C_{20}^2 + C_{11}K_{20} \tag{2.39}$$

$$K_{03} = 2K_{02}^2 + C_{02}K_{11} \tag{2.40}$$

$$C_{03} = 2C_{02}K_{02} + C_{02}C_{11} \tag{2.41}$$

$$K_{30} = 2C_{20}K_{20} + K_{02}K_{11} \tag{2.42}$$

$$C_{21} = 3C_{11}C_{20} + 2C_{02}K_{20} + C_{11}K_{11} \tag{2.43}$$
$$K_{12} = 3K_{11}K_{02} + 2C_{02}K_{20} + C_{11}K_{11} \tag{2.44}$$
$$C_{12} = 2C_{02}K_{11} + 2C_{02}C_{20} + C_{11}K_{02} + C_{11}^2 \tag{2.45}$$
$$K_{21} = 2K_{02}K_{20} + 2C_{11}K_{20} + K_{11}C_{20} + K_{11}^2. \tag{2.46}$$

Time derivatives of z_1 and z_2 are obtained by differentiating the near identity transformations (2.35) with time and inserting the ODEs for the components of $\mathbf{u}$. Then, by using the backwards transformation $\mathbf{u} \to \mathbf{z}$, the formulas for $\partial_t(z_1, z_2)$ are obtained. The resulting equation can be put into a form of the nonspatial CGLE if the quadratic terms in $\mathbf{z}$ are removed. This is achieved by setting the near identity transformation coefficients to

$$C_{20} = C_{02} = 2K_{11} = \frac{\sqrt{3}\sigma(\sigma + 3\mu(3+\sigma))(3+\sigma)}{4\left(3\mu\sigma(3+\sigma) - 7\sigma^2 - 9\mu^2(3+\sigma)^2\right)} \tag{2.47}$$
$$K_{20} = K_{02} = 2C_{11} = \frac{\sigma(-5\sigma + 3\mu(3+\sigma))(3+\sigma)}{4\left(3\mu\sigma(3+\sigma) - 7\sigma^2 - 9\mu^2(3+\sigma)^2\right)}. \tag{2.48}$$

Finally, the resulting equations for (z_1, z_2) can be written as

$$\partial_t z_1 = c_1 z_1 + \omega_H z_1 - c_2(z_1 + c_3 z_2)(z_1^2 + z_2^2) \tag{2.49}$$
$$\partial_t z_2 = c_1 z_2 - \omega_H z_2 - c_2(z_2 - c_3 z_1)(z_1^2 + z_2^2) \tag{2.50}$$

which can be manipulated further to obtain the nonspatial CGLE for a complex variable $\mathbf{z}$. The expressions for c_1, c_2 and c_3 for models with $\zeta = \mu = 0$ can be found in Frey (2010); Reichenbach *et al.* (2008) and are reproduced below

$$c_1 = \frac{\beta\sigma}{2(3\beta + \sigma)} \tag{2.51}$$
$$c_2 = \frac{\sigma(3\beta + \sigma)(48\beta + 11\sigma)}{56\beta(3\beta + 2\sigma)} \tag{2.52}$$
$$c_3 = \frac{\sqrt{3}(18\beta + 5\sigma)}{48\beta + 11\sigma}. \tag{2.53}$$

More complicated expressions for $\zeta \neq 0$ are provided in Rulands *et al.* (2013) while a case with $\zeta \neq 0$ and $\mu \neq 0$ is reported in Cremer (2008). The expression for ω_H is equivalent to (2.25) with $\zeta = 0$ in studies where the zerosum interaction (2.3) was not considered.

As mentioned before, the final equation for complex variable $\mathbf{z}$ is not the full CGLE as it normally contains a spatial diffusive terms in $\nabla^2(z_1, z_2)$. These had to be added manually in an ad hoc fashion at the end of the derivations in previous studies. It is also important to note that $\mu = 0$ in the majority of original research, implying an absence of the Hopf bifurcation. This in turn guarantees that $u_1, u_2 \ll 1$ is not satisfied as required for the manifold Ansatz (2.32) and the near identity transformations (2.35).

2.3.3 Asymptotic Expansion

After obtaining the PDEs in the Jordan normal form in Section 2.3.1, the interest of the mathematical analysis lies with a small perturbation of size ϵ around the Hopf bifurcation. It is possible to begin with $\mu = \mu_H + p(\epsilon)$ and expect the small perturbation $p(\epsilon)$ to define the scaling. Most general form of such perturbation is $p(\epsilon) = p_1\epsilon + p_2\epsilon^2 + \mathcal{O}(\epsilon^3)$ where p_1 and p_2 are real constants of order $\mathcal{O}(1)$. However, the standard approach is to begin with $p(\epsilon) = p_2\epsilon^2$ since the derivation is expected to yield $p_1 = 0$ to satisfy conditions on secular terms. Furthermore, with the advance knowledge of the derivation, it is convenient to set $p_2 = -\frac{1}{3}$ in order to simplify the analysis. Therefore, the departure from the onset of Hopf bifurcation is described by a perturbation parameter ϵ such that

$$\mu = \mu_H - \frac{1}{3}\epsilon^2. \tag{2.54}$$

The following derivation provides the details of the multiscale asymptotic expansion adopted from a similar derivation in Miller (2006). In contrast to the strained coordinate methods, such expansion assumes a general undetermined functional dependence on the new multiscale coordinates.

Therefore, the first step of the analysis is the multiscale expansion of time and space coordinates

$$\frac{\partial}{\partial t} \to \frac{\partial}{\partial t} + \epsilon^2 \frac{\partial}{\partial T} \tag{2.55}$$

$$\frac{\partial}{\partial x} \to \frac{\partial}{\partial x} + \epsilon \frac{\partial}{\partial X} \tag{2.56}$$

shown here for the case of one dimensional space. The coordinates $T = \epsilon^2 t$ and $\mathbf{X} = \epsilon \mathbf{x}$ are usually referred to as the "slow" coordinates in the literature. However, as shown later in the derivation, the leading order solution has no x dependence and the "fast" spatial coordinate can be safely ignored. Subsequently, the Laplace operator (2.27) $\nabla^2 \to \epsilon^2 \nabla^2_{\mathbf{X}}$ which can be defined in terms of $\mathbf{X}$ as

$$\nabla^2_{\mathbf{X}} = \partial^2_{X_1} + \partial^2_{X_2}. \tag{2.57}$$

Finally, the variable $\mathbf{u}$ is also expanded in the perturbation parameter ϵ. The expansion, which can be truncated at the order $\mathcal{O}(\epsilon^3)$ where the CGLE is expected to appear, reads

$$\mathbf{u}(\mathbf{x}, t) = \sum_{n=1}^{3} \epsilon^n \mathbf{U}^{(n)}(t, T, \mathbf{X}). \tag{2.58}$$

It should be noted that all scaling in ϵ is made explicit with the variables T, $\mathbf{X}$ and $\mathbf{U}^{(n)}$ for all n, being of order $\mathcal{O}(1)$.

The application of the chain rule implies $\partial_t u_i = \sum_{i,n} \epsilon^{i+n} \partial_{T_n} U_i$ and similarly for $\nabla^2 u_i$ with $T_0 = t$, $T_2 = T$, $\mathbf{X}_1 = \mathbf{X}$ and $i \in \{1, 2, 3\}$. This creates a new hierarchy of simplified PDEs describing the original system which are solved at each order of ϵ while also removing the secular terms. These unbound terms arise naturally upon the application of the perturbation theory to weakly nonlinear problems and their removal provides additional information about the dynamics. Moreover, the Jordan normal form of the system suggests that the first two oscillating components of $\mathbf{U}^{(n)}$ can be combined into a complex number

$$\mathcal{Z}^{(n)} = U_1^{(n)} + i U_2^{(n)}. \tag{2.59}$$

After the multiscale expansion is complete, solving the hierarchy of simplified PDEs begins at the leading order of $\mathcal{O}(\epsilon)$ where the first set of equations reads

$$\frac{\partial \mathcal{Z}^{(1)}}{\partial t} = i\omega_H \mathcal{Z}^{(1)} \tag{2.60}$$

$$\frac{\partial U_3^{(1)}}{\partial t} = -\beta U_3^{(1)} \tag{2.61}$$

The inspection of the these PDEs suggests oscillating and decaying solutions. Hence, the following Ansätze are proposed

$$\mathcal{Z}^{(1)} = \mathcal{A}^{(1)}(T, \mathbf{X}) e^{i\omega_H t} \tag{2.62}$$

$$U_3^{(1)} = 0 \tag{2.63}$$

with $\mathcal{A}^{(1)}$ being the complex amplitude modulation at the "slow" time and length scales. Here, $U_3^{(1)} = 0$ can be safely assumed as evident from its exponentially decaying nature with rate $\beta > 0$. At the second order of ϵ, the next set of PDEs yields

$$U_3^{(2)} = \frac{\sigma}{2\sqrt{3}\beta} |\mathcal{Z}^{(1)}|^2 \tag{2.64}$$

which is the leading term in the equation for the centre manifold proposed in the mapping procedure (2.32). Finally, solving at order $\mathcal{O}(\epsilon^3)$ requires the removal of a secular term which happens to be the CGLE and can be written as

$$\partial_T \mathcal{A}^{(1)} = \delta \nabla_{\mathbf{X}}^2 \mathcal{A}^{(1)} + \mathcal{A}^{(1)} - (c_{Re} + i c_{Im}) |\mathcal{A}^{(1)}|^2 \mathcal{A}^{(1)} \tag{2.65}$$

where the two constants in the coefficient of the "cubic" $|\mathcal{A}^{(1)}|^2 \mathcal{A}^{(1)}$ term are

$$c_{Re} = \frac{\sigma}{2}\left(1 + \frac{\sigma}{6\beta}\right) \tag{2.66}$$

$$c_{Im} = \omega_H + \frac{\sigma^2}{36\omega_H} + \frac{\sigma\omega_H}{6\beta}\left(1 - \frac{\sigma}{3\beta}\right). \tag{2.67}$$

In addition, it is convenient to define an effective diffusion constant δ in terms of the two mobility rates δ_D and δ_E such that

$$\delta = \frac{3\beta\delta_E + \sigma\delta_D}{3\beta + \sigma}. \tag{2.68}$$

The form of the combined constant δ summarises the contributions from the two diffusion rates weighted by the reaction rates β and σ showing an intuitive relation between migration and biological processes. For example, in case of high reproduction $\beta \gg \sigma$, exchange of habitat dominates due to lack of empty space. However, when $\beta \ll \sigma$, diffusive migration is dominant as aggressive predation leaves most of the ecosystem unoccupied. Nevertheless, δ can be set to unity by rescaling $\mathbf{X}$, changing only the size of the overall pattern in the domain.

Finally, the equation (2.65) is simplified by a rescaled amplitude $\mathcal{A} = \sqrt{c_{Re}}\mathcal{A}^{(1)}$ and introduction of parameter $c = c_{Im}/c_{Re}$ to yield the final form of the complex Ginzburg–Landau equation

$$\partial_T \mathcal{A} = \delta\nabla^2_{\mathbf{X}}\mathcal{A} + \mathcal{A} - (1 + ic)|\mathcal{A}|^2\mathcal{A}. \tag{2.69}$$

Therefore, the only remaining variable in the CGLE (2.69) is the parameter c which combines reaction rates from the generic metapopulation model such that

$$c = \frac{c_{Im}}{c_{Re}} = \frac{12\zeta(6\beta - \sigma)(\sigma + \zeta) + \sigma^2(24\beta - \sigma)}{3\sqrt{3}\sigma(6\beta + \sigma)(\sigma + 2\zeta)}. \tag{2.70}$$

It should be noted that the general form of the CGLE has an additional complex coefficient $(1 + ib)$ in front of the diffusive term $\delta\nabla^2_{\mathbf{X}}\mathcal{A}$ (Aranson *et al.*, 1992, 1993; Weber *et al.*, 1992). However, the multiscale expansion of the PDEs (2.26) results in $b = 0$ and a real diffusion constant.

As with the system size expansion in Section 2.2.2, the algebraic manipulations of the asymptotic expansion can be challenging. To avoid any mistakes, the `REDUCE` (Hearn, 2004) computer algebra system was used again and the full listing of the notebook deriving the CGLE (2.69) can be found in Section A.2.

2.3.4 Plane Wave Ansatz

Characterisation of the spiral patterns exhibited by the two dimensional CGLE (2.69) can be attempted by proposing closed form solutions of the spiral waves. However, such complicated expressions are not necessary to gain a substantial understanding of the properties and the stability of spirals. Instead, the effects of the parameter c (2.70) are studied here with a plane wave approximation of the spiral waves which is expected to be valid away from the spiral core. Similar analysis, presented in previous studies, was shown to be inadequate because of the assumption that the velocity of the waves is constant. Therefore, the wave properties are instead obtained numerically and used to predict phenomena such as the Eckhaus instability through the analysis shown in Section 2.3.5.

To better appreciate this novel approach, the treatment based on the constant velocity assumption used in majority of previous studies is outlined below. Firstly, to understand the properties of spiral waves in the complex Ginzburg–Landau equation, a plane wave Ansatz

$$\mathcal{A} = \mathcal{R}e^{i(kX-\omega T)} \tag{2.71}$$

with a complex amplitude $\mathcal{R}$ is substituted into the CGLE producing

$$\omega = c|\mathcal{R}|^2 = c(1-\delta k^2). \tag{2.72}$$

The dispersion relation (2.72) shows that $\delta k^2 < 1$ has to be satisfied for meaningful solutions whose amplitude must have a non-negative modulus. The next step is a calculation of the wavelength of the waves by assuming that their velocity is $v = 2\sqrt{\delta}$. This assumption is incorrect by relying on the results of van Saarloos (2003) where spreading velocity of localised perturbations around the unstable state $\mathcal{A} = 0$ are considered as explained in Figure 2.2. However, according to results from Section 4.2, the numerical experiments suggest that the travelling waves have a range of different velocities which depend on the parameter c as summarised in Table 4.1. This could explain the discrepancies reported in previous studies where the results had to be rescaled by a factor of ≈ 1.6 in order to match the predictions based on constant velocity assumption (Frey, 2010; Reichenbach *et al.*, 2007b, 2008).

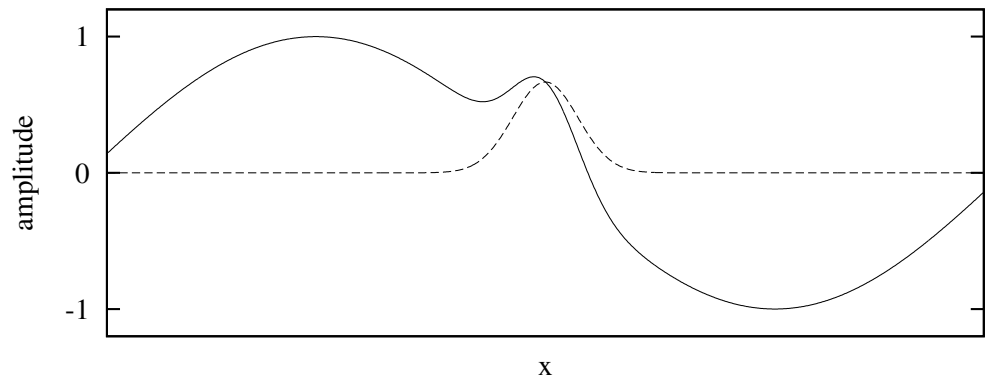

Figure 2.2: Solid line: schematic perturbation of a plane wave Ansatz analysed in Section 2.3.5. Dashed line: schematic localised perturbation around zero amplitude whose spreading velocity derived in van Saarloos (2003) was used in previous studies.

Nevertheless, the steps leading to the standard formula for the wavelength of the plane waves (2.74) are reproduced here for comparison. Firstly, substituting $\omega = vk = 2\sqrt{\delta}k$ into the dispersion relation (2.72) gives a quadratic equation for $\sqrt{\delta}k$ whose solutions satisfy

$$\delta k^2 = \frac{1}{c^2}\left(-1 \pm \sqrt{1+c^2}\right)^2. \tag{2.73}$$

As mentioned above, according to the dispersion relation (2.72) all physical solutions must satisfy $\delta k^2 < 1$. Substituting (2.73) into this condition and simplifying yields $2 < \pm 2\sqrt{1+c^2}$ which shows that the solution for k with the minus sign has to be discarded as nonphysical. Therefore, based on the assumption that $v = 2\sqrt{\delta}$, the derived formula for the wavelength is

$$\lambda = \frac{2\pi}{k} = \frac{2\pi c\sqrt{\delta}}{\sqrt{1+c^2}-1}. \tag{2.74}$$

In addition, it should be noted that some of the formulas reported in previous studies contain a factor of $1-\sqrt{1+c^2}$ instead of $\sqrt{1+c^2}-1$ in the denominator which makes the expression for the wavelength negative (Cremer, 2008; Frey, 2010; Reichenbach & Frey, 2008; Reichenbach *et al.*, 2007b, 2008).

In contrast, following the plane wave approach (2.71) presented in this thesis, the wavelength $\lambda = 2\pi/k$ obtained from the dispersion relation (2.72) reads

$$\lambda = 2\pi\sqrt{\frac{\delta}{1-|\mathcal{R}|^2}} \tag{2.75}$$

while the velocity $v = \omega/k$ can be calculated with

$$v = c|\mathcal{R}|^2\sqrt{\frac{\delta}{1-|\mathcal{R}|^2}} \tag{2.76}$$

where $|\mathcal{R}|^2$ must be obtained numerically as explained in Section 4.2.

2.3.5 Eckhaus Instability

Eckhaus instability, also referred to as Benjamin-Feir instability, is a convective instability caused by growing perturbations which are convected away from the spiral core (Hoyle, 2006). In order to derive the Eckhaus criterion in the CGLE, a similar derivation for the Newell-Whitehead-Segel equation is adopted from Hoyle (2006). Firstly, amplitude and phase pertubations $|\rho|, |\varphi| \ll 1$ are added to the plane wave Ansatz to allow for full generality such that

$$\mathcal{A} = (1+\epsilon'\rho)\mathcal{R}e^{i(kX-\omega T+\epsilon'\varphi)}. \tag{2.77}$$

The parameter ϵ' is introduced here to track the order of ρ and φ in the `REDUCE` notebook shown in Section A.3 and should not be confused with the asymptotic expansion perturbation parameter ϵ. After substituting the perturbed plane wave (2.77) into the CGLE (2.69), the resulting expression is linearised in ρ and φ by setting $(\epsilon')^2 = 0$. Taking the real and imaginary parts of the equation yields the following PDEs for the amplitude and phase perturbations

$$\rho_T = \delta\rho_{XX} - 2\delta k\varphi_X - 2|\mathcal{R}|^2\rho \tag{2.78}$$

$$\varphi_T = \delta\varphi_{XX} + 2\delta k\rho_X - 2|\mathcal{R}|^2\rho c. \tag{2.79}$$

The perturbations, approximated by plane waves, are assumed to grow exponentially with growth rate g while their wavelengths are assumed to be large compared to the wavelengths of the plane waves, i.e. their wavenumber $|q| \ll 1$. Both perturbations are combined into a vector form

$$\begin{bmatrix} \rho \\ \varphi \end{bmatrix} = \begin{bmatrix} \hat{\rho} \\ \hat{\varphi} \end{bmatrix} e^{gT+iqX} \tag{2.80}$$

where $\hat{\rho}$ and $\hat{\varphi}$ are real constants. Substituting this expression into the equations (2.78) and (2.79) leads to the following eigenvalue problem

$$g \begin{bmatrix} \hat{\rho} \\ \hat{\varphi} \end{bmatrix} = \begin{bmatrix} -2|\mathcal{R}|^2 - \delta q^2 & -i2\delta kq \\ -2|\mathcal{R}|^2 c + i2\delta kq & -\delta q^2 \end{bmatrix} \begin{bmatrix} \hat{\rho} \\ \hat{\varphi} \end{bmatrix}. \tag{2.81}$$

An approximate expression for the possible growth factors can now be calculated from the eigenvalues of (2.81) by expanding in powers of q. The real part of the growth rate has two possible solutions, which up to the order of $\mathcal{O}(q^2)$ are

$$Re\{g\} = (-1 \pm 1)|\mathcal{R}|^2 + 2\delta \left[\frac{c^2+1}{|\mathcal{R}|^2} - \left(c^2 - \frac{3}{2} \right) \right] q^2. \tag{2.82}$$

Therefore, the solution with the negative sign is dominated by the leading term $-2|\mathcal{R}|^2$ which results in a decaying perturbations and stable waves. However, taking the positive sign in (2.82) can lead to $Re\{g\} > 0$ and growing perturbations. The critical condition for such instability can be derived by calculating when the coefficient of q^2 becomes greater than zero. This yields the critical value for the squared modulus of the amplitude of the unperturbed waves which reads

$$|\mathcal{R}|^2 < \frac{c^2+1}{c^2+\frac{3}{2}}. \tag{2.83}$$

Thus, if the amplitude of the waves falls below a certain critical value, they become unstable due to the Eckhaus instability. This prediction is confirmed in numerical experiments detailed in Sections 4.2 and 4.3.

The condition on the amplitude of the waves (2.83) can be also expressed in terms of the wavenumber k of the unperturbed waves to produce

$$\delta k^2 > \frac{1}{3+2c^2}. \tag{2.84}$$

The condition on the wavenumber (2.84) can be checked for consistency by referring to Aranson *et al.* (1992) or Weber *et al.* (1992) where a similar perturbative treatment was used to derive the Eckhaus criterion.

More intuitively, the Eckhaus instability can be associated with the decrease in the wavelength of the plane waves below a critical value defined as

$$\lambda < 2\pi\sqrt{\delta(3+2c^2)}. \tag{2.85}$$

This general rule appears to hold even in regimes where the CGLE approximation is not longer valid as the onset of the Eckhaus-like instability is usually accompanied by a decrease in the wavelength as discussed in Section 5.5.

* * *

As mentioned throughout this chapter, the notebooks for the computer algebra system `REDUCE` (Hearn, 2004) complementing the analytical derivations are listed in Appendix A. These notebooks reproduce the main mathematical results and are provided with comments linking the source code to the derived equations.

Chapter 3

Computational Methods

> Inserted debug statements into `anomdtb.f90`, discovered that a sum-of-squared variable is becoming very, very negative!
>
> UEA Climategate files

3.1 Computational Introduction

As in many areas of science, computer simulations became an important research method complementing experimental techniques in biology. The main objective of such numerical experiments is to compare their results with the theoretical predictions obtained through mathematical analysis. In order to guarantee further discoveries in the field of computational biology, appropriate models which balance realistic complexity with mathematical tractability need to be developed. However, as the analytical tools progress to describe more complicated models, their predictions may not be fully utilised if a direct comparison to numerical results is not feasible. Simulations of more complex systems pose certain challenges, however, they offer a possibility to study phenomena such as maintenance of biodiversity through formation of stable patterns as explored in this thesis.

3. COMPUTATIONAL METHODS

The history of individual based simulations in computational biology spans several decades and can be characterised by a trend of adopting established methods used to simulate chemical reactions. Early simulations of spatially structured populations consisted of simplified cellular automatons (Boon *et al.*, 1996; Ziff *et al.*, 1986) with biologically motivated rules (Rozenfeld & Albano, 1999). It was assumed that synchronously updating the system across the entire spatial domain at each time step did not affect the dynamics of the system. However, this meant that such dynamics was defined by the initial conditions which evolved deterministically into a steady or an oscillating state due to the finite number of all possible configurations (Nowak & May, 1992). To correct this unrealistic situation, an asynchronous and randomised updating was introduced to capture the stochastic nature of the biological dynamics (Huberman & Glance, 1993). This approach is often referred to as the Monte Carlo simulation. Despite initial claims of little importance to the dynamics (Nowak *et al.*, 1994), this update scheme was adopted by researchers because of its more realistic nature. The popularity of such approach has grown and the lattice based Monte Carlo simulations became the default way of modelling spatial populations.

Nevertheless, while being the de-facto standard, simulations which are often referred to as lattice Monte Carlo (LMC) are far from standardised. In fact, the algorithm for performing such simulations given a particular stochastic system was never formalised while the source codes are not published. There exist a handful of rules which are usually present in various implementation but inclusion of all is not guaranteed. Therefore, there is no lattice Monte Carlo algorithm, only a loosely defined set of instructions which are often interpreted in different ways. With the absence of a predefined procedure, there exists a number of different implementations which do not accurately simulate the stochastic systems. A modeller is free to pick and choose the different features of the algorithm, often introduced to correct well known discrepancies with the theoretical predictions. It is usually difficult to know which implementation is used as a detailed description of the algorithm, allowing for a good degree of reproducibility, appears only in a selection of papers (Antal & Droz, 2001; Boccara *et al.*, 1994; Droz & Pekalski, 2004; Lipowski, 1999; Lipowski & Lipowska, 2000; Mobilia *et al.*, 2007; Pekalski, 2004; Provata *et al.*, 1999; Satulovsky & Tom, 1994; Washenberger *et al.*, 2007;

Wodarz *et al.*, 2012). The ability to solve the underlying stochastic process by the lattice Monte Carlo simulations remains unproven while analytical arguments suggest that LMC does not generate accurate realisations of the underlying microscopic dynamics as explained in Section 3.2. Fortunately, improving the LMC approach to perform more accurate simulations is not necessary since there already exists another method generating exact realisations of a stochastic process.

The Gillespie algorithm is rigorously defined in terms of the dynamics of the stochastic system and it is mathematically proven to provide statistically exact solutions (Anderson, 2007; Cao *et al.*, 2004; Erban *et al.*, 2007; Gibson & Bruck, 2000; Gillespie, 1976; Li & Petzold, 2006; Roberts *et al.*, 2013; Twomey, 2007). The reader is encouraged to study an excellent introduction to the algorithm along with a thorough review of its various modifications in Gillespie (2007). The results of the stochastic simulations were compared successfully to the solutions of macroscopic ODEs while also predicting new phenomena not captured by the deterministic equations (McKane & Newman, 2005; Traulsen *et al.*, 2005). The usual implementation of the Gillespie algorithm for well-mixed systems can be extended to simulate spatial dynamics and such studies were already performed successfully in one dimension (Lugo & McKane, 2008; McKane *et al.*, 2013).

The following sections contain the details of the bespoke computational framework modelling the two-dimensional model inspired by the bacterial dynamics described in Section 1.1. The framework consists of three complementary computer programs solving the Master equation (2.16), the macroscopic PDEs (2.26) and the CGLE (2.69) which are derived in Chapter 2. As mentioned above, the lattice Monte Carlo simulations possess certain limitations which make them unsuitable for simulations required in this research. More concrete example of simulating a simple toy model using LMC is provided in Section 3.2 along with the comparison to exact results from the Gillespie approach.

A lattice Gillespie algorithm used in this research was developed to simulate large metapopulation lattice systems as explained in Section 3.3. The increased efficiency was achieved by the use of a binary tree data structures which reduced the computational complexity from $\mathcal{O}(L^2)$ to $\mathcal{O}(\ln L)$. Finally, some details of implementing the second order exponential time differencing method (ETD2), such as the dealiasing procedure, are provided in Section 3.4.

3.2 Lattice Monte Carlo

One of the major problems with the lattice Monte Carlo simulations is a priori assumption that all events are separated by a constant time step. This distorts the time evolution of the dynamics as there is no distinction between slow and fast rates since a reaction must occur at each time step. In addition, the time is measured in the so-called Monte Carlo steps which consists of some number of the constant time steps. This number is usually the system size, interpreted as the total number of lattice sites, while some implementations rescale by the number of individual currently present in the system (Krebs *et al.*, 1995). This makes it difficult to trust measurements of any time related quantities such as velocities or frequencies obtained from these simulations (Case *et al.*, 2010).

Another problem of the LMC approach stems from the inappropriate way of choosing the next reaction since the usual methods do not reflect the probabilities of the reactions. Such probabilities, also referred to as propensities, should be based on the relative reaction rate and the possible number of reactions in the current state. Therefore, the choice of interacting pairs requires careful implementation or additional corrections in the reactions rates. An example of such correction appears in some papers where choosing an occupied site and its neighbour means that a pair of individuals is chosen twice as often as an individual neighbouring an empty site (Krebs *et al.*, 1995).

To present the inconsistencies of the LMC approach, a simplified predator-prey system is defined with S_1 (predator) and S_2 (prey) strains. The only allowed reactions are the removal of S_2 upon a contact with the dominant S_1 at rate σ and the movement of S_1 to the right across empty spaces at rate δ_D. In addition, the total propensity from the Gillespie algorithm, a_0, is defined as the sum of rates of all reactions that can occur at a given instance (Gillespie, 2007).

The evolution of such system can be easily envisioned, the S_1 strain explores the lattice sites, removing individuals of S_2 strain which remain stationary. Considering first a one dimensional chain of three agents with non-periodic boundary conditions and an initial state of $S_1S_2S_2$ it is clear that the next two states of the system are $S_1\emptyset S_2$ and $\emptyset S_1S_2$. According to the Gillespie algorithm, the waiting times are exponentially distributed and the time elapsed between these states is

$-\ln(r_u)/a_0$ where r_u is an uniform random number in the interval $(0, 1]$ and a_0 is the total propensity for each state. In the first stage, only a removal of S_2 is possible whereas at a later time hopping of S_1 to the right is the only allowed event. Therefore, the mean waiting times are $1/\sigma$ and $1/\delta_D$ respectively as the factor of $-\ln(r_u)$ averages to unity.

A typical interpretation of the lattice Monte Carlo simulation would carry out the procedure in a different way with both events separated by a constant time step. As this is not a realistic approach, a more sensible method used in Krebs *et al.* (1995) is applied even though it is not normally utilised in the field of population modelling. Firstly, a lattice site needs to be picked along with one of its neighbours. However, there is only one reactive pair per each state, S_1S_2 or $S_1\emptyset$, and the pair choosing is not necessary. Once a pair is picked, a predefined small time step dt is multiplied by rates of possible reactions between the two lattice sites to give a probability of an event happening in time interval $[t, t+dt)$. Here, the situation is again simplified as there is only one possible reaction in first two stages of the system. Subsequently, a uniform random number r is generated. If $r_u \leq \delta_D dt$ or $r_u \leq \sigma dt$ is satisfied, depending on which reaction is considered, the event is chosen to happen. This procedure puts a limit on the value of dt since true randomness is achieved only if most of the small time intervals elapse without a single reaction happening. Small values of dt mean that most of the generated random numbers are wasted, particularly in the case of reactions happening on different time scales. Assuming that the removal of S_2 is much less likely than the hopping with $\sigma \ll \delta_D$, the small time interval must satisfy $dt \ll \sigma$ to give appropriate level of randomness. Therefore, waiting for $r \leq \sigma dt$ during the first stage takes a long time, requiring many random numbers which are not utilised.

Choosing which reaction should occur is another problem in LMC technique. In Gillespie algorithm, all the possible reactions from all lattice sites are weighted by their respective rates. A uniform random number is then used to decide which one is to happen. For example in state $\emptyset S_1 S_2$, if hopping to the left was allowed, the selection and diffusion reactions would be possible with respective probabilities of $\sigma/(\delta_D + \sigma)$ and $\delta_D/(\delta_D + \sigma)$. In contrast, LMC approach requires choosing a lattice site and one of its neighbours. The system is then evolved as described

previously. Therefore, the simulation depends not only on the value of dt and generated random numbers but also on the way of choosing pairs. Usually, an agent is picked and then, with equal probabilities, one of its neighbours. The two chosen individuals are considered only if there is a possible reaction between them and in the case of this simplified system only S_1S_2 and $S_1\emptyset$ are allowed. However, the descriptions of the LMC algorithms do not usually make clear whether empty spaces can be chosen as the first lattice site which implies that S_1S_2 is picked twice as frequently as $S_1\emptyset$. This incorrect approach must then be amended by additional factors in the reaction rates (Krebs *et al.*, 1995).

To see another inconsistency of LMC approach, an initial chain $S_2S_1S_2$ is considered where hopping of S_1 is no longer allowed. Second stage of this systems is either $\emptyset S_1S_2$ or $S_2S_1\emptyset$ with the final state being $\emptyset S_1\emptyset$. Calculating total propensities at each state, the Gillespie algorithm predicts that mean time intervals between the three stages are exactly $1/(2\sigma)$ and $1/\sigma$. However, according to LMC simulation, the states are separated by equal time periods on average since both require $r_u \leq \sigma dt$ to be satisfied. Therefore, the time interval is computed without taking into account the delay originating from a smaller number of possible reactions. In addition, the two most common LMC time rescalings, dividing by the lattice size and the number of agents left on a lattice, fail to correct these time intervals.

Since one the objectives of this postgraduate research was to validate the correctness of micro- and macroscopic descriptions of the generic model by direct comparison of the generated results, the Gillespie algorithm was used in simulating the stochastic system. This ensures a correct time evolution and reliable results for all time-dependent quantities which cannot be guaranteed by the lattice Monte Carlo simulations (Case *et al.*, 2010).

```
1  func update_tree(node_coord) {
2      parent = parent_of(node_coord)
3      value_of(parent) = value_of(left_child_of(parent))
4                       + value_of(right_child_of(parent))
5      if (has_parent(parent)) {
6          update_tree(parent)
7      } else {
8          return
9      }
10 }
```

Listing 3.1: Pseudocode of the recursive function updating the tree of propensities. The input variable `node_coord` is the coordinate of a node in the tree. Initially, the functions is called with coordinate of the leaf node whose value has changed. The function is then called recursively until the parentless root node is reached.

3.3 Lattice Gillespie Algorithm

In the original Gillespie algorithm, the time taken for the accumulation of reaction propensities, and the subsequent choice of the next reaction, scales with the total number of reactions (Gillespie, 2007). Therefore, the standard algorithm is relatively efficient only when a small number of reactions is considered. This is certainly not the case for the metapopulation lattice system where millions of reaction are possible. Their number is proportional to the lattice size L^2 meaning that the accumulation of propensities as well as the reaction search require computational complexity of order $\mathcal{O}(L^2)$. The search can be optimised through various algorithms to run at order $\mathcal{O}(\ln L)$ (Li & Petzold, 2006), however, the summation of propensities occurs then at order $\mathcal{O}(L^2)$. In this thesis, an improved algorithm based on the direct method is presented, in which not only the search but also the accumulation occurs at logarithmic complexity allowing for $\mathcal{O}(\ln L)$ scaling of the entire algorithm. This novel approach is based on storing the reaction propensities in a binary tree data structure (Knuth, 1968) while a similar approach utilising the direct methods and the next reaction method can be found in Elf & Ehrenberg (2004). In order to make the implementation as simple as possible, the binary tree is extended up to the level of individual lattice

```
1  func reaction_search(node_coord, rand) {
2      if (has_children(node_coord)) {
3          if (rand < value_of(left_child_of(node_coord))) {
4              reaction_search(left_child_of(node_coord), rand)
5          } else {
6              rand = rand - value_of(left_child_of(node_coord))
7              reaction_search(right_child_of(node_coord), rand)
8          }
9      } else {
10         i, j = get_site_coords(node_coord)
11         for (r = 0; r < NUM_OF_REACTIONS; r++) {
12             rand = rand - propensity(i, j, r)
13             if (rand < 0.0) {
14                 return i, j, r
15             }
16         }
17     }
18 }
```

Listing 3.2: Pseudocode of the recursive next reaction search function. The input parameter `node_coord` is the coordinate of the parent node while `rand` is a random number. Initially, the function starts from the top of the tree and is then called recursively with the coordinate of one of the children. It should be noted that the value of `rand` must be decreased when descending to the right. After a leaf node is reached, the corresponding lattice site coordinates `i` and `j` are obtained along with the reaction number `r` as in the standard direct method.

sites while the on-site search is performed by the standard technique. Since the number of possible birth, selection and mutation reactions inside one population is constant, the on-site search is essentially an order $\mathcal{O}(1)$ process.

The binary tree is built starting from the lowest level where each leaf holds the sum of the propensities in one subpopulation, with an example for $L^2 = 4^2$ representable as a 4 by 4 array

$$\begin{bmatrix} 0.01 & 0.02 & 0.03 & 0.04 \\ 0.05 & 0.06 & 0.07 & 0.08 \\ 0.09 & 0.10 & 0.11 & 0.12 \\ 0.13 & 0.14 & 0.15 & 0.16 \end{bmatrix} \rightarrow (3.2). \tag{3.1}$$

```
func update_propensities(i, j, reaction_num) {
    update_site(i  , j  )
    update_site(i-1, j  )
    update_site(i  , j-1)
    if (is_migration_reaction(reaction_num)) {
        if (is_in_i_direction(reaction_num)) {
            update_site(i+1, j  )
            update_site(i+1, j-1)
        } else {
            update_site(i  , j+1)
            update_site(i+1, j+1)
        }
    }
}
```

Listing 3.3: Pseudocode of the function updating the leaves in the binary tree of propensities. Depending on the reaction number, only the affected neighbours of the population at coordinates `i` and `j` are updated.

The next layer is a sum of pairs in each row while the following layer consists of summed pairs in each column. The process, presented in Listing 3.1, is repeated until arriving at the root of the tree which holds the value of the total propensity producing the remaining structure of the binary tree

$$(3.1) \rightarrow \begin{bmatrix} 0.03 & 0.07 \\ 0.11 & 0.15 \\ 0.19 & 0.23 \\ 0.27 & 0.31 \end{bmatrix} \rightarrow \begin{bmatrix} 0.14 & 0.22 \\ 0.46 & 0.54 \end{bmatrix} \rightarrow \begin{bmatrix} 0.36 \\ 1.00 \end{bmatrix} \rightarrow \begin{bmatrix} 1.36 \end{bmatrix}. \tag{3.2}$$

When a reaction occurs at a certain patch, the total propensity associated with that patch changes and the binary tree needs to be updated in turn. However, this procedure can be done simply by updating only relevant entries along the branches with $\mathcal{O}(\ln L)$ complexity. The search is done by comparing the randomly generated number with the entries at each level, subtracting the cumulative sums when necessary as shown in Listing 3.2. After the reaction is chosen and executed, the tree has to be updated. However, since each reaction affects only the nearest neighbour populations, only a small number of propensities needs updating as shown in Listing 3.3. This works to speed up the simulations in a similar fashion to dependency graph methods (Gibson & Bruck, 2000).

3.4 Exponential Time Differencing

At the macroscopic level, the dynamics of the generic metapopulation model can be described by the PDEs (2.26) which in turn are approximated by the CGLE (2.69). These macroscopic descriptions are solved with a pseudo-spectral method called exponential time differencing (ETD) of second order (ETD2) using a time step of $\Delta t = 0.125$ in all numerical experiments. A detailed analysis of ETD, discussing accuracy, stability and a comparison to other methods can be found in Cox & Matthews (2002). More interestingly, the actual computational implementation can be found in the open source code of `OpenCGLE` discussed in Section 3.5. In addition, a short description of the dealiasing process, added as an enhancement to the ETD scheme, is given below in Section 3.4.1.

An important different between the stochastic and deterministic simulations is the additional grid size parameter G^2 specifying the number of discrete points representing the patterns in the domain of size L^2. Metapopulation lattice can be thought of as having $L^2 = G^2$ while the ETD method allows $L^2 \neq G^2$. Therefore, the spatial coordinate $\mathbf{x} = (\mathbf{g}/G)L$ becomes continuous as $G \to \infty$ with $\mathbf{g} = (g_1, g_2)$ being the position of the grid point. This has a consequence on the resolvability of the patterns emerging in the simulations and the important issue of resolution effects is discussed in Section 5.4.

It should be noted that the PDEs (2.26) are integrated after the origin is moved to the fixed point s^* (2.23) via $\tilde{s}_i = s_i - s^*$ as described in Section 2.3.1. Separating the diagonal terms in $\tilde{s}_i$ from the off-diagonal terms (ODT), the redefined PDEs can be represented as

$$\begin{aligned} \partial_t \tilde{s}_i = &\Big((1-4s^*)\beta - s^*\sigma - 2\mu\Big)\tilde{s}_i + \delta_D \nabla^2 \tilde{s}_i - 2s^*(\delta_D - \delta_E)\nabla^2 \tilde{s}_i \\ &+ \mathrm{ODT}(\tilde{s}_{i+1}, \tilde{s}_{i-1}, \tilde{s}_i\tilde{s}_{i+1}, \tilde{s}_i\tilde{s}_{i-1}, \tilde{s}_i\nabla^2\tilde{s}_{i+1}, \tilde{s}_i\nabla^2\tilde{s}_{i-1}, \tilde{s}_{i+1}\nabla^2\tilde{s}_i, \tilde{s}_{i-1}\nabla^2\tilde{s}_i) \end{aligned} \tag{3.3}$$

while their full expression can be obtained with the `REDUCE` notebook listed in Section A.4. As a result of this transformation, the nonlinear terms such as $(\tilde{s}_{i+1} + \tilde{s}_{i-1})\Delta\tilde{s}_i$ generate linear diagonal terms such as $-2s^*(\delta_D - \delta_E)\Delta\tilde{s}_i$ which can be solved exactly by the ETD method. In addition, the off-diagonal terms in $s_{i\pm1}$ are solved as nonlinear terms avoiding calculations of matrix exponentials.

```
for (i = 0; i < grid_pts_x; i++) {
    for (j = 0; j < grid_pts_y; j++) {
        if ((k_abs_x[i] == k_dealias_x and
             k_abs_y[j] <= k_dealias_y) or
            (k_abs_x[i] <= k_dealias_x and
             k_abs_y[j] == k_dealias_y)) {
            dealias_mask[i][j] = ETD_DEALIAS_EDGE;
        } else if (k_abs_x[i] < k_dealias_x and
                   k_abs_y[j] < k_dealias_y) {
            dealias_mask[i][j] = ETD_DEALIAS_KEEP;
        } else {
            dealias_mask[i][j] = ETD_DEALIAS_LOSE;
        }
    }
}
```

Listing 3.4: Pseudocode of the loop initialiasing the dealiasing mask. The absolute values of the wave numbers in x and y direction are compared to the cutoff values set by the dealiasing factor. If the values are to be kept after the dealiasing, the constants `ETD_DEALIAS_KEEP` or `ETD_DEALIAS_EDGE` are set to the mask. Otherwise, the mask assumes the value of `ETD_DEALIAS_LOSE` which indicates that the Fourier modes corresponding to the particular wavenumbers will be removed. See Listing 3.5 for example of a dealiasing mask.

3.4.1 Dealiasing

An important issue in implementation of the ETD scheme is the aliasing of Fourier modes (Press *et al.*, 2007). The well-known fact of the sampling theorem defines a critical Nyquist frequency f_{Nq} specifying a limit on the bandwidth which can be resolved on a discrete grid. As a consequence, any frequencies outside of the bandwidth are aliased into that range of frequencies introducing numerical errors. One concrete example of aliasing considers an expression in $\cos(2\pi f_{Nq})$ where f_{Nq} is the aforementioned critical frequency. Calculations of any nonlinear terms, in which such expression is squared, produce terms in $\cos(4\pi f_{Nq})$ oscillating at twice the Nyquist frequency. These terms alias into the resolvable bandwidth, introducing errors in the discrete representation of the waves. In order to avoid such errors, the numerical scheme should remove any terms causing an aliasing.

```
 1  1  1  1  2  0  0  0  0  0  0  0  2  1  1  1
 1  1  1  1  2  0  0  0  0  0  0  0  2  1  1  1
 1  1  1  1  2  0  0  0  0  0  0  0  2  1  1  1
 1  1  1  1  2  0  0  0  0  0  0  0  2  1  1  1
 2  2  2  2  2  0  0  0  0  0  0  0  2  2  2  2
 0  0  0  0  0  0  0  0  0  0  0  0  0  0  0  0
 0  0  0  0  0  0  0  0  0  0  0  0  0  0  0  0
 0  0  0  0  0  0  0  0  0  0  0  0  0  0  0  0
 0  0  0  0  0  0  0  0  0  0  0  0  0  0  0  0
 0  0  0  0  0  0  0  0  0  0  0  0  0  0  0  0
 0  0  0  0  0  0  0  0  0  0  0  0  0  0  0  0
 0  0  0  0  0  0  0  0  0  0  0  0  0  0  0  0
 2  2  2  2  2  0  0  0  0  0  0  0  2  2  2  2
 1  1  1  1  2  0  0  0  0  0  0  0  2  1  1  1
 1  1  1  1  2  0  0  0  0  0  0  0  2  1  1  1
 1  1  1  1  2  0  0  0  0  0  0  0  2  1  1  1
```

Listing 3.5: Dealiasing mask for a grid with $G^2 = 16^2$ and $\frac{1}{2}$ dealiasing factor. The constants `ETD_DEALIAS_LOSE`, `ETD_DEALIAS_KEEP` and `ETD_DEALIAS_EDGE` are represented as `0`, `1` and `2` respectively. The $(k_x, k_y) = (0, 0)$ Fourier mode is placed in the top left corner.

Dealiasing is achieved by removing Fourier modes above a certain wavenumber depending on the highest order of nonlinear terms in the solved equations. In case of the CGLE (2.69), the removal of all modes above $\frac{1}{2} f_{Nq}$ is required due to the cubic terms and is referred to as the $\frac{1}{2}$-dealiasing rule (Phillips, 1959). For the PDEs (2.26), where only quadratic terms are present, the $\frac{2}{3}$-dealiasing rule is sufficient (Orszag, 1971). The removal of the unwanted terms is performed by the dealiasing mask whose initialisation algorithm is given in Listing 3.4. In addition to specifying the kept or lost Fourier modes, the edges of the retained region are also marked as shown in Listing 3.5. This helps monitoring the amplitude of the removed modes which should be significantly smaller than the retained modes in a well resolved numerical experiment. For example, the `OpenCGLE` software, discussed in Section 3.5, requires at least three orders of magnitude difference between the maximum modes from the `ETD_DEALIAS_KEEP` and `ETD_DEALIAS_EDGE` regions shown in Listing 3.5. If such condition is not met, the user of the program is warned about the lack of resolution. This helps determining the appropriate number of grid points G^2 which balance performance and accuracy.

Name	Repository URL	License
`Datum`	https://github.com/bszcz/datum.git	[MIT]
`Pixmap`	https://github.com/bszcz/pixmap.git	[MIT]
`OpenCGLE`	https://github.com/bszcz/opencgle.git	[GPLv2+]

Table 3.1: Summary of the independently developed open source research software inspired by the postgraduate research. Full source code and development history can be obtained by cloning the repositories from the provided URLs.

3.5 Open Source Research Software

A number of independent open source projects (Ince *et al.*, 2012; McCafferty, 2010) was released during the postgraduate research. The projects are written in `C` programming language (Kernighan *et al.*, 1988), version controlled with `git` (Chacon & Hamano, 2009; Prlić & Procter, 2012; Wilson *et al.*, 2014) and released under open source licenses (Morin *et al.*, 2012) as summarised in Table 3.1.

The first library called `Datum` is an input/output library designed for storage of numerical arrays. The human readable plain text format of `Datum` files allows for maximum flexibility and compatibility with other tools and programming languages. In addition, the software supports optional compression in `GZ` and `BZ2` standards performed transparently upon reading and writing of data.

The second library, `Pixmap`, enables creation of lossless bitmap images in `PPM`, `PPM.GZ` and `PNG` formats as well as in the lossy `JPEG` standard with optional adjustments of quality and chroma subsampling. This library was used to visualise the results from a majority of simulations presented in this thesis.

`OpenCGLE` is a pseudo-spectral solver of the complex Ginzburg–Landau equation implementing the exponential time stepping methods of 1st and 2nd order. The main part of the project is a modular ETD library which can be separated for reuse in other software. The module utilises `FFTW3` library (Frigo & Johnson, 1998, 2005) and allows for threaded parallel execution. The input and output of data and images in `OpenCGLE` are performed with `Datum` and `Pixmap` libraries.

Chapter 4

Results: Complex Ginzburg–Landau Equation

The complex Ginzburg-Landau equation (CGLE) is a celebrated pattern forming system exhibiting spiral waves. The most well-known application of the CGLE is the modelling of Belousov–Zhabotinsky reaction in which periodically oscillating reactants form a chemical clock (Smolka *et al.*, 2005; Zaikin & Zhabotinsky, 1970). Another interesting example of spiral formation can be found in the aggregation of unicellular amoeba *Dictyostelium discoideum* by the process of chemotaxis (Pálsson & Cox, 1996; Pálsson *et al.*, 1997; Tyson & Murray, 1989). In both cases, the visual appearance of the evolving system bears striking resemblance to the numerical solutions of the CGLE as shown in Figure 4.1.

This chapter summarises the results related to the two-dimensional complex Ginzburg–Landau equation (2.69) derived in Section 2.3.3. These results are provided here to complement the discussion on the generic metapopulation model which can be approximated by the 2D CGLE. The equation, and the spiral waves it exhibits, were studied for decades with numerous publications covering analytical and numerical aspects of the subject as reviewed in Aranson & Kramer (2002). Nevertheless, a rigorous mathematical analysis of the properties and stability of the spiral patterns in the context of cyclic dominant models is missing from the previous studies as explained in Section 2.3.4.

Figure 4.1: Spiral waves in a biological and a chemical system. Left panel: chemotactic movements of amoeba population reproduced from [BiophysikBildergalerie]. Centre panel: the Belousov–Zhabotinsky chemical reaction reproduced from [ChemWiki]. Right panel: numerical solution of the two-dimensional CGLE with phase of the complex amplitude encoded in greyscale.

Moreover, with the rapid advancement in the computational power, it is now possible to reproduce the original results with much higher quality. For example, the simulations reported here have up to 10^3 times as many Fourier modes as the original results performed on the CRAY YMP supercomputer (Aranson *et al.*, 1993) allowing for exploration of previously inaccessible regimes.

4.1 Four Phases

One of the main aims of this research is to confirm the existence of the four CGLE phases in the generic metapopulation model. However, it is useful to study them first in the actual CGLE to understand the nature of those regimes in more detail. Based on the formula for the variable c (2.70) in the derived CGLE (2.69), the phase diagram of the original system is plotted in Figure 4.2. As mentioned in Section 2.3, setting $\beta = 1$ has no effect on the generality of the results. Therefore, it is sufficient to plot the contours of the parameter c in the $\sigma - \zeta$ plane. The values of $(c_{AI}, c_{EI}, c_{BS}) = (0.845, 1.25, 1.75)$ were approximated from Aranson *et al.* (1993) and divide the diagram into four phases as explained in the caption of Figure 4.2. A snapshot of the four different solutions with values of the parameter

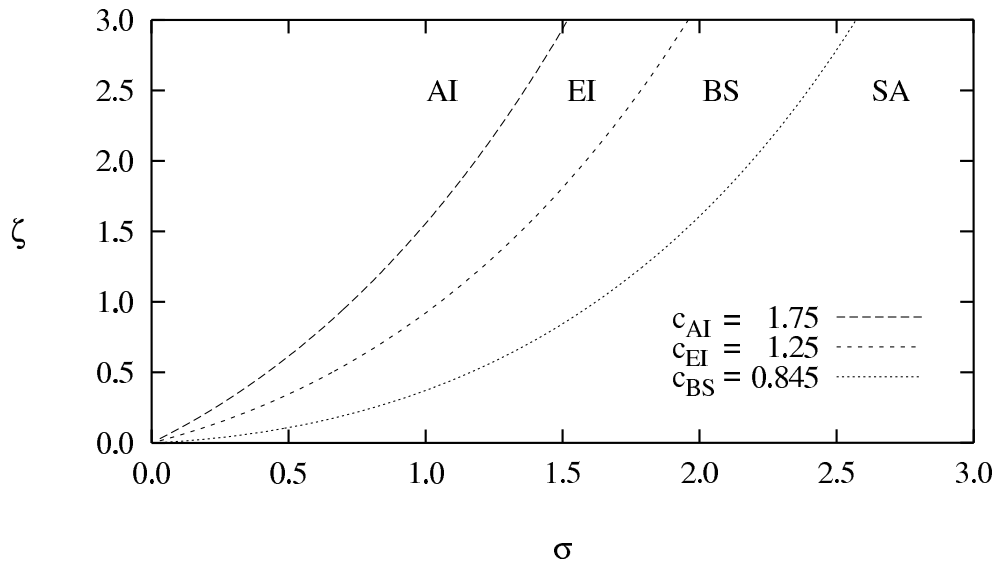

Figure 4.2: The phase diagram of the 2D CGLE (2.69) based on the expression for the parameter c (2.70) with $\beta = 1$. The contours of $c = (c_{AI}, c_{EI}, c_{BS})$ distinguish four phases characterised by absolute instability (AI), Eckhaus instability (EI), bound states (BS) and spiral annihilation (SA). See Section 4.1 for details.

c placed in the four different regions of the phase diagram is shown in Figure 4.3. The images visualise the argument of the complex amplitude $\mathcal{A}$ encoded as hue in which red, green and blue are placed at 0°, 120° and 240° respectively. Such choice of the colour scheme is grounded in the derivation of the CGLE where the values of the phase correspond to the dominance of one of the species. The four values of $c = (2.0, 1.5, 1.0, 0.5)$ used in the numerical experiments are placed conveniently between the three critical values of $(c_{AI}, c_{EI}, c_{BS}) = (0.845, 1.25, 1.75)$. They are also closely related to the values $\beta = \sigma = 1$ and $\zeta = (1.8, 1.2, 0.6, 0)$ used later in the generic metapopulation model simulations which correspond to $c = (1.9, 1.5, 1.0, 0.6)$ respectively via (2.70).

Starting from the rightmost panel of Figure 4.3, the spiral annihilation phase (SA) is characterised by colliding spirals. These annihilate in pairs until a homogeneous oscillating state fills the entire domain. Such deterministic phenomenon is not a result of noise or any type of instabilities and occurs in a relatively short time for low values of c as discussed in Section 4.4. The time for complete anni-

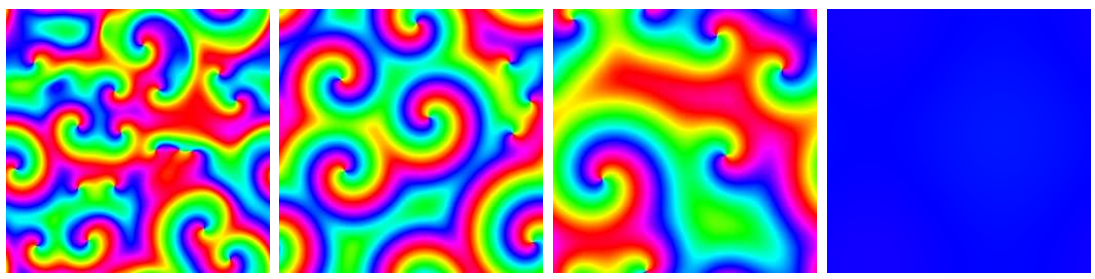

Figure 4.3: Four phases in the 2D CGLE (2.69) for $c = (2.0, 1.5, 1.0, 0.5)$ from left to right. The colours represent the argument of the complex amplitude $\mathcal{A}$ encoded in hue. See Section 4.1 for more detailed discussion of the four phases.

hilation of spirals increases asymptotically with c until $c_{BS} = 0.845$ above which the spirals form bound states (BS). In the next panel with $c = 1.0$, pairs of stable spirals are formed and coevolve. The properties of the spiral arms can be approximated to a good degree of accuracy by the dispersion relation (2.72) following from the plane wave Ansatz (2.71). These states are stable below $c_{EI} = 1.25$ which signifies the onset of the Eckhaus instability (EI). Therefore, in the next panel at $c = 1.5$, the spirals are convectively unstable due to EI which limits the size to which the patterns can grow. However, this effect is not easily observable with many spirals present in the domain since the high density of spirals limits their growth to a larger degree than the Eckhaus instability. Because of the convective nature of the instability, the perturbations are convected away before growing and destabilising the spiral arms in small spirals. This is not the case in the absolute instability (AI) phase where the speed of the spreading perturbations exceeds the speed at which the spiral waves can convect them away. At the critical value of $c_{AI} = 1.75$ any perturbations grow in place until their amplitude destroys the spiral arms whose shapes become significantly distorted. The two situations are depicted in Figure 4.9 while the Eckhaus and the absolute instability are characterised and discussed in more details in Section 4.3. Finally, the argument and the modulus of the solutions to the CGLE for $c = 0.1$ up to $c = 2.0$ in steps of 0.1 are visualised in Figures 4.4 and 4.5 to show a more continuous transition between the four phases.

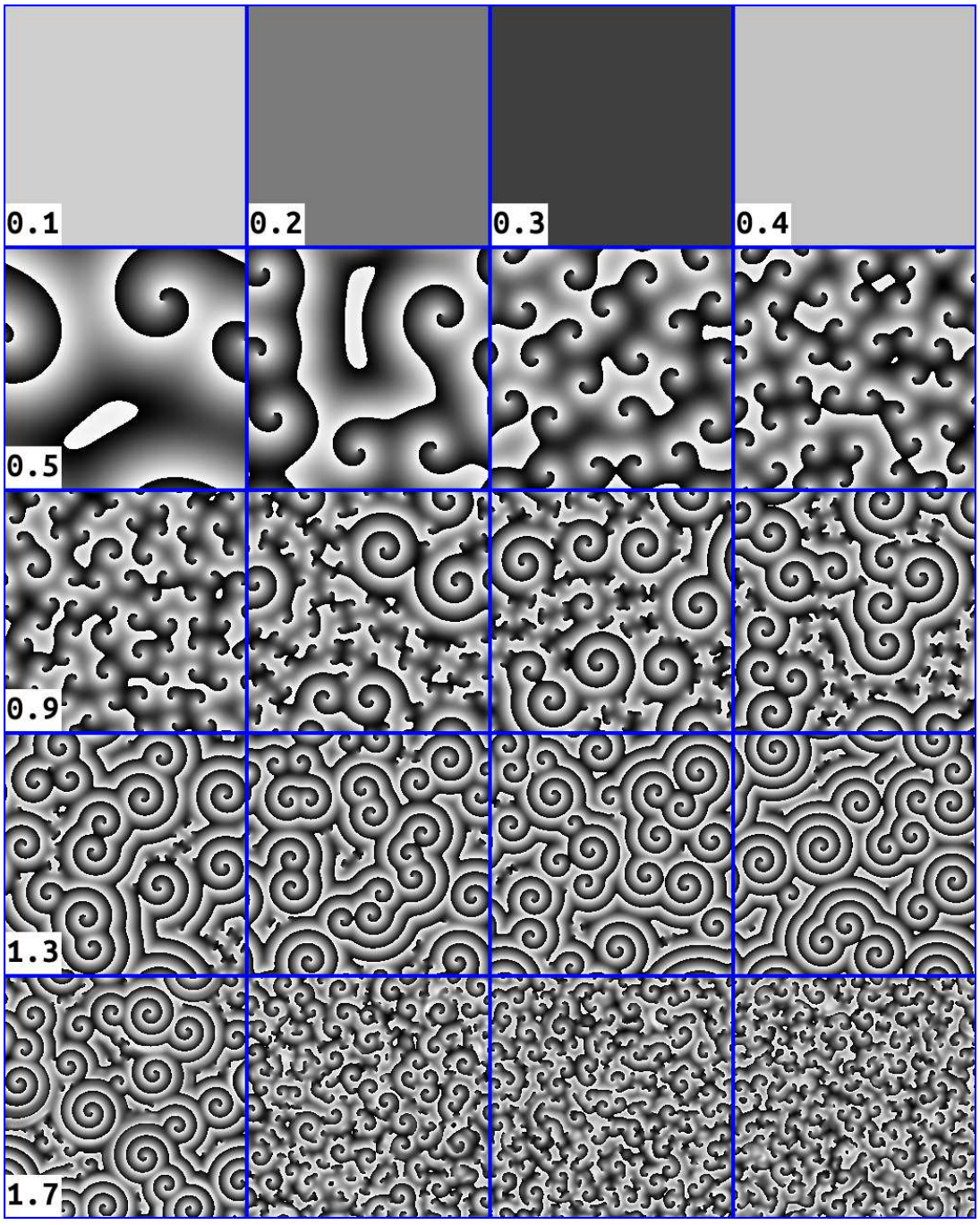

Figure 4.4: Argument of the solutions to the 2D CGLE (2.69) encoded in greyscale. Values of c vary from 0.1 to 2.0 in steps of 0.1 in a zigzag fashion, left to right, top to bottom, as stated in the corner of the frames. The images are taken at time $t = 100000$ with $L^2 = 64^2$, $G^2 = 256^2$ and $\delta = 1$ in all simulations.

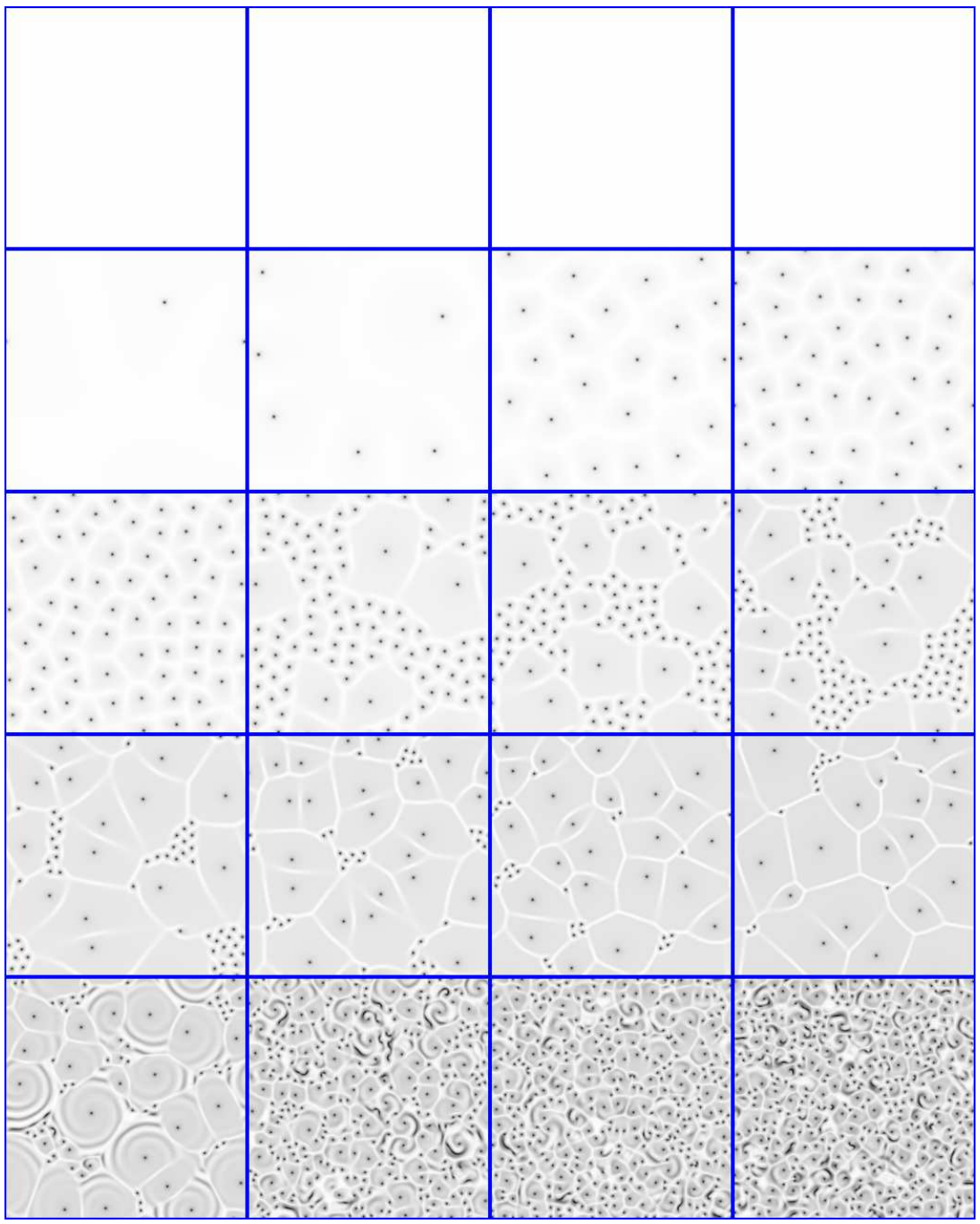

Figure 4.5: Modulus of the solutions to the 2D CGLE (2.69) encoded in greyscale. Bright areas indicate high values of the modulus, dark areas indicate low values. All parameters, including variation of the parameter c, are as in Figure 4.4.

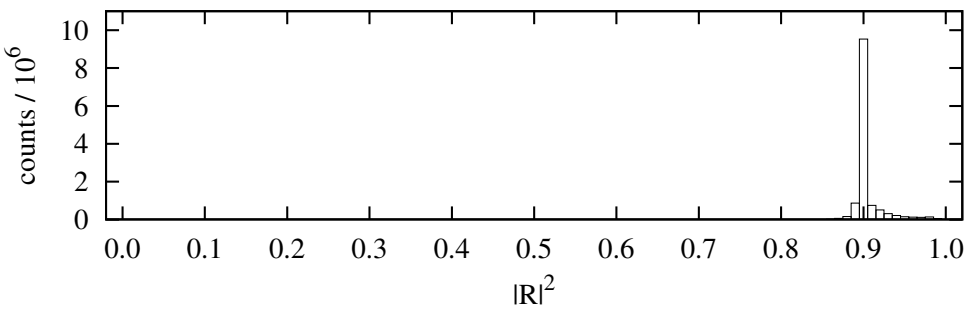

Figure 4.6: Amplitude histogram with 100 bins for $c = 1.0$ averaged over 200 frames between $t = 800$ and $t = 999$ showing a sharp peak at pixel count with $|R|^2 = 0.9$. In comparison, a similar value of $|R|^2 = 0.904444$ is obtained with the technique of global averaging. Both approaches are explained in Section 4.2.

4.2 Amplitude Measurements

In addition to visualising the solutions the two-dimensional complex Ginzburg–Landau equation, the data produced in the experiments can be analysed to confirm the theoretical predictions based on the plane wave Ansatz (2.71) detailed in Section 2.3.4. Despite this naive approximation of the spiral waves, expected to be accurate away from the core, a good agreement is found when predicting the properties of the patterns. The measurements are based on the amplitude of the spiral waves from which their wavelength, velocity and frequency are then calculated as shown in Table 4.1. The amplitude is computed from the solutions of CGLE by globally averaging over the whole domain which allows for a more automated approach and deployment on large datasets. The solutions are integrated initially up to the time $t = 799$ until the spirals are well developed to avoid any transient effects. Then, the amplitude from the successive 200 data frames between $t = 800$ and $t = 999$ are averaged. This gives a total of approximately 1.3×10^7 data points for each value of c as the grid size used in all experiments is equal to $G^2 = 256^2$. The diffusion constant was set to $\delta = 1$ in all simulations.

The global averaging technique is found to be very accurate since the amplitude is usually constant everywhere in the domain excluding small regions where the cores are nucleated as shown in Figure 4.12. In an alternative approach, the

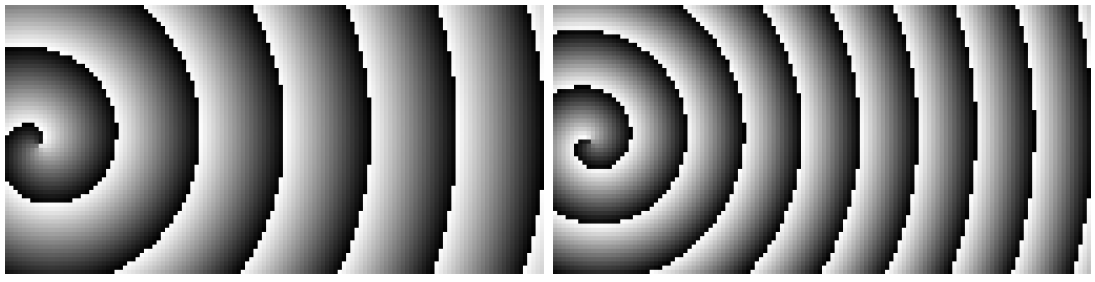

Figure 4.7: Well developed spiral waves at $c = 1.0$ (left) and $c = 1.5$ (right) in the CGLE used for manual wavelength measurements. The spirals for $c = 1.0$ are in the stable phase while for $c = 1.5$ they remain unperturbed due to their small size despite the presence of Eckhaus instability. See Section 4.2 for results.

amplitude can be obtained from a histogram where a distinct peak can be observed at the value of $|R|^2$ as shown in Figure 4.6. However, unless the CGLE is strongly Eckhaus unstable with $c \gtrsim 1.5$, the average stays very close the more accurate value obtained from the histogram since the number of cores in the domain remains small. This claim was verified numerically by comparing results obtained with both methods while also varying bin sizes in the histogram approach. The values from a histogram with 1000 bins and the results of global averaging are compared in Figure 4.8 showing a good agreement.

In addition, the amplitude measurements are also validated by manually calculating the wavelengths of the waves. This process relies on counting the pixels between successive wave fronts in the obtained images. For example, in Figure 4.7 with $L = G$, one pixel corresponds to one spatial unit of the physical domain. Averaging the wavelengths of the five most distant waves from the core, where the plane wave approximation is most accurate, gives a good estimate of the wavelengths in the spiral wave arms. The values obtained from the manual counting are $(20.2, 18.2, 16.8, 15.6, 14.6, 13.8)$ respectively for $c = (1.0, 1.1, 1.2, 1.3, 1.4, 1.5)$ while the values obtained with amplitude measurements and the formula derived from the plane wave Ansatz (2.75) are $(20.3, 18.3, 16.7, 15.5, 14.5, 13.7)$.

Furthermore, the frequency of the phase oscillations is also calculated via a Fourier transform and compared to the predicted frequency obtained from the amplitude measurements. Using the values for the last 300 data frames between

c (2.70)	$\|R\|^2$	λ (2.75)	v (2.76)	ω (2.72)
0.10	0.998826	183.	2.92	0.10
0.20	0.998520	163.	5.19	0.20
0.30	0.997951	139.	6.61	0.30
0.40	0.996919	113.	7.18	0.40
0.50	0.994523	84.9	6.72	0.50
0.60	0.986988	55.1	5.19	0.59
0.70	0.968483	35.4	3.82	0.68
0.80	0.946138	27.1	3.26	0.76
0.90	0.926029	23.1	3.06	0.83
1.00	0.904444	20.3	2.93	0.90
1.10	0.881941	18.3	2.82	0.97
1.15	0.870495	17.5	2.78	1.00
1.20	0.858985	16.7	2.74	1.03
1.25	0.847453	16.1	2.71	1.06
1.30	0.835936	15.5	2.68	1.09
1.35	0.824478	15.0	2.66	1.11
1.40	0.813129	14.5	2.63	1.14
1.50	0.790724	13.7	2.59	1.19

Table 4.1: Global averages of amplitude $|R|^2$ in the CGLE (2.69) for different values of the parameter c (2.70). Other properties of the plane waves, derived from the value of $|R|^2$, are calculated with $\delta = 1$. Additional points at $c = (1.15, 1.25, 1.35)$ are added to more accurately determine the value of c_{EI}. See Section 4.2 for details on the experimental methods.

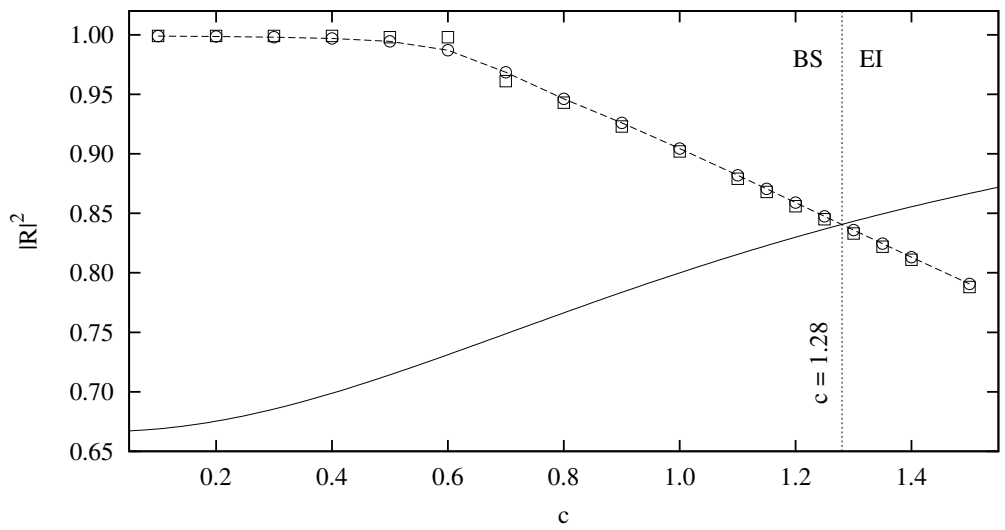

Figure 4.8: Numerical values of $|R|^2$ obtained from a 1000–bin histogram (□) and global averaging (○) with interpolation (dashed line). Dotted line shows the value of $c_{EI} \approx 1.28$ obtained from the experiments. Solid line is the theoretical Eckhaus criterion (2.83) obtained from the plane wave Ansatz in Section 2.3.5.

$t = 700$ and $t = 999$ at $c = 0.9$, a time series for a single point in the domain is extracted. Its frequency spectrum shows a sharp peak at the 40th wavenumber corresponding to $\sin(2\pi\frac{40}{300}t)$ mode. This suggests an angular frequency $\omega = 0.84$ while the value calculated from the plane wave dispersion relation (2.72) is $\omega = 0.83$ resulting in a good agreement with 1.2% discrepancy.

4.3 Instabilities

The plot shown in Figure 4.8 displays the values of $|R|^2$ from Table 4.1 as a function of c along with the derived Eckhaus criterion (2.83). As mentioned in Section 2.3.5, when the amplitude drops below the critical value close to $c_{EI} = 1.25$, the system enters into the EI phase and the spirals become convectively unstable. The convective nature of the Eckhaus instability makes it difficult to confirm the value of c_{EI} which marks the onset of the instability. Below this critical parameter, any small perturbations decay leaving the bound states stable.

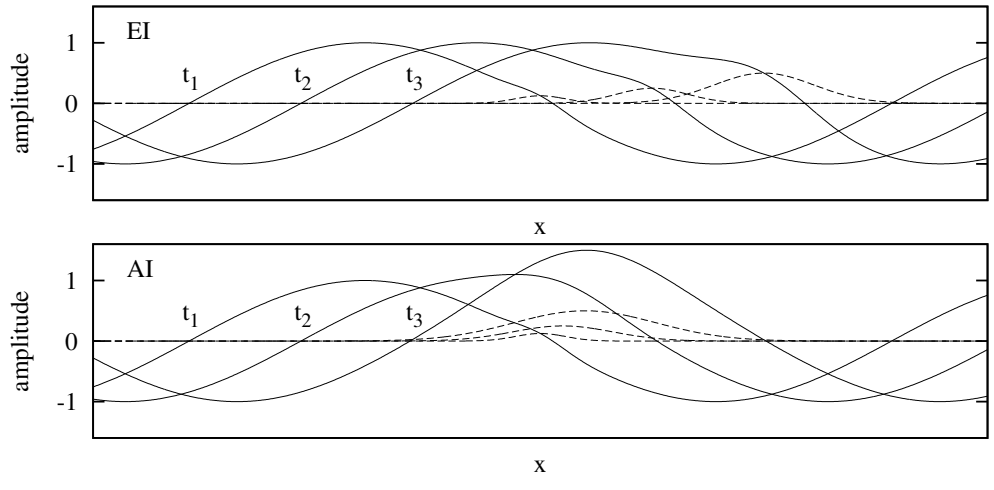

Figure 4.9: Perturbations of plane waves, travelling to the right with $t_1 < t_2 < t_3$, due to the Eckhaus (EI) and absolute (AI) instabilities. Solid lines mark the amplitude of the waves with dashed lines showing the underlying perturbations.

Once c_{EI} is exceeded, the perturbations begin to grow while also being convected away from the spiral core. In small domains, the perturbations reach the boundaries before growing to the necessary amplitude which destabilises the spiral waves. Therefore, extremely large domains are required to see the Eckhaus instability at its onset. This increase in the domain size L has to be coupled with the increase in the grid size G for good resolution as more waves can fit into the domain. It should be noted that the initial conditions must be carefully prepared to ensure that the spirals have enough space to grow to large sizes. Starting from random initial conditions results in nucleation of many spirals whose sizes become limited by their neighbours. Therefore, only two spirals are seeded as shown in the rightmost panel of Figure 4.1. An example of the Eckhaus instability obtained in a simulation with $L^2 = G^2 = 8192$ can be seen in Figure 4.10. Despite this relatively large domain size, the lowest value of c at which the instability can be observed is 1.5 whereas the amplitude measurements suggest $c_{EI} \approx 1.28$. In contrast with Eckhaus instability, the absolute instability can be observed in systems with intermediate domain and grid sizes. Because of the velocity at which the absolute instability spreads, the core is unable to convect away the perturbations which grow in the place of their origin as plotted in Figure 4.9.

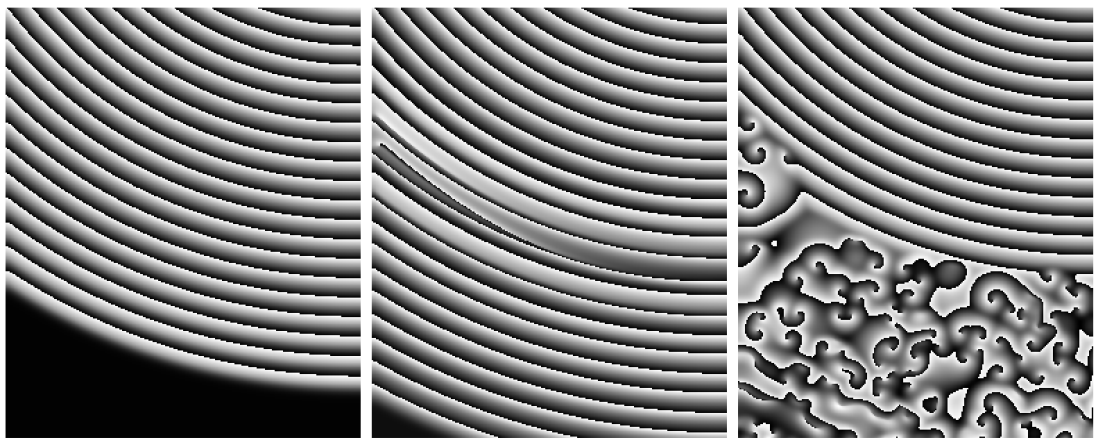

Figure 4.10: The far-field break-up of spirals due to convective Eckhaus instability at $c = 1.5$ in the CGLE. A small part of the image obtained in experiments with $L^2 = G^2 = 8192$ is shown at time $t = 700, 800, 900$ from left to right.

4.4 Spiral Annihilation

The phenomenon of spiral annihilation, predicted from the phase diagram of the 2D CGLE, is a novel discovery in the context of cyclic dominant models. The effect appears to be restricted to the vicinity of the Hopf bifurcation, a regime which remained inaccessible in previous studies of the rock-paper-scissors dynamics lacking the mutation process (2.4). It should be noted that the annihilations are a purely deterministic phenomena resulting from nonlinearities of the CGLE. The collisions and the subsequent loss of all spiral patterns is not an effect of demographic noise or any type of instability. Confirmation of the existence of the phase in the generic model requires, as in the case of Eckhaus instability, intensive computers simulations which were not attempted before.

According to the theoretical results, the stable equilibrium distance between two spirals increases asymptotically as the value of c is lowered to $c_{BS} = 0.845$ which marks the end of the bound state phase (Aranson *et al.*, 1993). In other words, unless the two spirals are separated by an infinite distance, they are destined to annihilate for values below c_{BS}. As to the time before annihilation for a certain separation distance, it increases asymptotically as the value of c is raised until c_{BS} at which it takes an infinite time for the spirals to annihilate.

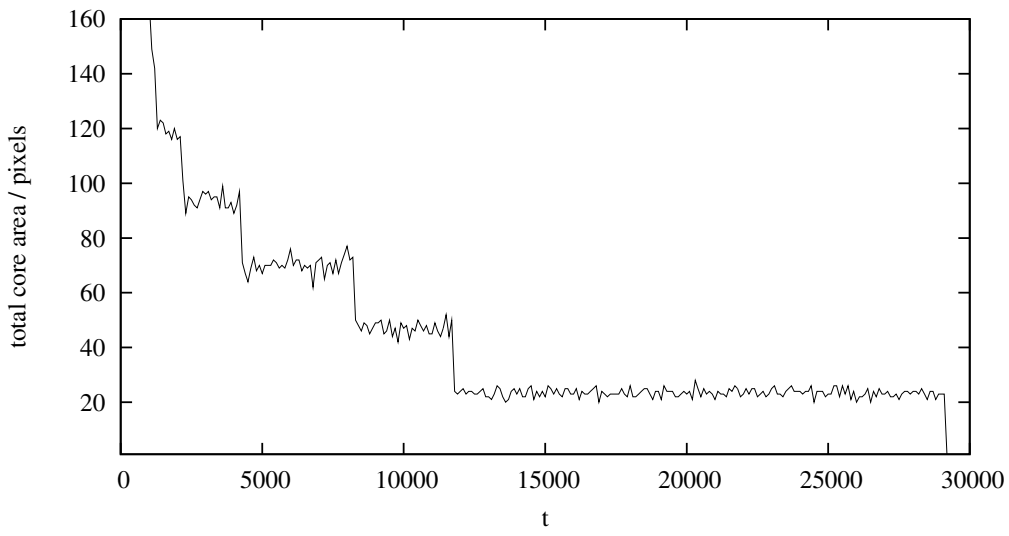

Figure 4.11: Quantised decay of the total core area $|R|^2 < 0.25$ at $c = 0.4$ in the CGLE. After initial transients, 10 spirals remain with a total core area of approximately 120 pixels. Subsequently, five annihilations occur marked by the sharp decreases in the total core area until the disappearance of all spirals.

One way of quantifying the spiral annihilation is tracking the decay of the spiral core area in time. The value of $|R|^2$ is usually of order $\mathcal{O}(1)$ as shown in Table 4.1 and Figure 4.8. However, it drops rapidly to 0 within the small area of the core as shown in Figure 4.12. For a single core, such area remains approximately constant provided that good enough resolution is used in the simulations. Therefore, the total core area becomes a quantised quantity allowing for observations of individual spiral annihilations. These annihilations are manifested as sharp drops in the total core area equal to area of the two colliding cores. An example of such process for $c = 0.4$, where pixels with $|R|^2 < 0.25$ are counted, is presented in Figure 4.11 showing five annihilations and an eventual disappearance of all spirals. The initial transient is characterised by a continuous decrease in the core area since the starting conditions are perturbations around $|R|^2 = 0$. The time periods between first collisions are notably shorter since more spirals are present in the domain. The last annihilation takes longest since the spirals need to move over larger distances to collide. It should also be noted that spirals need to spin in opposite directions in order the annihilate which may prolong their existence in

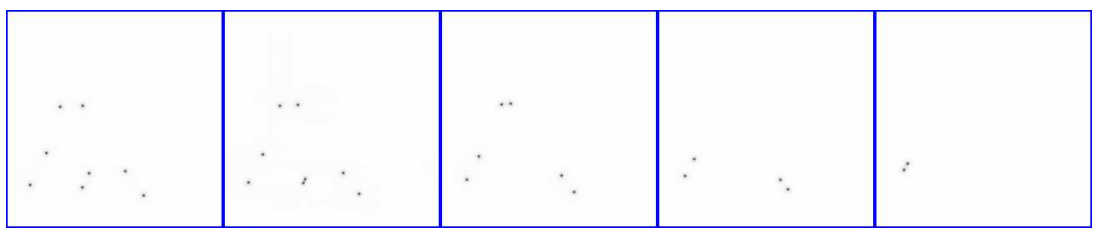

Figure 4.12: Spiral annihilation for $c = 0.1$ in the CGLE. The modulus of the complex amplitude is visualised here with dark pixels representing $|R|^2 \sim 0$ while light pixels show areas with $|R|^2 \sim 1$. Images taken at $t = (1800, 2000, 2200, 2400, 2600)$ respectively from left to right. Blue frame is added in post-processing to outline the boundaries of the domains.

the domain before an appropriate pairing is achieved. A visual representation of spiral annihilation for $c = 0.1$ is also shown in Figure 4.12 where $|R|^2$ is encoded in greyscale. Four pairs of dark spots, signifying the spiral cores with $|R|^2 \sim 0$, are shown colliding and disappearing in a time period of approximately 3000 time steps. In comparison, the numerical experiments for $c = 0.4$ shown in Figure 4.11 take about 30000 time steps before all spirals annihilate.

* * *

As mentioned in the introduction to this chapter, the discussion of the numerical experiments of the two-dimensional complex Ginzburg–Landau equation were presented here to accompany the main results for the generic metapopulation model given in Chapter 5. These rely on approximating the model with the 2D CGLE near the onset of Hopf bifurcation and the predictions of such approach are analysed also in the absence of the bifurcation as in the previous studies.

Chapter 5

Results: Generic Metapopulation Model

Chapter 2 on mathematical methods contains various predictions about the generic metapopulation model based on the novel analysis involving system size and asymptotic expansions leading to the derivation of the macroscopic PDEs (2.26) and the CGLE (2.69). Because the two equations are derived under specific assumptions, the validity of the predictions is tested here as these assumptions are relaxed. The value of the mutation rate μ, related to the perturbation parameter ϵ from the asymptotic expansion through (2.54), is explored here at three different regimes. Firstly, the absence of the Hopf bifurcation is confirmed for $\mu > \mu_H$ with no emerging patterns being observed. The prediction of the existence of four CGLE phases in the generic metapopulation model, as described in Chapter 4, is confirmed at $\mu \sim \frac{1}{2}\mu_H$ implying a relatively large perturbation of $\epsilon \sim 1/4$. All phases can be observed despite the departure from the Hopf bifurcation with the condition of the asymptotic expansion $\epsilon \ll 1$ being no longer satisfied. Finally, in order to relate to the previous studies in which the mutation rate was absent, the system is also simulated at $\mu = 0$ with the limit cycle created by the bifurcation becoming a heteroclinic orbit.

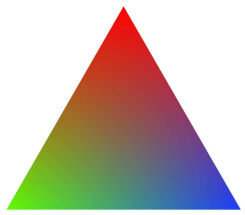

Figure 5.1: Colour-coded simplex of species abundances with total density $r = 1$. Each corner represents complete dominance of one of the species while the middle of the simplex is a grey area around the point $\mathbf{s} = (1/3, 1/3, 1/3)$. The colours fade to black as the total density decreases to $r = 0$.

Furthermore, in contrast with previous studies and wider scientific literature (Joppa *et al.*, 2013; Merali, 2010), the novel computations methods outlined in Chapter 3 are evaluated here with a series of control experiments. Such testing of the algorithms is performed to ensure the correctness of the bespoke computational framework developed in this research. In addition, the control experiments play an important role in proper understanding of the numerical methods whose artefacts may be interpreted as genuine phenomena in the intrinsic dynamics of the generic metapopulation model.

The far-field break-up of spiral waves, a phenomenon resembling the Eckhaus instability (Bär & Brusch, 2004; Bär & Or-Guil, 1999; Ouyang & Flesselles, 1996), is also discussed in this chapter. The initial results obtained from the numerical experiments suggest that the various effects leading to the break-up can be associated with the decrease in the wavelength of the spiral waves. In addition, the nonlinear mobility is found to affect the stability of the spirals in a similar manner without a significant reduction in the wavelength.

The results of the simulations are visualised by colour coding the abundances of the three bacterial strains in each population with appropriate `RGB` intensities such that $(\text{red}, \text{green}, \text{blue}) = (s_1, s_2, s_3)$. An example of this colour scheme is presented in Figure 5.1 where values corresponding to total density $r = s_1 + s_2 + s_3 = 1$ are encoded in `RGB` colours. When the sum of the species frequencies $r < 1$, the colours are darker with the case for $r = 0$ resulting in black colouring. Each pixel in the images shown in this chapter represents one subpopulation in the stochastic simulations or one grid point in the deterministic case.

Figure 5.2: Absence of the Hopf bifuraction and related pattern formation at $\mu = 0.050 > \mu_H = 0.042$. The population sizes are $N = (64, 256, 1024)$ increasing from left to right while all other parameters remain the same.

5.1 Absence of Hopf Bifurcation

As argued analytically in Section 2.2.2, the generic metapopulation model exhibits a Hopf bifurcation at the critical value of the mutation rate μ_H (2.24) developing a stable limit cycle with an approximate frequency of ω_H (2.25). For values of $\mu > \mu_H$, the only fixed point (2.23) is globally stable and no patterns are expected to form on the metapopulation lattice. This regime for $\beta = \sigma = 1$ and $\zeta = 0$ is presented in Figure 5.2 where no pattern formation can be observed. The dynamics fluctuates around the stable fixed point due to finite sizes of the subpopulations with the frequencies of all species being approximately equal. As the patch size N is increased, the fluctuations become less pronounced since their amplitude is proportional to the factor of $\frac{1}{\sqrt{N}}$. The entire domain becomes filled with grey coloured subpopulations because of the almost equal quantities of red, green and blue agents as explained in Figure 5.1. These results confirm the global stability of the fixed point for $\mu > \mu_H$ with the amplitude of the stochastic fluctuations around the fixed point originating from the strength of the demographic noise. Time evolutions of the three experiments resulting in the final states shown in Figure 5.2 can be observed in Movie 4 from the supplementary material in Szczesny *et al.* (2012).

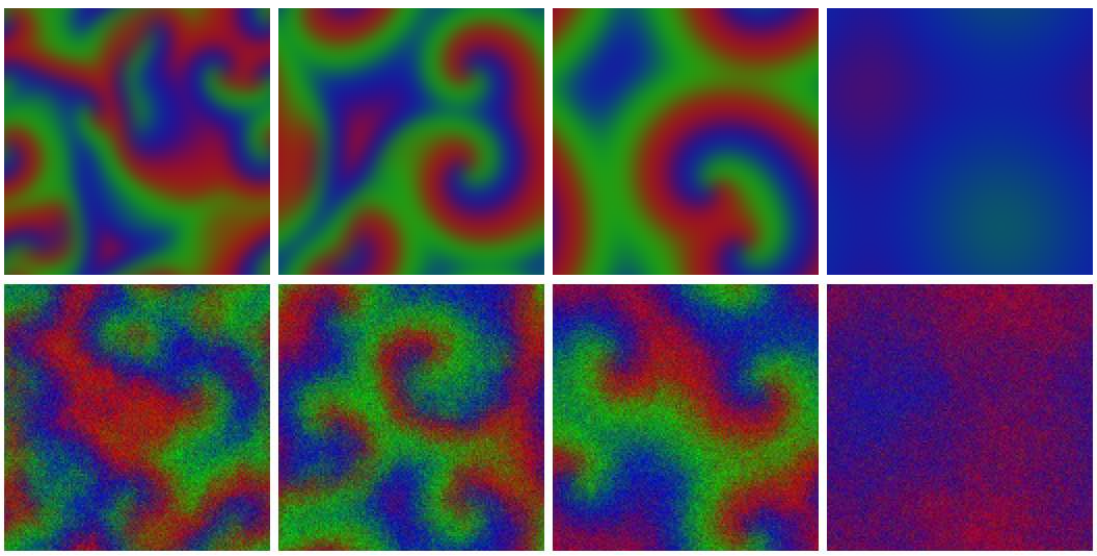

Figure 5.3: Four phases in the PDEs (2.26) (top panel) and the stochastic system (lower panel) for $\zeta = (1.8, 1.2, 0.6, 0)$ from left to right with $\mu = 0.02 < \mu_H = 0.042$. Other parameters are $\beta = \sigma = \delta_D = \delta_E = 1$, $L^2 = G^2 = 128^2$ and $N = 64$. All frames are visualised at time $t = 1000$.

5.2 Four Phases

One of the main results of this research is the classification of the different phases exhibited by the generic metapopulation model. This classification is based on the parameter c from the CGLE (2.69), the phase diagram shown in Figure 4.2 and the four phases observed in the CGLE as discussed in Section 4.1. Even though such predictions are valid only close to the onset of Hopf bifurcation, that is for values of $\epsilon \ll 1$, the mutation rate of $\mu = 0.02$ implying $\epsilon = 0.25$ was used in the simulations. The presence of the phases is confirmed in Figure 5.3 for $\beta = \sigma = 1$ and $\zeta = (1.8, 1.2, 0.6, 0)$ in both stochastic and deterministic simulations. These values β, σ and ζ translate to $c = (1.9, 1.5, 1.0, 0.6)$ respectively placing the system in each of the four different phases. Starting from the rightmost panel, the spiral annihilation (SA) phase is clearly present with the collisions of spirals and eventual relaxation into a homogeneous oscillating state. Further to the left is the phase of bound states (BS) in which stable spiral waves persist forever. The next phase is the Eckhaus instability (EI) phase which does not clearly exhibits

convective instabilities due to the small sizes of the spirals as explained in Section 4.3 for the case of the CGLE. The leftmost panel shows the absolute instability (AI) phase where the distortion of the shape of the patterns is clearly visible. Overall, the patterns presented in Figure 5.3 show striking resemblance to those obtained from the CGLE in Figure 4.3 despite significant departure from the assumptions made during the asymptotic expansion. For the time evolution of the simulations resulting in the final states shown in Figure 5.3 see Movie 1 in Szczesny *et al.* (2012). In addition, the numerical experiments for a low value of carrying capacity $N = 2$ are also recorded as Movie 2 in Szczesny *et al.* (2012). While the noise fluctuations make is difficult to compare the pattern in AI, EI and BS phases, the spiral annihilation is indeed observed in SA phase despite violating the assumptions that $N \gg 1$ required by the system size expansion.

5.2.1 Robustness Testing

The reaction rates stated in the generic model outlined in Section 2.2 are independent of the species indices. Such rates are often considered to ensure the mathematical tractability of the analysis which is greatly simplified for cyclically symmetric equations. However, one can argue analytically that the results of the derivations should be valid in a case of asymmetric rates. Such asymmetry arises in the interactions of the *E. coli* bacteria where the cyclic dominance results from different processes such as reproduction and toxin production in each species (Kerr *et al.*, 2002). The robustness to asymmetry in rates is tested in the simulations by perturbing the rates of the on-site reactions (2.1), (2.2), (2.3) and (2.4) as well as the migration reactions (2.5) and (2.6). More concretely, each of the 39 reaction rates present in the stochastic simulation algorithm was multiplied by a perturbation coefficient drawn from a uniform random distribution in range $[0.95, 1.05]$. Since the EI and AI phases are difficult to compare due their distorted appearance, the robustness testing considered the striking differences between the BS and SA phases. The experiments were repeated several times, starting from different initial conditions, with new perturbing coefficients generated each time. Other parameters were the same as in Section 5.2.

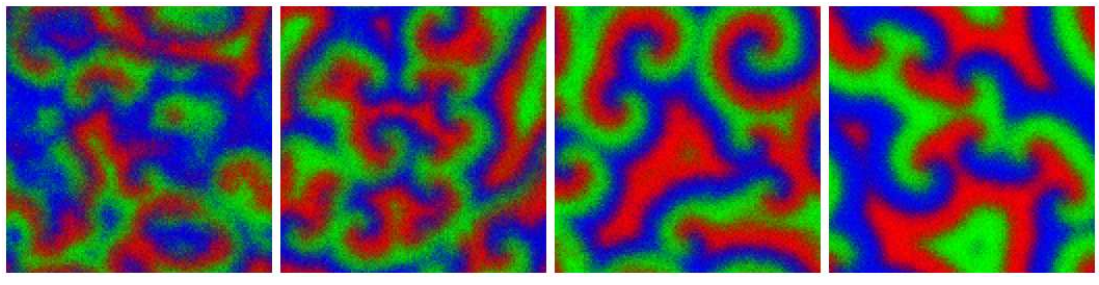

Figure 5.4: Stochastic simulations from Figure 5.3 reproduced far away from the Hopf bifuraction at $\mu = 0.001 \ll \mu_H = 0.042$. All parameters are the same with $\zeta = (1.8, 1.2, 0.6, 0)$ from left to right as before. See Section 5.3 for discussion.

Despite the perturbations, the simulations reproduce the predictions of spiral annihilation at $\zeta = 0$ leading to an oscillating homogeneous state. In the next phase, at $\zeta = 0.6$, persistent bound states were observed after their emergence from the random initial conditions.

5.3 Low Mutation Rates

One of the key assumptions in the multiscale expansion deriving the CGLE (2.69) in Section 2.3.3 is that the perturbation parameter $\epsilon \ll 1$. Despite this assumption, the predictions regarding the appearance of the four phases in the metapopulation model are shown to be valid even for $\mu = 0.02$ implying $\epsilon = 0.25$ via (2.54) as discussed in Section 5.2. Nevertheless, the theory breaks down eventually as shown in Figure 5.4 where a relatively low value of $\mu = 0.001$ was used in stochastic simulations. Comparing the resulting patterns with those obtained with $\mu = 0.02$ shown in Figure 5.3, suggests that the the spiral annihilation phase is no longer present in the right most panel. However, since both experiments were set to run for the same period of time until $t = 1000$, this results can be attributed to the extended annihilation time with spiral collisions happening at later stages of the simulation. The reduction of the wavelength is also noticeable in all phases while the brighter colouring can be attributed to the enlarged limit cycle which increases the amplitude of oscillations in species abundances.

$\downarrow \mu$ (ϵ) $\setminus$ ζ (c) $\rightarrow$	0.2 (0.73)	0.4 (0.86)	0.6 (1.01)	0.8 (1.16)
0.035 (0.14)	(too large)	155	128	111
0.030 (0.19)	130	107	91	80
0.025 (0.22)	99	83	71	63
0.020 (0.25)	77	66	58	52
0.015 (0.28)	61	54	48	(unstable)

Table 5.1: Measurements of spiral arm wavelength λ in solutions to the macroscpic PDEs (2.26) as a function of μ and ζ with corresponding values of ϵ and c. The results are plotted in the domain of CGLE via (5.1) in Figure 5.5.

The decrease of the wavelength for the vanishing mutation rate was investigated in a separate experiment. These findings are important since almost all previous studies of the rock-paper-scissors dynamics set $\mu = 0$ which is shown to be a special case of wavelength convergence. Firstly, the PDEs (2.26) were solved numerically at four different values of ζ in the bound state phase which corresponded to different values of c and wavelengths λ_ϵ in the CGLE space. It is important to understand, that the numerical values of λ_ϵ in Figure 5.5 are obtained by the coordinate transformation outlined in the multiscale expansion in Section 2.3.3. In contrast to mapping technique, the multiscale expansion distinguishes between the spatial coordinate $\mathbf{x}$ in the PDEs and $\mathbf{X}$ in the CGLE. Therefore, the spatial dimension must be matched through the perturbation parameter ϵ based on the coordinate transformation $\mathbf{X} = \epsilon\mathbf{x}$ such that

$$\lambda_\epsilon = \epsilon\lambda = \sqrt{3(\mu_H - \mu)}\lambda. \tag{5.1}$$

Since the critical mutation rate is not a function of ζ (2.24), its value of $\mu_H = 0.042$ for $\beta = \sigma = 1$ is valid in all simulations. A good agreement between the theoretical and experimental values of λ_ϵ are observed close to the onset of Hopf bifurcation. However, as the mutation rate decreases, the wavelengths converge to a single point for all ζ. This discrepancy shows that the predictions about the generic model should be considered as valid only close to the Hopf bifurcation when $\mu \lesssim \mu_H$ rather than when $\mu = 0$ as in the majority of previous studies.

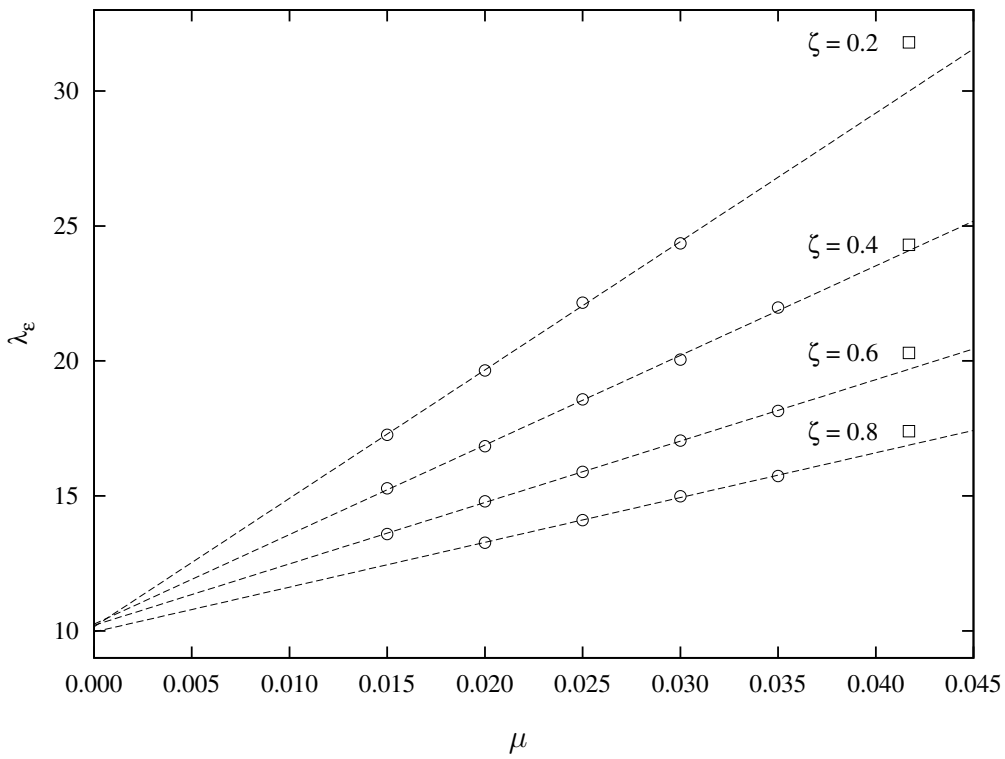

Figure 5.5: The convergence of wavelengths λ_ϵ in the macroscopic PDEs (2.26) as a function of vanishing mutation rate μ. Wavelengths λ obtained from the numerical solutions (circles) are rescaled to λ_ϵ via (5.1) and compared to the predictions from the CGLE (squares) at Hopf bifurcation where $\mu = \mu_H = 0.042$. Raw measurements of the wavelength λ are provided in Table 5.1. Dashed lines represent linear fits through the values of λ_ϵ corresponding to a given value of ζ.

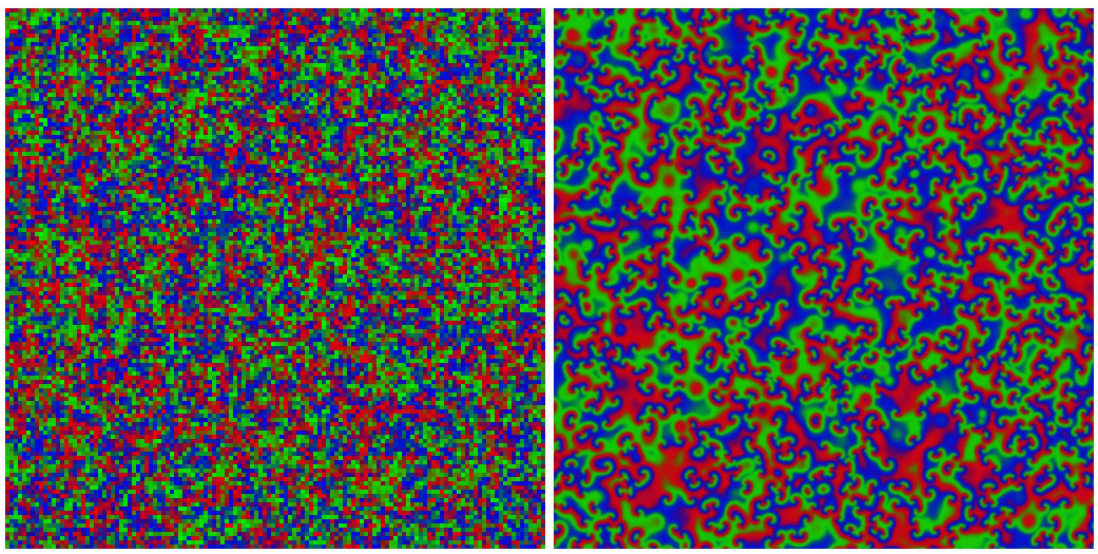

Figure 5.6: Resolution effects in stochastic simulations (left) with equivalent deterministic simulations (right). Domain sizes in both simulations are $L^2 = 128^2$ while the deterministic system has grid size $G^2 = 1024^2$. Other parameters are the same. See Section 5.4 for discussion on the differences in appearance.

5.4 Resolution Effects

The interplay between the diffusion constants δ_D, δ_E and δ, domain size L and grid size G can be a source of confusion when simulating the spatial dynamics of the generic metapopulation model. The relative sizes of δ_D and δ_E are important in the nonlinear mobility case when $\delta_D \neq \delta_E$ as reported in Section 5.5. However, in the case of linear diffusion with $\delta_D = \delta_E$, the constants have no effect on the dynamics except for changing the overall sizes of the patterns. This can be understood by absorbing the constants into the derivatives with $\delta_D \partial_x \to \partial_x$. Such spatial rescaling shows explicitly that diffusion rates δ_D, δ_E and δ from the PDEs (2.26) and the CGLE (2.69) act to zoom out and zoom in on the patterns formed in the domain. One example of such effect is the reported loss of biodiversity for large diffusion rates (Reichenbach *et al.*, 2007a) which results from the patterns outgrowing the domain. It should also be noted that the migration constants δ_D and δ_E from (2.5) and (2.6) are the same quantities as the diffusion constants in the macroscopic PDEs as explained in Section 2.2.2.

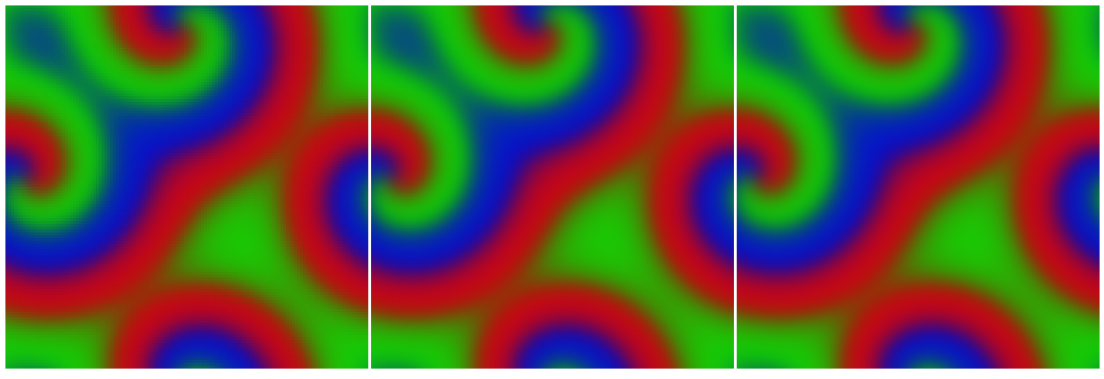

Figure 5.7: Identical outcomes from simulations of the rock-paper-scissors PDEs (2.26) for grid sizes $G^2 = (128^2, 256^2, 512^2)$ from left to right respectively. The domain size is $L^2 = 128^2$ while $\delta_D = \delta_E = 1$.

In stochastic simulations, the domain size and the grid size are coupled quantities such that a lattice of L^2 populations corresponds to a domain with area equal to L^2. Therefore, when integrating the PDEs (2.26), such physical size should be chosen for the domain to obtain solutions matching in space. This also means that certain patterns cannot be represented on the grid of the stochastic system. For example, a plane wave with a wavelength of $\lambda = 0.1$ space units cannot be visualised on a discrete domain with one population representing a minimum distance of 1 space unit. In contrast, the ETD2 integration scheme outlined in Section 3.4 allows for varying the grid size G^2 as an independent variable in the numerical experiments which acts to increase the resolution of the image. Therefore, in the case $G > L$ there can be multiple grid points spanning the distance of 1 space unit in the physical domain. The two different scenarios are shown in Figure 5.6 where the spiral waves, predicted in the continuous system, are absent from the discrete system because of the lack of resolution rather than effects of intrinsic dynamics. In the simulations performed in this research, the diffusion constants used are of order $\mathcal{O}(1)$ which makes the spiral patterns resolvable on the metapopulation grid. Increasing the grid size G in deterministic simulations has no visible effect on the resulting patterns as shown in Figure 5.7. Therefore, the value of $G^2 = 128^2$ is chosen as a default grid size, delivering good resolution and fast performance.

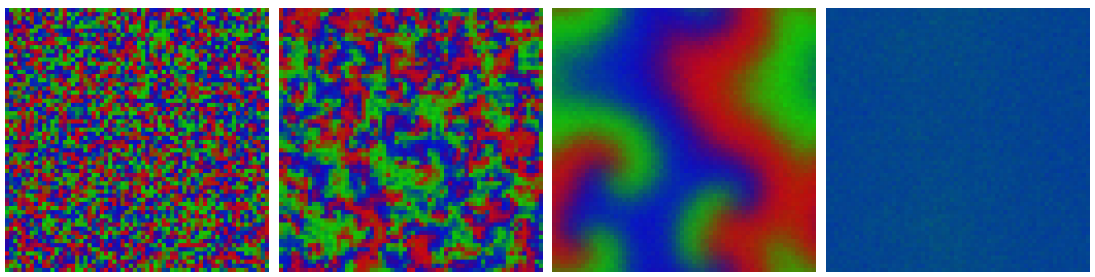

Figure 5.8: An attempt at reproducing results from Rulands *et al.* (2013) reporting effects of diffusion constant on the spiral patterns with $\delta_D = \delta_E = (0.000625, 0.005625, 0.64, 2.56)$ left to right. See Section 5.4 for details.

The problems outlined in this section can lead to claims about the effects of the diffusion constants on the dynamics of the system (Rulands *et al.*, 2013). Namely, critical values of the diffusion constants marking the disappearance of spirals are reported. These claims, in the case of linear diffusion, can be understood and predicted by calculating the wavelength λ of the waves in the spiral arms and comparing them to the resolution of the numerical simulations. For example, the leftmost panel of Figure 5.8 shows results of stochastic simulations for $\lambda = 1$ space unit, while the next panel has $\lambda = 3$ space units. Representing a wave in 1 or even 3 populations is not possible due to the lack of resolution. Therefore, noisy patches rather than spirals are observed. The next two panels to the right show $\lambda = L/2$ and $\lambda = L$ where $L^2 = 64^2$ is the physical domain size. While the case of $\lambda = L/2$ exhibits spirals, the patterns decay into a homogeneous oscillating state as shown in the the rightmost panel of Figure 5.8 where the size of the spiral arms is too large to fit into the domain.

5.5 Far-field Break-up

The effects of the selection-removal process (2.2) on the stability of spiral waves were reported in previous studies in models without mutation with $\mu = 0$. The phenomenon was investigated as a function of the selection-removal rate σ and a critical value of approximately 2 was reported as the onset of Eckhaus instability in Reichenbach & Frey (2008). However, due to the random initial conditions

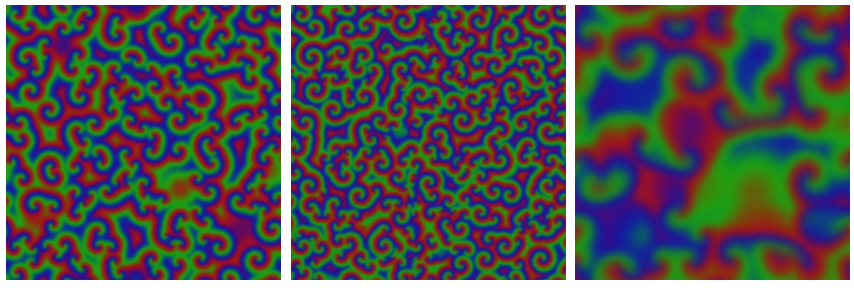

Figure 5.9: Left and centre: BS and EI phases in the PDEs (2.26) with $L^2 = 1024^2$ for $\zeta = (0.6, 1.2)$. Right: AI phase with $L^2 = 256^2$ for $\zeta = 1.8$. Other parameters were $\beta = \sigma = \delta_D = \delta_E = 1$, $\mu = 0.02$ and $G^2 = 256^2$.

and a large number of small spirals present in the domain, it is not clear if the reported simulations at $\sigma = 5$ were not in EI phase. As shown in the left and centre panels of Figure 5.9, the bound state and Eckhaus instability phases are similar in appearance when the starting conditions are random. In contrast, special initial conditions shown in Movie 3 from Szczesny *et al.* (2012) are used in the simulations in order to observe the far-field break-up phenomenon. The conditions are arranged geometrically such that four spirals are seeded in the domain and are then allowed to grow up to a radius equal to a quarter of the domain width L. Moreover, the apparent distortion and blurring of the patterns reported at $\sigma = 0.5$ is most likely caused by the absolute instability rather than Eckhaus instability as can be seen in the rightmost panel of Figure 5.9.

More interestingly, a similar value was estimated as 2.3 ± 0.3 in Jiang *et al.* (2011) for a system with a domain size $L^2 = 512^2$. Different values were also reported for varying domain sizes as would be the case with Eckhaus instability which can be observed only in domains of appropriate size as discussed in Section 4.3. While it is not possible to directly compare the lattice Monte Carlo simulations performed in the previous studies with the lattice Gillespie algorithm simulations, an attempt of reproducing the results is shown in Figure 5.10. The far-field break-up, resembling the Eckhaus instability, can be seen as the value of σ is increased. The wavelength of waves in the spiral arms are also reduced suggesting a critical value of the wavelength, similar to that derived for Eckhaus instability (2.85) in Section 2.3.5.

This hypothesis is tested in simulations which gradually decrease the wavelength of the waves by reducing the values of the diffusion constants δ_D and δ_E as shown in Figure 5.11. It should be noted that despite the value of the subpopulation size $N = 256$, the demographic noise can be responsible for the spiral break-up. The size of carrying capacity N is relevant for low diffusion rates since the resulting thin stripes representing the bacterial concentrations can be easily disrupted by the noise. Nevertheless, the spirals in the leftmost panel of Figure 5.11 with $\delta_D = \delta_E = 0.4$ are stable and a higher value of 0.5 is used as a starting point in simulations presented in Figure 5.12 and discussed below.

As shown in Section 5.4, the effects of diffusion rates in case of linear mobility, when $\delta_D = \delta_E$, have no effects on the stability of spiral waves. However, when $\delta_D \neq \delta_E$, the far-field break-up of spirals resembling the Eckhaus instability can be observed in stochastic simulations. At this point, it should be noted that hopping and exchange mechanisms were investigated previously (He *et al.*, 2011). However, the numerical experiments were performed on single occupancy lattices with $N = 1$ meaning that the influence of demographic noise could be a significant factor in the simulations.

The influence of the nonlinear diffusion rates is reported in Figure 5.12. The leftmost panel of Figure 5.12 shows results for linear mobility only and serves as a control experiment reaffirming that noise effects are not present with $\delta_D = \delta_E = 0.5$ and $N = 256$. The parameters in the next panels remain the same except for δ_D which is increased to the value of 2 in steps of 0.5 from left to right such that $\delta_D > \delta_E$. It should be noted that in the opposite case, when $\delta_D < \delta_E$, the stability of the spirals is not observed after divorcing of the mobility rates. Consequently, the gradual reduction of the maximum radius of the spirals is observed, caused by the break-up of spiral arms. The final check against the influence of noise is performed for the results with $\delta_D = 2$ in the rightmost panel of Figure 5.12 by repeating them with $N = 512$ and $N = 1024$. The increased patch sizes act to further diminish any effects of the demographic noise on the stability of the waves. The results are in agreement with those performed with $N = 256$, showing the far-field break-up of spiral arms caused by the nonlinear mobility. The time evolution of a similar experiment is recorded as Movie 3 in Szczesny *et al.* (2012).

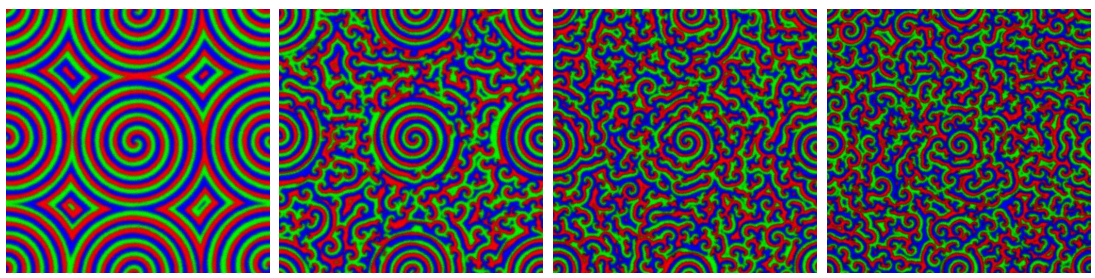

Figure 5.10: Instability of spiral waves with selection-removal rate $\sigma = (1, 2, 3, 4)$ from left to right. The system size is constant in all panels with $N = 64$ and $L^2 = 512^2$. Other parameters are $\delta_D = \delta_E = 0.5$, $\beta = 1$ and $\zeta = \mu = 0$.

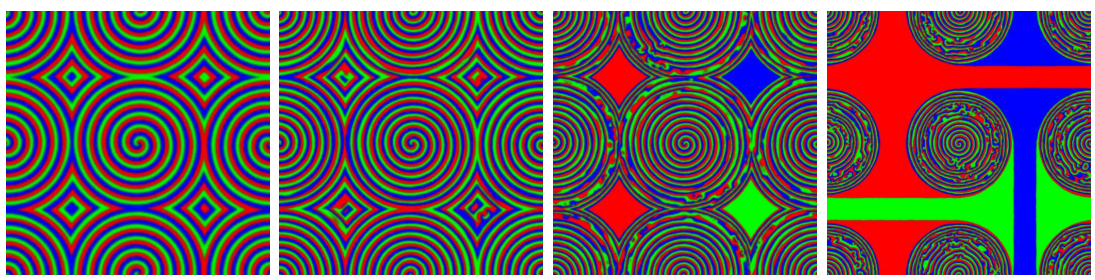

Figure 5.11: Decrease in wavelength and far-field break-up of spiral waves with $\delta_D = \delta_E = (0.4, 0.2, 0.1, 0.05)$ from left to right. The domain size is $L^2 = 512^2$ wtih $N = 256$ in all panels. Other parameters are $\beta = \sigma = 1$ and $\zeta = \mu = 0$. Frames shown at time $t = 800$ with initial conditions still partially visible.

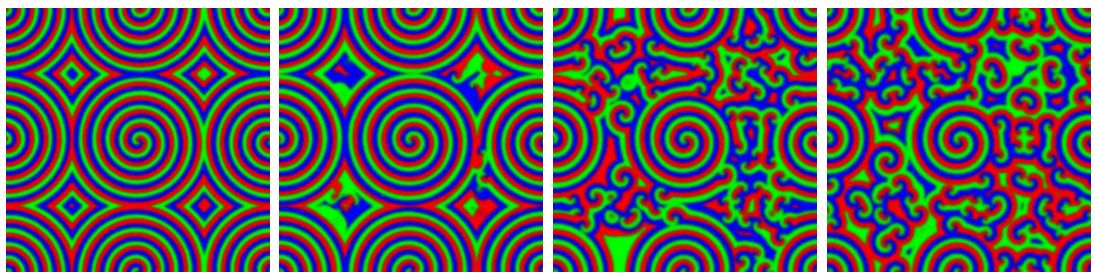

Figure 5.12: Effects of nonlinear mobility on the stability of spiral waves. The diffusion rates are $\delta_D = (0.5, 1, 1.5, 2)$ left to right while $\delta_E = 0.5$ in all panels. Other parameters are $\beta = \sigma = 1$, $\zeta = \mu = 0$ and $L^2 = 512^2$. The demographic noise can be considered negligible with $N = 256$ as shown in Figure 5.13.

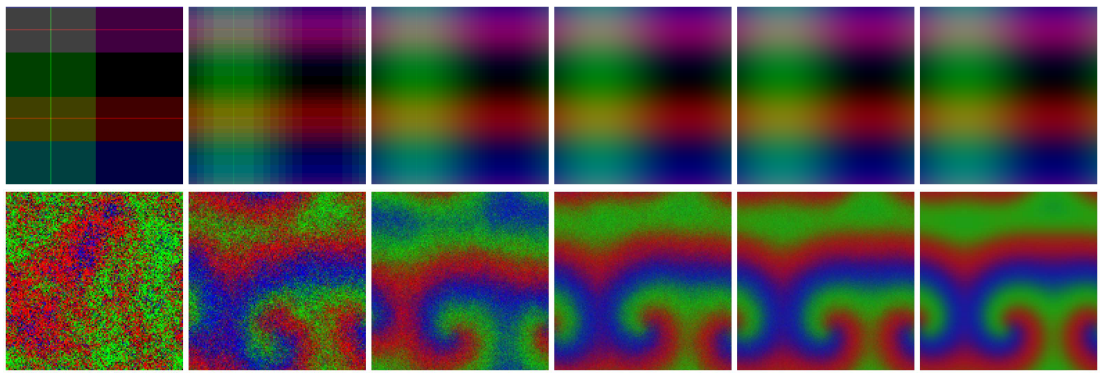

Figure 5.13: Matching stochastic and deterministic simulations for identical parameters. Top panels show initial conditions while lower panels show the domains at time $t = 1000$. The five leftmost panels are the results of stochastic simulations for $L^2 = 128^2$ with $N = 4, 16, 64, 256, 1024$ left to right respectively. The rightmost panels are the solutions of the PDEs (2.26) with grid size $G^2 = 128^2$.

5.6 Matching in Space and Time

As argued in Section 3.2, the lattice Monte Carlo approach is not capable of exact simulations of the Master equation (2.16). However, the lattice Gillespie algorithm described in Section 3.3 is proven to provide statistically exact realisations of the stochastic process. This is an important matter if the long term spatio-temporal properties of the system are to be studied. The agreement between the deterministic dynamics, describing the averages of the simulated quantities, and the stochastic dynamics increases with the population carrying capacity N according to the system size expansion detailed in Section 2.2.2. Therefore, provided that identical initial conditions are used, the evolution of the generic metapopulation model should be indistinguishable for large N when simulated by the deterministic and stochastic algorithms. The results of such numerical experiments are shown in Figure 5.13 while the time evolution is also recorded as Movie 5 in Szczesny *et al.* (2012). As can be seen, the snapshots of the stochastic dynamics match the deterministic results for increasing values of N as predicted by the theory without the need for any arbitrary time or space rescaling.

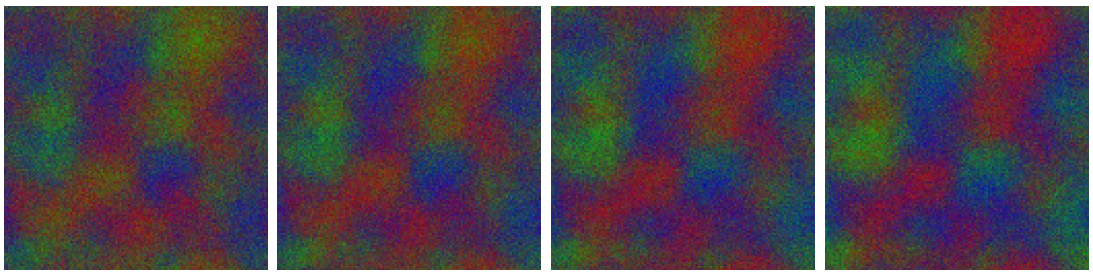

Figure 5.14: Stochastic simulations at time $t = 50, 52, 54, 56$ from left to right. The leftmost panel resembles the starting conditions of the laboratory experiments from Kerr *et al.* (2006). The subsequent time evolution, taking only 6 time units in the simulations, can be compared to 4 days in the experiment with real bacteria reproduced in Figure 5.15.

Certain conclusions about the time scales involved in the numerical and laboratory experiments can also be proposed. The original experiments with *E. coli* bacteria were followed by a number of theoretical studies predicting the appearance of spiral waves. Nevertheless, these patterns are yet to be observed in the real-life bacterial interactions. Most explanations of the missing spirals concentrate on the dynamics of the system discussing various effects impacting on the stability of the spiral waves. However, a different explanation can be proposed, based on matching the time scales reported in the original experiments and those found in the numerical simulations. Starting initially from a random distribution of bacterial species, their self-organisation into small patches can be observed as shown in Figure 5.14. The resulting state is similar to the setup of the real experiments where droplets containing each of the three species of *E. coli* were deposited onto the Petri dish as reproduced in Figure 5.15. The cyclic dominance of the bacteria is then observed from the movement of the boundaries between the patches. This dynamics takes several days in the laboratory while similar motion happens after only few time steps in the computer simulations. Noting that most of theoretically predicted effects appear after hundreds or thousands of such time steps, it is plausible to assume that the real experiments would have to be carried out for months if not years to confirm the analytical predictions.

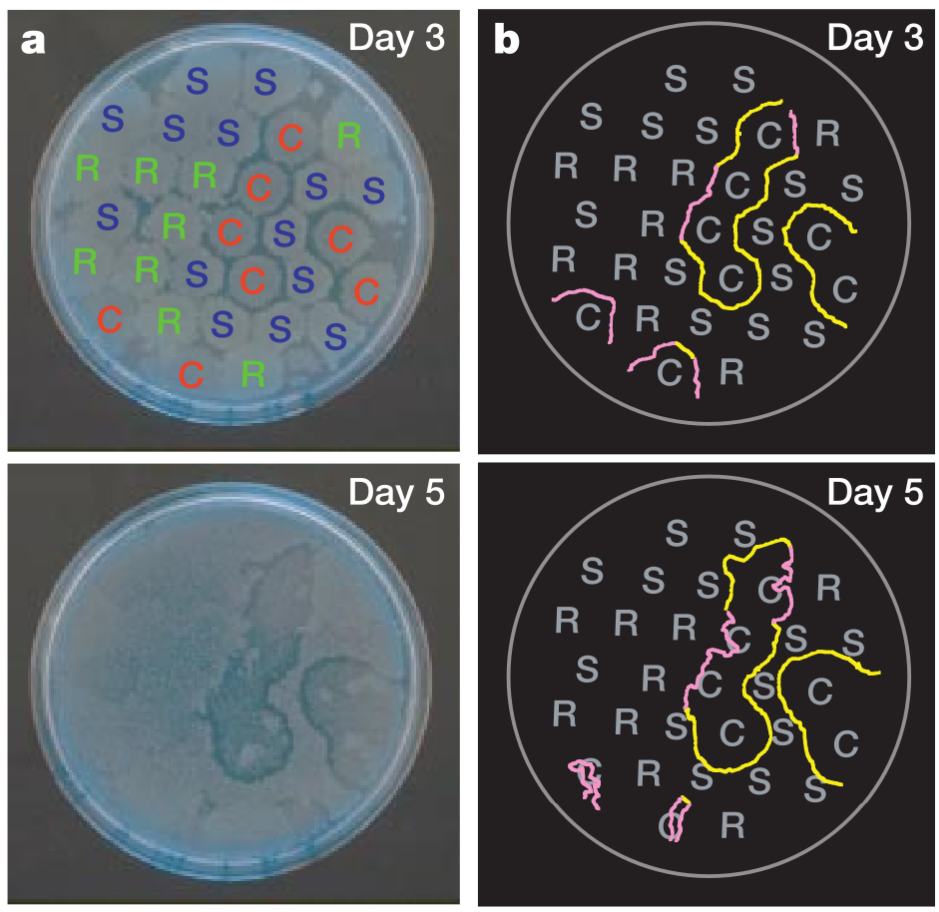

Figure 5.15: Time series photographs of bacterial interactions on a static plate. Letters C, R and S denote communities of colicinogenic (producing), resistant and sensitive strains of *E. coli* bacteria from the diagram in Figure 1.4. Reproduced from Kerr *et al.* (2006), see also Figure 5.14 for a comparison with simulations.

Chapter 6

Conclusion

The postgraduate research presented in this thesis contains a number of innovative approaches which advance or replace the mathematical and computational methods utilised in previous studies as summarised in Section 1.2. These rigorously defined methods, outlined in Chapters 2 and 3, can be generalised to a broad class of population modelling problems where more heuristic approaches are currently in use. As reported in Chapters 4 and 5, the data obtained from the computer simulations agrees with the theoretical predictions in a variety of studies exploring the different aspects of the coevolutionary dynamics.

However, the predictions stated in this thesis should be considered with some caution. As speculated in Section 5.6, the time scales involved in the reported phenomena may not be attainable in laboratory experiments. Moreover, the characterisation of the properties of the spiral waves, such as their velocities and wavelength, are unlikely to be tested in experiments with living organisms. The accurate calculations and measurements of these properties should therefore be considered as a mathematical exercise while their relevance to the physical interactions of the microbial communities should not be overestimated.

Finally, it is worth mentioning that despite inertia originating from a large body of previous research, the more controlled derivation of the CGLE as well as the treatment of previously neglected nonlinear diffusive terms received some recognition in Mowlaei *et al.* (2014) and Claudia & Carletti (2014) while the results are also to appear in a broad review of the field (Szolnoki *et al.*).

Appendix A

Computer Algebra Notebooks

A.1 System Size Expansion

A.1.1 Variables

Mathematical symbols used in Chapter 2 and their corresponding representations in the `REDUCE` notebook deriving the PDEs (2.26) via the system size expansion detailed in Section 2.2:

Symbol	Plaintext
$\sqrt{N}$	`m`
$N_{i,\boldsymbol{\ell}}$	`n(i, l)`
$s_{i,\boldsymbol{\ell}}$	`s(i, l)`
$\eta_{i,\boldsymbol{\ell}}$	`nn(i, l)`
$\Pi(\boldsymbol{\eta}, t)$	`pi`
T_1^β	`re_beta_1`
$\mathbb{E}_{i,\boldsymbol{\ell}}^+ T_1^\beta$	`step_p(re_beta_1, i, l)`
$\Delta_i s_1$	`lap_s1`
$\partial_t s_i$	`ds1_dt`

A.1.2 Comments

The following table contains comments on sections of the source code within specific line numbers. The comments establish direct links to the derivation in Section 2.2.2 and equations therein.

From	To	Comment
1	5	Defining positions for a subpopulation at $\boldsymbol{\ell} = (\ell_1, \ell_2)$ and its neighbours.
7	27	Definition of $N_{i,\boldsymbol{\ell}}$, $s_{i,\boldsymbol{\ell}}$ and $\eta_{i,\boldsymbol{\ell}}$.
29	33	Redefinition of $N_{i,\boldsymbol{\ell}}$ via (2.18).
37	58	Definition of the differential step up/down operators $\mathbb{E}_i^{\pm}$.
62	62	Stating dependence of Π on η_i.
64	98	Reactions T^{β}, T^{σ}, T^{ζ} and T^{μ} and application of the step up/down operators.
101	205	Migration reactions D^{δ_D} and D^{δ_E} and application of the step up/down operators.
209	231	The master equation (2.16).
235	237	The substitutions defining the lattice Laplacian (2.28).
243	245	Extraction of the macroscopic PDEs (2.26).
250	255	Output of the macroscopic PDEs (2.26).
258	262	Checking the simplified output shown in Listing 2.1.

A.1.3 Source

```
let centre = 1; %    2
let above  = 2; %    |
let right  = 3; % 5--1--3
let below  = 4; %    |
let left   = 5; %    4

matrix n(3,5);  % numbers of individuals
matrix s(3,5);  % normalised frequencies
matrix nn(3,5); % fluctuations (noise)

n := mat(
    (n1, n1a, n1r, n1b, n1l),
    (n2, n2a, n2r, n2b, n2l),
    (n3, n3a, n3r, n3b, n3l)
);

s := mat(
    (s1, s1a, s1r, s1b, s1l),
    (s2, s2a, s2r, s2b, s2l),
    (s3, s3a, s3r, s3b, s3l)
);

nn := mat(
    (nn1, nn1a, nn1r, nn1b, nn1l),
    (nn2, nn2a, nn2r, nn2b, nn2l),
    (nn3, nn3a, nn3r, nn3b, nn3l)
);

for sp:=1:3 do <<
    for pos:=1:5 do
        % m = sqrt(N) where N is the carrying capacity
        let n(sp,pos) = ( (m*m)*s(sp,pos) + m*nn(sp,pos) );
>>;

% operators: step up (plus) and step down (minus)

operator step_p;
operator step_m;
operator step_p_m;
operator step_pm_pm;

for all re, sp1p,pos1 let step_p(re, sp1p,pos1) = +df(re, nn(sp1p,pos1)) / m +
    df(re, nn(sp1p,pos1), 2) / m**2 / 2;
for all re, sp1m,pos1 let step_m(re, sp1m,pos1) = -df(re, nn(sp1m,pos1)) / m +
    df(re, nn(sp1m,pos1), 2) / m**2 / 2;

for all re, sp1p,pos1, sp2m,pos2 let step_p_m(re, sp1p,pos1, sp2m,pos2) = (
    (df(re, nn(sp1p,pos1)  ) - df(re, nn(sp2m,pos2)  )) / m
    +
```

```
48      (df(re, nn(sp1p,pos1),2) + df(re, nn(sp2m,pos2),2) - 2*df(df(re,
            nn(sp1p,pos1)), nn(sp2m,pos2))) / m**2 / 2
49  );
50
51  for all re, sp1p,sp1m,pos1, sp2p,sp2m,pos2 let step_pm_pm(re, sp1p,sp1m,pos1,
        sp2p,sp2m,pos2) = (
52      (df(re, nn(sp1p,pos1)  ) - df(re, nn(sp1m,pos1)  ) + df(re, nn(sp2p,pos2)
            ) - df(re, nn(sp2m,pos2)  )) / m
53      +
54      (df(re, nn(sp1p,pos1),2) + df(re, nn(sp1m,pos1),2) + df(re,
            nn(sp2p,pos2),2) + df(re, nn(sp2m,pos2),2)) / m**2 / 2
55      +
56      (-df(df(re,nn(sp1p,pos1)),nn(sp1m,pos1)) +
            df(df(re,nn(sp1p,pos1)),nn(sp2p,pos2)) -
            df(df(re,nn(sp1p,pos1)),nn(sp2m,pos2))
57       -df(df(re,nn(sp1m,pos1)),nn(sp2p,pos2)) +
             df(df(re,nn(sp1m,pos1)),nn(sp2m,pos2)) -
             df(df(re,nn(sp2p,pos2)),nn(sp2m,pos2))) / m**2
58  );
59
60  % transitions
61
62  depend pi, nn1, nn2, nn3;
63
64  re_beta_1 := beta * n(1,centre) * (m*m - n(1,centre) - n(2,centre) -
        n(3,centre)) / m**4;
65  re_beta_2 := beta * n(2,centre) * (m*m - n(1,centre) - n(2,centre) -
        n(3,centre)) / m**4;
66  re_beta_3 := beta * n(3,centre) * (m*m - n(1,centre) - n(2,centre) -
        n(3,centre)) / m**4;
67  re_beta_1 := step_m(re_beta_1*pi, 1,centre) $
68  re_beta_2 := step_m(re_beta_2*pi, 2,centre) $
69  re_beta_3 := step_m(re_beta_3*pi, 3,centre) $
70
71  re_sigma_1 := sigma * n(1,centre) * n(2,centre) / m**4;
72  re_sigma_2 := sigma * n(2,centre) * n(3,centre) / m**4;
73  re_sigma_3 := sigma * n(3,centre) * n(1,centre) / m**4;
74  re_sigma_1 := step_p(re_sigma_1*pi, 2,centre) $
75  re_sigma_2 := step_p(re_sigma_2*pi, 3,centre) $
76  re_sigma_3 := step_p(re_sigma_3*pi, 1,centre) $
77
78  re_zeta_1 := zeta * n(1,centre) * n(2,centre) / m**4;
79  re_zeta_2 := zeta * n(2,centre) * n(3,centre) / m**4;
80  re_zeta_3 := zeta * n(3,centre) * n(1,centre) / m**4;
81  re_zeta_1 := step_p_m(re_zeta_1*pi, 2,centre, 1,centre) $
82  re_zeta_2 := step_p_m(re_zeta_2*pi, 3,centre, 2,centre) $
83  re_zeta_3 := step_p_m(re_zeta_3*pi, 1,centre, 3,centre) $
84
85  re_mu_12 := mu * n(1,centre) / m**2;
86  re_mu_13 := mu * n(1,centre) / m**2;
87  re_mu_12 := step_p_m(re_mu_12*pi, 1,centre, 2,centre) $
```

```
88  re_mu_13 := step_p_m(re_mu_13*pi, 1,centre, 3,centre) $
89
90  re_mu_21 := mu * n(2,centre) / m**2;
91  re_mu_23 := mu * n(2,centre) / m**2;
92  re_mu_21 := step_p_m(re_mu_21*pi, 2,centre, 1,centre) $
93  re_mu_23 := step_p_m(re_mu_23*pi, 2,centre, 3,centre) $
94
95  re_mu_31 := mu * n(3,centre) / m**2;
96  re_mu_32 := mu * n(3,centre) / m**2;
97  re_mu_31 := step_p_m(re_mu_31*pi, 3,centre, 1,centre) $
98  re_mu_32 := step_p_m(re_mu_32*pi, 3,centre, 2,centre) $
99
100
101 re_delta_d_1_ca := delta_d * n(1,centre) * (m*m - n(1,above) - n(2,above) -
        n(3,above)) / m**4;
102 re_delta_d_1_cr := delta_d * n(1,centre) * (m*m - n(1,right) - n(2,right) -
        n(3,right)) / m**4;
103 re_delta_d_1_cb := delta_d * n(1,centre) * (m*m - n(1,below) - n(2,below) -
        n(3,below)) / m**4;
104 re_delta_d_1_cl := delta_d * n(1,centre) * (m*m - n(1,left ) - n(2,left ) -
        n(3,left )) / m**4;
105 re_delta_d_1_ca := step_p_m(re_delta_d_1_ca*pi, 1,centre, 1,above) $
106 re_delta_d_1_cr := step_p_m(re_delta_d_1_cr*pi, 1,centre, 1,right) $
107 re_delta_d_1_cb := step_p_m(re_delta_d_1_cb*pi, 1,centre, 1,below) $
108 re_delta_d_1_cl := step_p_m(re_delta_d_1_cl*pi, 1,centre, 1,left ) $
109
110 re_delta_d_2_ca := delta_d * n(2,centre) * (m*m - n(1,above) - n(2,above) -
        n(3,above)) / m**4;
111 re_delta_d_2_cr := delta_d * n(2,centre) * (m*m - n(1,right) - n(2,right) -
        n(3,right)) / m**4;
112 re_delta_d_2_cb := delta_d * n(2,centre) * (m*m - n(1,below) - n(2,below) -
        n(3,below)) / m**4;
113 re_delta_d_2_cl := delta_d * n(2,centre) * (m*m - n(1,left ) - n(2,left ) -
        n(3,left )) / m**4;
114 re_delta_d_2_ca := step_p_m(re_delta_d_2_ca*pi, 2,centre, 2,above) $
115 re_delta_d_2_cr := step_p_m(re_delta_d_2_cr*pi, 2,centre, 2,right) $
116 re_delta_d_2_cb := step_p_m(re_delta_d_2_cb*pi, 2,centre, 2,below) $
117 re_delta_d_2_cl := step_p_m(re_delta_d_2_cl*pi, 2,centre, 2,left ) $
118
119 re_delta_d_3_ca := delta_d * n(3,centre) * (m*m - n(1,above) - n(2,above) -
        n(3,above)) / m**4;
120 re_delta_d_3_cr := delta_d * n(3,centre) * (m*m - n(1,right) - n(2,right) -
        n(3,right)) / m**4;
121 re_delta_d_3_cb := delta_d * n(3,centre) * (m*m - n(1,below) - n(2,below) -
        n(3,below)) / m**4;
122 re_delta_d_3_cl := delta_d * n(3,centre) * (m*m - n(1,left ) - n(2,left ) -
        n(3,left )) / m**4;
123 re_delta_d_3_ca := step_p_m(re_delta_d_3_ca*pi, 3,centre, 3,above) $
124 re_delta_d_3_cr := step_p_m(re_delta_d_3_cr*pi, 3,centre, 3,right) $
125 re_delta_d_3_cb := step_p_m(re_delta_d_3_cb*pi, 3,centre, 3,below) $
126 re_delta_d_3_cl := step_p_m(re_delta_d_3_cl*pi, 3,centre, 3,left ) $
```

```
127
128 re_delta_d_1_ac := delta_d * n(1,above) * (m*m - n(1,centre) - n(2,centre) -
        n(3,centre)) / m**4;
129 re_delta_d_1_rc := delta_d * n(1,right) * (m*m - n(1,centre) - n(2,centre) -
        n(3,centre)) / m**4;
130 re_delta_d_1_bc := delta_d * n(1,below) * (m*m - n(1,centre) - n(2,centre) -
        n(3,centre)) / m**4;
131 re_delta_d_1_lc := delta_d * n(1,left ) * (m*m - n(1,centre) - n(2,centre) -
        n(3,centre)) / m**4;
132 re_delta_d_1_ac := step_p_m(re_delta_d_1_ac*pi, 1,above, 1,centre) $
133 re_delta_d_1_rc := step_p_m(re_delta_d_1_rc*pi, 1,right, 1,centre) $
134 re_delta_d_1_bc := step_p_m(re_delta_d_1_bc*pi, 1,below, 1,centre) $
135 re_delta_d_1_lc := step_p_m(re_delta_d_1_lc*pi, 1,left , 1,centre) $
136
137 re_delta_d_2_ac := delta_d * n(2,above) * (m*m - n(1,centre) - n(2,centre) -
        n(3,centre)) / m**4;
138 re_delta_d_2_rc := delta_d * n(2,right) * (m*m - n(1,centre) - n(2,centre) -
        n(3,centre)) / m**4;
139 re_delta_d_2_bc := delta_d * n(2,below) * (m*m - n(1,centre) - n(2,centre) -
        n(3,centre)) / m**4;
140 re_delta_d_2_lc := delta_d * n(2,left ) * (m*m - n(1,centre) - n(2,centre) -
        n(3,centre)) / m**4;
141 re_delta_d_2_ac := step_p_m(re_delta_d_2_ac*pi, 2,above, 2,centre) $
142 re_delta_d_2_rc := step_p_m(re_delta_d_2_rc*pi, 2,right, 2,centre) $
143 re_delta_d_2_bc := step_p_m(re_delta_d_2_bc*pi, 2,below, 2,centre) $
144 re_delta_d_2_lc := step_p_m(re_delta_d_2_lc*pi, 2,left , 2,centre) $
145
146 re_delta_d_3_ac := delta_d * n(3,above) * (m*m - n(1,centre) - n(2,centre) -
        n(3,centre)) / m**4;
147 re_delta_d_3_rc := delta_d * n(3,right) * (m*m - n(1,centre) - n(2,centre) -
        n(3,centre)) / m**4;
148 re_delta_d_3_bc := delta_d * n(3,below) * (m*m - n(1,centre) - n(2,centre) -
        n(3,centre)) / m**4;
149 re_delta_d_3_lc := delta_d * n(3,left ) * (m*m - n(1,centre) - n(2,centre) -
        n(3,centre)) / m**4;
150 re_delta_d_3_ac := step_p_m(re_delta_d_3_ac*pi, 3,above, 3,centre) $
151 re_delta_d_3_rc := step_p_m(re_delta_d_3_rc*pi, 3,right, 3,centre) $
152 re_delta_d_3_bc := step_p_m(re_delta_d_3_bc*pi, 3,below, 3,centre) $
153 re_delta_d_3_lc := step_p_m(re_delta_d_3_lc*pi, 3,left , 3,centre) $
154
155
156 re_delta_e_12_ca := delta_e * n(1,centre) * n(2,above) / m**4;
157 re_delta_e_13_ca := delta_e * n(1,centre) * n(3,above) / m**4;
158 re_delta_e_12_cr := delta_e * n(1,centre) * n(2,right) / m**4;
159 re_delta_e_13_cr := delta_e * n(1,centre) * n(3,right) / m**4;
160 re_delta_e_12_cb := delta_e * n(1,centre) * n(2,below) / m**4;
161 re_delta_e_13_cb := delta_e * n(1,centre) * n(3,below) / m**4;
162 re_delta_e_12_cl := delta_e * n(1,centre) * n(2,left ) / m**4;
163 re_delta_e_13_cl := delta_e * n(1,centre) * n(3,left ) / m**4;
164 re_delta_e_12_ca := step_pm_pm(re_delta_e_12_ca*pi, 1,2,centre, 2,1,above) $
165 re_delta_e_13_ca := step_pm_pm(re_delta_e_13_ca*pi, 1,3,centre, 3,1,above) $
```

```
166 re_delta_e_12_cr := step_pm_pm(re_delta_e_12_cr*pi, 1,2,centre, 2,1,right) $
167 re_delta_e_13_cr := step_pm_pm(re_delta_e_13_cr*pi, 1,3,centre, 3,1,right) $
168 re_delta_e_12_cb := step_pm_pm(re_delta_e_12_cb*pi, 1,2,centre, 2,1,below) $
169 re_delta_e_13_cb := step_pm_pm(re_delta_e_13_cb*pi, 1,3,centre, 3,1,below) $
170 re_delta_e_12_cl := step_pm_pm(re_delta_e_12_cl*pi, 1,2,centre, 2,1,left ) $
171 re_delta_e_13_cl := step_pm_pm(re_delta_e_13_cl*pi, 1,3,centre, 3,1,left ) $
172
173 re_delta_e_21_ca := delta_e * n(2,centre) * n(1,above) / m**4;
174 re_delta_e_23_ca := delta_e * n(2,centre) * n(3,above) / m**4;
175 re_delta_e_21_cr := delta_e * n(2,centre) * n(1,right) / m**4;
176 re_delta_e_23_cr := delta_e * n(2,centre) * n(3,right) / m**4;
177 re_delta_e_21_cb := delta_e * n(2,centre) * n(1,below) / m**4;
178 re_delta_e_23_cb := delta_e * n(2,centre) * n(3,below) / m**4;
179 re_delta_e_21_cl := delta_e * n(2,centre) * n(1,left ) / m**4;
180 re_delta_e_23_cl := delta_e * n(2,centre) * n(3,left ) / m**4;
181 re_delta_e_21_ca := step_pm_pm(re_delta_e_21_ca*pi, 2,1,centre, 1,2,above) $
182 re_delta_e_23_ca := step_pm_pm(re_delta_e_23_ca*pi, 2,3,centre, 3,2,above) $
183 re_delta_e_21_cr := step_pm_pm(re_delta_e_21_cr*pi, 2,1,centre, 1,2,right) $
184 re_delta_e_23_cr := step_pm_pm(re_delta_e_23_cr*pi, 2,3,centre, 3,2,right) $
185 re_delta_e_21_cb := step_pm_pm(re_delta_e_21_cb*pi, 2,1,centre, 1,2,below) $
186 re_delta_e_23_cb := step_pm_pm(re_delta_e_23_cb*pi, 2,3,centre, 3,2,below) $
187 re_delta_e_21_cl := step_pm_pm(re_delta_e_21_cl*pi, 2,1,centre, 1,2,left ) $
188 re_delta_e_23_cl := step_pm_pm(re_delta_e_23_cl*pi, 2,3,centre, 3,2,left ) $
189
190 re_delta_e_31_ca := delta_e * n(3,centre) * n(1,above) / m**4;
191 re_delta_e_32_ca := delta_e * n(3,centre) * n(2,above) / m**4;
192 re_delta_e_31_cr := delta_e * n(3,centre) * n(1,right) / m**4;
193 re_delta_e_32_cr := delta_e * n(3,centre) * n(2,right) / m**4;
194 re_delta_e_31_cb := delta_e * n(3,centre) * n(1,below) / m**4;
195 re_delta_e_32_cb := delta_e * n(3,centre) * n(2,below) / m**4;
196 re_delta_e_31_cl := delta_e * n(3,centre) * n(1,left ) / m**4;
197 re_delta_e_32_cl := delta_e * n(3,centre) * n(2,left ) / m**4;
198 re_delta_e_31_ca := step_pm_pm(re_delta_e_31_ca*pi, 3,1,centre, 1,3,above) $
199 re_delta_e_32_ca := step_pm_pm(re_delta_e_32_ca*pi, 3,2,centre, 2,3,above) $
200 re_delta_e_31_cr := step_pm_pm(re_delta_e_31_cr*pi, 3,1,centre, 1,3,right) $
201 re_delta_e_32_cr := step_pm_pm(re_delta_e_32_cr*pi, 3,2,centre, 2,3,right) $
202 re_delta_e_31_cb := step_pm_pm(re_delta_e_31_cb*pi, 3,1,centre, 1,3,below) $
203 re_delta_e_32_cb := step_pm_pm(re_delta_e_32_cb*pi, 3,2,centre, 2,3,below) $
204 re_delta_e_31_cl := step_pm_pm(re_delta_e_31_cl*pi, 3,1,centre, 1,3,left ) $
205 re_delta_e_32_cl := step_pm_pm(re_delta_e_32_cl*pi, 3,2,centre, 2,3,left ) $
206
207 % RHS of the Master equation
208
209 me_rhs := (-1)*m**4*(
210     re_beta_1 + re_beta_2 + re_beta_3 +
211     re_sigma_1 + re_sigma_2 + re_sigma_3 +
212     re_zeta_1 + re_zeta_2 + re_zeta_3 +
213     re_mu_12 + re_mu_13 + re_mu_21 + re_mu_23 + re_mu_31 + re_mu_32
214     +
215     re_delta_d_1_ca + re_delta_d_1_cr + re_delta_d_1_cb + re_delta_d_1_cl +
216     re_delta_d_2_ca + re_delta_d_2_cr + re_delta_d_2_cb + re_delta_d_2_cl +
```

```
    re_delta_d_3_ca + re_delta_d_3_cr + re_delta_d_3_cb + re_delta_d_3_cl
    +
    re_delta_d_1_ac + re_delta_d_1_rc + re_delta_d_1_bc + re_delta_d_1_lc +
    re_delta_d_2_ac + re_delta_d_2_rc + re_delta_d_2_bc + re_delta_d_2_lc +
    re_delta_d_3_ac + re_delta_d_3_rc + re_delta_d_3_bc + re_delta_d_3_lc
    +
    re_delta_e_12_ca + re_delta_e_13_ca + re_delta_e_12_cr + re_delta_e_13_cr +
    re_delta_e_12_cb + re_delta_e_13_cb + re_delta_e_12_cl + re_delta_e_13_cl
    +
    re_delta_e_21_ca + re_delta_e_23_ca + re_delta_e_21_cr + re_delta_e_23_cr +
    re_delta_e_21_cb + re_delta_e_23_cb + re_delta_e_21_cl + re_delta_e_23_cl
    +
    re_delta_e_31_ca + re_delta_e_32_ca + re_delta_e_31_cr + re_delta_e_32_cr +
    re_delta_e_31_cb + re_delta_e_32_cb + re_delta_e_31_cl + re_delta_e_32_cl
) $

% lattice Laplacian

let s1a + s1b + s1l + s1r = lap_s1 + 4*s1;
let s2a + s2b + s2l + s2r = lap_s2 + 4*s2;
let s3a + s3b + s3l + s3r = lap_s3 + 4*s3;

% rate equations

factor beta, sigma, zeta, mu, delta_d, delta_e;

ds1_dt := coeffn(me_rhs, df(pi,nn1), 1) $
ds2_dt := coeffn(me_rhs, df(pi,nn2), 1) $
ds3_dt := coeffn(me_rhs, df(pi,nn3), 1) $

% order m**3 below is really m**(-1) since "me_rhs" was multiplied by m**4
% and since N = m**2, the expressions occur at order 1/sqrt{N} as expected

write "ds1/dt =";
coeffn(ds1_dt, m, 3);
write "ds2/dt =";
coeffn(ds2_dt, m, 3);
write "ds3/dt =";
coeffn(ds3_dt, m, 3);

% check simplified version from the thesis
pde_s1 :=
beta*s1*(1 - s1 - s2 - s3)- sigma*s1*s3 + zeta*s1*(s2 - s3)
+ mu*(s2 + s3 - 2*s1) + delta_d*lap_s1 +
 (delta_d - delta_e) * (s1*(lap_s2 + lap_s3) - (s2 + s3)*lap_s1);
pde_s1_error := coeffn(ds1_dt, m, 3) - pde_s1; % should = 0
```

A.2 Asymptotic Expansion

A.2.1 Variables

Mathematical symbols used in Chapter 2 and their corresponding representations in the `REDUCE` notebook deriving the CGLE (2.69) via the multiscale asymptotic expansion detailed in Section 2.3:

Symbol	Plaintext
s_1	`s1`
s^*	`fp` (fixed point)
$s_1 - s^*$	`sfp1`
$\mathcal{F}_1(\mathbf{s})$	`f1`
$\partial_t s_1 - \mathcal{F}_1(\mathbf{s})$	`d1` (diffusive terms only)
$\partial_t s_1$	`f1 + d1`
u_1	`u1`
$U_1^{(1)}, U_1^{(2)}, \ldots$	`uu11, uu12, ...`
$\mathcal{Z}^{(1)}, \mathcal{Z}^{*(1)}$	`zz1,zzc1`
$\mathcal{A}^{(1)}, \mathcal{A}^{*(1)}$	`aa1, aac1`
x, X	`x0`, `x1` (since $X = \epsilon^1 x$)
t, T	`t0`, `t2` (since $T = \epsilon^2 t$)

A.2.2 Comments

The following table contains comments on sections of the source code within specific line numbers. The comments establish direct links to the derivation in Section 2.3.3 and equations therein.

From	To	Comment
1	23	Defining variables ϵ, β, σ, ζ, μ, and ω_H as real numbers.
29	38	Definition of the PDEs (2.26).
44	53	Transformation $\mathbf{s} \to \mathbf{s} - s^*$.
55	59	Jacobian of the PDEs (2.26).
61	78	Eigenvalues and eigenvectors of the Jacobian.
80	97	Matrix for transformation to the Jordan normal form.
99	113	Transformation to the Jordan normal form.
115	128	Dependence of $\mathbf{U}^{(n)}$ on t, T and $\mathbf{X}$.
132	149	Multiscale expansion of coordinates x and t via (2.55).
151	153	Multiscale expansion of variable $\mathbf{u}$ via (2.58).
155	161	Hierarchy of simplified PDEs at different orders of ϵ.
165	179	Dependence of $\mathcal{Z}$ on t, T and $\mathbf{X}$ and $\mathcal{A}$ on T and $\mathbf{X}$.
181	212	Moving to a complex plane via (2.59).
217	230	Solving at order $\mathcal{O}(\epsilon)$.
232	253	Solving at order $\mathcal{O}(\epsilon^2)$.
255	260	Solving at order $\mathcal{O}(\epsilon^3)$.
262	266	Checking the expression for `c1` from line 241.
268	273	Calculation of c in the CGLE (2.69).
277	279	Checking the simplified expression for c (2.70).

A.2.3 Source

```
let repart(epsilon) = epsilon;
let impart(epsilon) = 0;
let    abs(epsilon) = epsilon;

let repart(sigma) = sigma;
let impart(sigma) = 0;
let    abs(sigma) = sigma;

let repart(beta) = beta;
let impart(beta) = 0;
let    abs(beta) = beta;

let repart(zeta) = zeta;
let impart(zeta) = 0;
let    abs(zeta) = zeta;

let repart(mu) = mu;
let impart(mu) = 0;
let    abs(mu) = mu;

let repart(omega_hopf) = omega_hopf;
let impart(omega_hopf) = 0;
let    abs(omega_hopf) = omega_hopf;

depend s1, x0 $
depend s2, x0 $
depend s3, x0 $

f1 := beta*s1*(1-s1-s2-s3) - sigma*s3*s1 - zeta*s3*s1 + zeta*s1*s2 + mu*(s2 +
    s3 - 2*s1) $
f2 := beta*s2*(1-s1-s2-s3) - sigma*s1*s2 - zeta*s1*s2 + zeta*s2*s3 + mu*(s3 +
    s1 - 2*s2) $
f3 := beta*s3*(1-s1-s2-s3) - sigma*s2*s3 - zeta*s2*s3 + zeta*s3*s1 + mu*(s1 +
    s2 - 2*s3) $

d1 := delta_d*df(s1, x0,2) + (delta_e - delta_d)*((s2 + s3)*df(s1, x0,2) -
    s1*df(s2 + s3, x0,2)) $
d2 := delta_d*df(s2, x0,2) + (delta_e - delta_d)*((s3 + s1)*df(s2, x0,2) -
    s2*df(s3 + s1, x0,2)) $
d3 := delta_d*df(s3, x0,2) + (delta_e - delta_d)*((s1 + s2)*df(s3, x0,2) -
    s3*df(s1 + s2, x0,2)) $

f := tp mat((f1, f2, f3))$
d := tp mat((d1, d2, d3))$

depend sfp1, x0 $
depend sfp2, x0 $
depend sfp3, x0 $

```

```
sfp := tp mat((sfp1,sfp2,sfp3))$
fp := beta / (3*beta + sigma);
for n:=1:3 do
    write "fixed point check: 0 == ", sub({s1=fp, s2=fp, s3=fp}, f(n,1));

sub_fp := {s1=sfp1+fp, s2=sfp2+fp, s3=sfp3+fp} $
new_fp := {sfp1=0, sfp2=0, sfp3=0} $

f := sub(sub_fp, f) $
d := sub(sub_fp, d) $

matrix jac(3,3);
for n:=1:3 do
    for m:=1:3 do
        jac(n,m) := df(f(n,1), sfp(m,1));
jac := sub(new_fp, jac) $

on fullroots$
eigSol := mateigen(jac, ev) $

charpoly1 := part(eigSol, 1,1) $
charpoly2 := part(eigSol, 2,1) $

eSol1 := solve(charpoly1=0, ev) $
eSol2 := solve(charpoly2=0, ev) $

let abs(sigma + 3*beta) = sigma + 3*beta;
let abs(sigma + 2*zeta) = sigma + 2*zeta;

eVal1 := sub(part(eSol2,1), ev) $
eVal2 := sub(part(eSol2,2), ev) $
eVal3 := sub(     eSol1,    ev) $
eVec1 := sub({arbcomplex(2)=1, ev=eVal1}, part(eigSol, 2,3)) $
eVec2 := sub({arbcomplex(2)=1, ev=eVal2}, part(eigSol, 2,3)) $
eVec3 := sub({arbcomplex(1)=1, ev=eVal3}, part(eigSol, 1,3)) $

for k:=1:3 do <<
    eVec1(k,1) := repart(eVec1(k,1));
    eVec2(k,1) := impart(eVec2(k,1));
>>;

norm1 := tp(eVec1)*eVec1 $
norm2 := tp(eVec2)*eVec2 $
norm3 := tp(eVec3)*eVec3 $
norma := tp mat((sqrt(norm1(1,1)), sqrt(norm2(1,1)), sqrt(norm3(1,1)))) $

matrix sep(3,3) $
for k:=1:3 do <<
    sep(1,k) := eVec1(k,1) / norma(1,1) $
    sep(2,k) := eVec2(k,1) / norma(2,1) $
    sep(3,k) := eVec3(k,1) / norma(3,1) $
```

```
>>;
sep := sep; % to display
transpose_sep_times_sep := tp(sep) * sep; % should = identity matrix

depend u1, x0,x1, t0,t1 $
depend u2, x0,x1, t0,t1 $
depend u3, x0,x1, t0,t1 $

u := tp mat((u1, u2, u3)) $
sfp_to_u_mat := 1/sep * u $
sfp_to_u_sub := {sfp1=sfp_to_u_mat(1,1), sfp2=sfp_to_u_mat(2,1),
    sfp3=sfp_to_u_mat(3,1)} $

mu_hopf := beta*sigma / 6 / (sigma + 3*beta);
let mu = mu_hopf - epsilon**2 / 3;
let zeta = omega_hopf * (sigma + 3*beta) / sqrt(3) / beta - sigma / 2;

jack := sep * jac / sep;
f := sep * sub(sfp_to_u_sub, f) $
d := sep * sub(sfp_to_u_sub, d) $

depend uu11, x1, t0,t2 $
depend uu12, x1, t0,t2 $
depend uu13, x1, t0,t2 $
depend uu14, x1, t0,t2 $

depend uu21, x1, t0,t2 $
depend uu22, x1, t0,t2 $
depend uu23, x1, t0,t2 $
depend uu24, x1, t0,t2 $

depend uu31, x1, t0,t2 $
depend uu32, x1, t0,t2 $
depend uu33, x1, t0,t2 $
depend uu34, x1, t0,t2 $

let epsilon**5 = 0 $

dx_sub := {
    df(u1, x0,2) = epsilon**0 * (  df(u1, x0,x0))
                 + epsilon**1 * (2*df(u1, x0,x1))
                 + epsilon**2 * (  df(u1, x1,x1)),
    df(u2, x0,2) = epsilon**0 * (  df(u2, x0,x0))
                 + epsilon**1 * (2*df(u2, x0,x1))
                 + epsilon**2 * (  df(u2, x1,x1)),
    df(u3, x0,2) = epsilon**0 * (  df(u3, x0,x0))
                 + epsilon**1 * (2*df(u3, x0,x1))
                 + epsilon**2 * (  df(u3, x1,x1))
} $
d := sub(dx_sub, d) $

```

```
dt := tp mat ((
    df(u1, t0) + epsilon**2 * df(u1, t2),
    df(u2, t0) + epsilon**2 * df(u2, t2),
    df(u3, t0) + epsilon**2 * df(u3, t2)
)) $

let u1 = epsilon * uu11 + epsilon**2 * uu12 + epsilon**3 * uu13 + epsilon**4 *
    uu14 $
let u2 = epsilon * uu21 + epsilon**2 * uu22 + epsilon**3 * uu23 + epsilon**4 *
    uu24 $
let u3 = epsilon * uu31 + epsilon**2 * uu32 + epsilon**3 * uu33 + epsilon**4 *
    uu34 $

fd1_eps := coeff(f(1,1) + d(1,1), epsilon) $
fd2_eps := coeff(f(2,1) + d(2,1), epsilon) $
fd3_eps := coeff(f(3,1) + d(3,1), epsilon) $

dt1_eps := coeff(dt(1,1), epsilon) $
dt2_eps := coeff(dt(2,1), epsilon) $
dt3_eps := coeff(dt(3,1), epsilon) $

on complex $

depend zz1, x1, t0,t2 $
depend zz2, x1, t0,t2 $
depend zz3, x1, t0,t2 $
depend zz4, x1, t0,t2 $

depend zzc1, x1, t0,t2 $
depend zzc2, x1, t0,t2 $
depend zzc3, x1, t0,t2 $
depend zzc4, x1, t0,t2 $

depend aa1, x1, t2 $
depend aa2, x1, t2 $

depend aac1, x1, t2 $
depend aac2, x1, t2 $

matrix t_eps(5,1) $
matrix z_eps(5,1) $
matrix w_eps(5,1) $

for k:=1:4 do
<<
    t_eps(k,1) := part(dt1_eps,k) + i * part(dt2_eps,k) $
    z_eps(k,1) := part(fd1_eps,k) + i * part(fd2_eps,k) $
    w_eps(k,1) := part(fd3_eps,k) $
>>;

on div $
```

```
193
194 factor zz1, zz2, zz3, zz4;
195 factor zzc1, zzc2, zzc3, zzc4;
196 factor uu31, uu32, uu33, uu34;
197
198 factor df(zz1, x1,2), df(zz2, x1,2), df(zz3, x1,2), df(zz4, x1,2);
199 factor df(uu32, x1,2);
200
201 factor aa1, aac1;
202 factor exp(i*omega_hopf*t0);
203
204 let uu11 = (zz1 + zzc1) /  2    $
205 let uu12 = (zz2 + zzc2) /  2    $
206 let uu13 = (zz3 + zzc3) /  2    $
207 let uu14 = (zz4 + zzc4) /  2    $
208
209 let uu21 = (zz1 - zzc1) / (2*i) $
210 let uu22 = (zz2 - zzc2) / (2*i) $
211 let uu23 = (zz3 - zzc3) / (2*i) $
212 let uu24 = (zz4 - zzc4) / (2*i) $
213
214 % introduce delta = (3*beta*delta_e + sigma*delta_d) / (sigma + 3*beta)
215 let delta_e = (delta*(sigma + 3*beta) - sigma*delta_d) / 3 / beta $
216
217 write "### order O(epsilon**1):";
218 write         t_eps(2,1), " = ", z_eps(2,1);
219 write part(dt3_eps, 2),   " = ", w_eps(2,1);
220
221 zz1sol  := aa1*exp( i*omega_hopf*t0);
222 zzc1sol := aac1*exp(-i*omega_hopf*t0);
223 uu31sol := 0 $
224
225 write "### O(epsilon**1) solution check: 0 == ", sub({zz1 = zz1sol}, t_eps(2,1)
        - z_eps(2,1));
226 write "### O(epsilon**1) solution check: 0 == ", sub({uu31 = uu31sol},
        part(dt3_eps, 2) - w_eps(2,1));
227
228 let uu31 = uu31sol $
229 let df(zz1,x0) = 0 $
230 let df(zzc1,x0) = 0 $
231
232 write "### order O(epsilon**2):";
233 write  t_eps(3,1),      " = ", z_eps(3,1);
234 write  part(dt3_eps,3), " = ", w_eps(3,1);
235
236 zz2sol  := aa2  * exp(+i*omega_hopf*t0) + (+i*     c1 ) / (3*omega_hopf) *
        (zzc1sol**2);
237 zzc2sol := aac2 * exp(-i*omega_hopf*t0) + (-i*conj(c1)) / (3*omega_hopf) *
        (zz1sol**2);
238 uu32sol := m1 * zzc1*zz1 / beta;
239
```

```
240 m1 :=  sigma / 2 / sqrt(3);
241 c1 := (sigma / 2 - i*omega_hopf*(sigma/beta + 3)) / sqrt(6); % = coefficient of
        zzc1**2
242
243 write "### O(epsilon**2) solution check: 0 == ",
244       sub({zz1=zz1sol, zzc1=zzc1sol}, sub({zz2=zz2sol}, t_eps(3,1) -
              z_eps(3,1))),
245       "  <- secularity condition!";
246 write "### O(epsilon**2) solution check: 0 == ",
247       sub({zz1=zz1sol, zzc1=zzc1sol}, sub({uu32=uu32sol}, part(dt3_eps, 3) -
              w_eps(3,1)));
248
249 let df(uu32, x0) = 0 $
250 let df(uu32, t0) = 0 $
251
252 let df(zz2,  x0) = 0 $
253 let df(zzc2, x0) = 0 $
254
255 write "### order O(epsilon**3):";
256 write t_eps(4,1),       " = ", z_eps(4,1);
257 write part(dt3_eps, 4), " = ", w_eps(4,1);
258
259 write "### (CGLE should be here)*exp(*i*omega_hopf*t0) :";
260 third_order := sub({zz1=zz1sol, zzc1=zzc1sol}, sub({zz2=zz2sol, zzc2=zzc2sol,
        uu32=uu32sol}, t_eps(4,1) - z_eps(4,1)));
261
262 check_c1_zzc1zzc2 := coeffn(coeffn(z_eps(4,1), zzc1,1), zzc2,1) - 2*c1;
263 check_c1_zz1uu32 := coeffn(coeffn(z_eps(4,1), zz1,1), uu32,1) - (-sqrt(2)*c1 -
        sqrt(3)*beta);
264
265 cgl_c := 2*i*conj(c1)*c1 / 3 / omega_hopf + (sqrt(2)*c1 + sqrt(3)*beta)*m1 /
        beta;
266 check_c1_aac1aa1aa1 := coeffn(coeffn(third_order, aa1, 2), aac1,
        1)/exp(i*omega_hopf*t0) - cgl_c;
267
268 cgl_c_re := repart(cgl_c);
269 cgl_c_im := impart(cgl_c);
270
271 clear zeta; % avoid cyclic substitution: zeta -> omega_hopf -> zeta -> ...
272 omega_hopf := sqrt(3)*beta*(sigma + 2*zeta) / 2 / (3*beta + sigma);
273 cgl_c := cgl_c_im / cgl_c_re;
274
275 off exp;
276
277 cgl_c_nice_num := 12*zeta*(6*beta - sigma)*(sigma + zeta) + sigma**2*(24*beta -
        sigma);
278 cgl_c_nice_den := 3*sqrt(3) * sigma * (6*beta + sigma) * (sigma + 2*zeta);
279 cgl_c_nice_err := cgl_c_nice_num / cgl_c_nice_den - cgl_c; % should = 0
```

A.3 Eckhaus Criterion

A.3.1 Variables

Mathematical symbols used in Chapter 2 and their corresponding representations in the `REDUCE` notebook deriving the Eckhaus criterion (2.83) via the perturbed plane wave Ansatz (2.77) detailed in Section 2.3.5, see also Table A.2.1:

Symbol	Plaintext
$\mathcal{A}$	`aa`
$\mathcal{R}$	`rr`
ϵ'	`epsilonp`
$\hat{\rho}, \hat{\varphi}$	`rho_hat, phi_hat`

A.3.2 Comments

The following table contains comments on sections of the source code within specific line numbers. The comments establish direct links to the derivation in Section 2.3.5 and equations therein.

From	To	Comment
1	5	Defining operators for exponentials of complex numbers.
7	35	Defining variables as real.
39	49	Applying unperturbed plane wave Ansatz (2.71).
76	90	Applying the perturbed Ansatz (2.77).
92	97	Definition of perturbations (2.78) and (2.79).
101	106	Deriving the eigenvalue problem (2.81).
108	120	Solving the eigenvalue problem (2.81).
122	128	Taylor expansion of the growth rate g (2.82).

A.3.3 Source

```
operator expi;
let expi(0) = 1;
for all arg1,arg2 let expi(arg1)*expi(arg2) = expi(arg1 + arg2);
for all arg,amp   let conj(amp*expi(arg)) = conj(amp)*expi(-arg);
for all arg,dfv   let df(expi(arg), dfv) = i*df(arg, dfv)*expi(arg);

let repart(rr) = rr;
let impart(rr) = 0;

let repart(c) = c;
let impart(c) = 0;

let repart(delta) = delta;
let impart(delta) = 0;

let repart(q) = q;
let impart(q) = 0;

let repart(k) = k;
let impart(k) = 0;

let repart(omega) = omega;
let impart(omega) = 0;

let repart(rho) = rho;
let impart(rho) = 0;

let repart(phi) = phi;
let impart(phi) = 0;

let repart(x0) = x0;
let impart(x0) = 0;

let repart(t0) = t0;
let impart(t0) = 0;

off exp;

aa := rr*expi(q*x0 + omega*t0) $
cgle := delta*df(aa, x0,x0) + aa - (1 + i*c)*aa*conj(aa)*aa - df(aa, t0) $
cgle_div := cgle / aa $

cgle_div_re := repart(cgle_div) $
cgle_div_im := impart(cgle_div) $

rr_sol := solve(cgle_div_re=0, rr) $
rr_sol := sub(part(rr_sol, 1), rr);
omega_sol := sub(solve(cgle_div_im=0, omega), omega) $
omega_sol := sub({rr=rr_sol},omega_sol);
```

```
50
51  depend phi, x0, t0;
52  depend rho, x0, t0;
53
54  let repart(df(rho, t0)) = df(rho, t0);
55  let impart(df(rho, t0)) = 0;
56
57  let repart(df(rho, x0)) = df(rho, x0);
58  let impart(df(rho, x0)) = 0;
59
60  let repart(df(rho, x0,x0)) = df(rho, x0,x0);
61  let impart(df(rho, x0,x0)) = 0;
62
63  let repart(df(phi, t0)) = df(phi, t0);
64  let impart(df(phi, t0)) = 0;
65
66  let repart(df(phi, x0)) = df(phi, x0);
67  let impart(df(phi, x0)) = 0;
68
69  let repart(df(phi, x0,x0)) = df(phi, x0,x0);
70  let impart(df(phi, x0,x0)) = 0;
71
72  let repart(epsilonp) = epsilonp;
73  let impart(epsilonp) = 0;
74  let epsilonp**2 = 0;
75
76  aa := rr*(1 + epsilonp*rho)*expi(q*x0 + omega*t0 + epsilonp*phi) $
77  cgle := delta*df(aa, x0,x0) + aa - (1 + i*c)*aa*conj(aa)*aa - df(aa, t0) $
78  cgle_div := cgle / rr / expi(q*x0 + omega*t0 + epsilonp*phi) $
79
80  cgle_div_re := repart(cgle_div) $
81  cgle_div_im := impart(cgle_div) $
82
83  let q**2 = (1 - rr**2) / delta;
84  rr_omega_wave := {omega=omega_sol} $
85
86  cgle_div_re := sub(rr_omega_wave, repart(cgle_div)) $
87  cgle_div_im := sub(rr_omega_wave, impart(cgle_div)) $
88
89  df_rho_sub := sub(solve(cgle_div_re=0, df(rho, t0)), df(rho, t0)) $
90  df_phi_sub := sub(solve(cgle_div_im=0, df(phi, t0)), df(phi, t0)) $
91
92  rho_phi_wave := {
93      phi = phi_hat*exp(g*t0)*expi(k*x0),
94      rho = rho_hat*exp(g*t0)*expi(k*x0)
95  } $
96  df_rho_sub := sub(rho_phi_wave, df_rho_sub) / exp(g*t0) / expi(k*x0) $
97  df_phi_sub := sub(rho_phi_wave, df_phi_sub) / exp(g*t0) / expi(k*x0) $
98
99  on exp; % needed by coeff()
100
```

```
matrix rho_phi_mat(2,2);
rho_phi_mat(1,1) := coeffn(df_rho_sub, rho_hat, 1) $
rho_phi_mat(1,2) := coeffn(df_rho_sub, phi_hat, 1) $
rho_phi_mat(2,1) := coeffn(df_phi_sub, rho_hat, 1) $
rho_phi_mat(2,2) := coeffn(df_phi_sub, phi_hat, 1) $
write "rho_phi_mat := ", rho_phi_mat;

eig_sol := mateigen(rho_phi_mat, g) $

charpoly := part(eig_sol, 1, 1) $
charpoly_check := (rho_phi_mat(1, 1) - g)*(rho_phi_mat(2, 2) - g)
                - (rho_phi_mat(1, 2)    )*(rho_phi_mat(2, 1)    ) $
charpoly_err := charpoly_check - charpoly;

eig_val1 := sub(part(solve(charpoly=0, g), 1), g) $
eig_val2 := sub(part(solve(charpoly=0, g), 2), g) $

eig_vec := part(eig_sol, 1, 3) $
eig_vec1 := sub({g=eig_val1, arbcomplex(1)=1}, eig_vec) $
eig_vec2 := sub({g=eig_val2, arbcomplex(1)=1}, eig_vec) $

load_package "taylor";

eig_vec1 := taylor(eig_vec1, k, 0, 1);
eig_vec2 := taylor(eig_vec2, k, 0, 1);

eig_val1 := taylor(eig_val1, k, 0, 2);
eig_val2 := taylor(eig_val2, k, 0, 2);
```

A.4 Fixed Point Shift

```
% lin : linear    terms
% nlt : nonlinear terms

depend s1,  x $
depend s2,  x $
depend s3,  x $
depend ss1, x $
depend ss2, x $
depend ss3, x $

factor s1,  s2,  s3  $
factor ss1, ss2, ss3 $
factor df(s1, x,2), df(s2, x,2), df(s3, x,2) $
factor df(ss1,x,2), df(ss2,x,2), df(ss3,x,2) $

f1 := beta*s1*(1 - s1 - s2 - s3) - sigma*s1*s3 + zeta*(s1*s2 - s1*s3)
   + mu*(s2 + s3 - 2*s1) $
d1 := delta_d*df(s1,x,2)
   + (delta_d - delta_e) * (s1*df(s2 + s3,x,2) - (s2 + s3)*df(s1,x,2)) $

let s1 = ss1 + fp $
let s2 = ss2 + fp $
let s3 = ss3 + fp $

d1_lin := coeffn(d1, df(ss1,x,2), 1) $
d1_lin := coeffn(d1_lin, ss2, 0) $
d1_lin := coeffn(d1_lin, ss3, 0);
d1_nlt := d1 - d1_lin * df(ss1,x,2);

f1_lin := coeffn(f1, ss1, 1) $
f1_lin := coeffn(f1_lin, ss2, 0) $
f1_lin := coeffn(f1_lin, ss3, 0);
f1_lin_simplified := (1 - 4*fp)*beta - fp*sigma - 2*mu $

f1_nlt := f1 - f1_lin*ss1;
f1_nlt_simplified := fp*(beta - fp*(3*beta + sigma))
                   + (mu - fp*(beta         - zeta)) * ss2
                   + (mu - fp*(beta + sigma + zeta)) * ss3
                   - (beta                ) * ss1 * ss1
                   - (beta          - zeta) * ss1 * ss2
                   - (beta + sigma + zeta) * ss1 * ss3 $

% checks, all err's should = 0
err1 := f1 - f1_lin*ss1 - f1_nlt;
err2 := f1_lin - f1_lin_simplified;
err3 := f1_nlt - f1_nlt_simplified;
```

References

Anderson, D.F. (2007). A modified next reaction method for simulating chemical systems with time dependent propensities and delays. *J. Chem. Phys.*, **127**, 214107. 39

Antal, T. & Droz, M. (2001). Phase transitions and oscillations in a lattice prey-predator model. *Phys. Rev. E*, **63**, 056119. 38

Aranson, I.S. & Kramer, L. (2002). The world of the complex Ginzburg–Landau equation. *Rev. Mod. Phys.*, **74**, 99–143. 51

Aranson, I.S., Aranson, L., Kramer, L. & Weber, A. (1992). Stability limits of spirals and traveling waves in nonequilibrium media. *Phys. Rev. A*, **46**, R2992–R2995. 30, 35

Aranson, I.S., Kramer, L. & Weber, A. (1993). Theory of interaction and bound states of spiral waves in oscillatory media. *Phys. Rev. E*, **47**, 3231–3241. 30, 52, 62

Bär, M. & Brusch, L. (2004). Breakup of spiral waves caused by radial dynamics: Eckhaus and finite wavenumber instabilities. *New J. Phys.*, **6**, 5. 66

Bär, M. & Or-Guil, M. (1999). Alternative scenarios of spiral breakup in a reaction–diffusion model with excitable and oscillatory dynamics. *Phys. Rev. Lett.*, **82**, 1160–1163. 66

[BiophysikBildergalerie] (accessed 21 Mar 2014). Otto von Guericke University, Biophysik Bildergalerie. http://www.biophysik.ovgu.de/Forschung/Bildergalerie.html. vii, viii, 3, 52

Black, A.J. & McKane, A.J. (2012). Stochastic formulation of ecological models and their applications. *Trends in Ecology & Evolution*, **27**, 337–345. 12

Boccara, N., Roblin, O. & Roger, M. (1994). Automata network predator–prey model with pursuit and evasion. *Phys. Rev. E*, **50**, 4531–4541. 38

Boerlijst, M. & Hogeweg, P. (1991). Spiral wave structure in pre-biotic evolution: Hypercycles stable against parasites. *Physica D: Nonlinear Phenomena*, **48**, 17–28. viii, 13, 14

Boerlijst, M.C. & van Ballegooijen, W.M. (2010). Spatial pattern switching enables cyclic evolution in spatial epidemics. *PLoS Computional Biology*, **6**, e1001030. 4

Boon, J.P., Dab, D., Kapral, R. & Lawniczak, A. (1996). Lattice gas automata for reactive systems. *Physics Reports*, **273**, 55–147. 38

Cameron, D.D., White, A. & Antonovics, J. (2009). Parasite–grass–forb interactions and rock–paper–scissor dynamics: predicting the effects of the parasitic plant Rhinanthus minor on host plant communities. *J. Ecol.*, **97**, 1311–1319. 4

Cao, Y., Li, H. & Petzold, L. (2004). Efficient formulation of the stochastic simulation algorithm for chemically reacting systems. *J. Chem. Phys.*, **121**, 4059–4067. 39

Cardinale, B.J., Duffy, J.E., Gonzalez, A., Hooper, D.U., Perrings, C., Venail, P., Narwani, A., Mace, G.M., Tilman, D., Wardle, D.A., Kinzig, A.P., Daily, G.C., Loreau, M., Grace, J.B., Larigauderie, A., Srivastava, D.S. & Naeem, S. (2012). Biodiversity loss and its impact on humanity. *Nature*, **486**, 59–67. 3

Case, S.O., Durney, C.H., Pleimling, M. & Zia, R. (2010). Cyclic competition of four species: Mean–field theory and stochastic evolution. *EPL*, **92**, 58003. 40, 42

Chacon, S. & Hamano, J.C. (2009). *Pro git*. Springer. 49

Chapin III, F.S., Zavaleta, E.S., Eviner, V.T., Naylor, R.L., Vitousek, P.M., Reynolds, H.L., Hooper, D.U., Lavorel, S., Sala, O.E., Hobbie, S.E., Mack, M.C. & Díaz, S. (2000). Consequences of changing biodiversity. *Nature*, **405**, 234–242. 3

[ChemWiki] (accessed 21 Mar 2014). ChemWiki: The Dynamic Chemistry E-textbook, Chapter 14. Chemical Kinetics. http://chemwiki.ucdavis.edu/Under_Construction/Lardbucket/Chapter_14/14._Chemical_Kinetics. viii, 52

Chesson, P. (2000). Mechanisms of maintenance of species diversity. *Annual Review of Ecology and Systematics*, **31**, 343–366. 3

Claudia, C. & Carletti, T. (2014). Stochastic patterns in a 1D rock–paper–scissor model with mutation. *Preprint arXiv:1401.4302*. 83

Claussen, J.C. & Traulsen, A. (2008). Cyclic dominance and biodiversity in well–mixed populations. *Phys. Rev. Lett.*, **100**, 058104. 3

Corl, A., Davis, A.R., Kuchta, S.R. & Sinervo, B. (2010). Selective loss of polymorphic mating types is associated with rapid phenotypic evolution during morphic speciation. *PNAS*, **107**, 4254–4259. 4

Cox, S. & Matthews, P. (2002). Exponential time differencing for stiff systems. *J. Comp. Phys.*, **176**, 430–455. 9, 46

Cremer, J. (2008). MSc (Diploma) Thesis, Ludwig–Maximilians–Universität München. 7, 16, 17, 27, 32

Darwin, C. (1859). *On the Origin of Species by Means of Natural Selection, Or, The Preservation of Favoured Races in the Struggle for Life*. J. Murray. 2

Dawkins, R. (1989). *The Selfish Gene*. Oxford paperbacks, Oxford University Press. 3

Dickinson, J.L. & Koenig, W.D. (2003). Desperately seeking similarity. *Science*, **300**, 1887–1889. 4

REFERENCES

Droz, M. & Pekalski, A. (2004). Role of evolution by natural selection in population dynamics. *Phys. Rev. E*, **69**, 051912. 38

Dunn, R.R. (2005). Modern insect extinctions, the neglected majority. *Conservation Biology*, **19**, 1030–1036. 3

Durrett, R. (1999). Stochastic spatial models. *SIAM Review*, **41**, 677–718. 13

Durrett, R. & Levin, S. (1994). The importance of being discrete (and spatial). *Theoretical Population Biology*, **46**, 363–394. 12, 13

Durrett, R. & Levin, S. (1998). Spatial aspects of interspecific competition. *Theoretical Population Biology*, **53**, 30–43. 13

Elf, J. & Ehrenberg, M. (2004). Spontaneous separation of bi–stable biochemical systems into spatial domains of opposite phases. *Systems Biology, IEE Proceedings*, **1**, 230–236. 43

Erban, R., Chapman, J. & Maini, P. (2007). A practical guide to stochastic simulations of reaction–diffusion processes. *Preprint arXiv:0704.1908v2*. 39

Eriksson, A., Elías-Wolff, F. & Mehlig, B. (2013). Metapopulation dynamics on the brink of extinction. *Theoretical Population Biology*, **83**, 101–122. 13

Frey, E. (2010). Evolutionary game theory: Theoretical concepts and applications to microbial communities. *Physica A: Statistical Mechanics and its Applications*, **389**, 4265–4298. 7, 24, 26, 31, 32

Frigo, M. & Johnson, S.G. (1998). FFTW: An adaptive software architecture for the FFT. In *Acoustics, Speech and Signal Processing, 1998. Proceedings of the 1998 IEEE International Conference on*, vol. 3, 1381–1384, IEEE. 49

Frigo, M. & Johnson, S.G. (2005). The design and implementation of FFTW3. *Proceedings of the IEEE*, **93**, 216–231. 49

Gardiner, C. (1985). *Handbook of stochastic methods*. Springer Berlin. 8

Gibson, M.A. & Bruck, J. (2000). Efficient exact stochastic simulation of chemical systems with many species and many channels. *J. Phys. Chem. A*, **104**, 1876–1889. 39, 45

Gillespie, D.T. (1976). A general method for numerically simulating the stochastic time evolution of coupled chemical reactions. *J. Comp. Phys.*, **22**, 403–434. 9, 39

Gillespie, D.T. (2007). Stochastic simulation of chemical kinetics. *Annual Review of Physical Chemistry*, **58**, 35–55. 39, 40, 43

[GPLv2+] (accessed 11 Apr 2014). The GNU Public License, Version 2+. http://opensource.org/licenses/GPL-2.0. 49

Grimm, V. (1999). Ten years of individual–based modelling in ecology: what have we learned and what could we learn in the future? *Ecological Modelling*, **115**, 129–148. 12

Harper, J.L. & Hawksworth, D.L. (1994). Biodiversity: measurement and estimation. *Phil. Trans. R. Soc. B*, **345**, 5–12. 2

He, Q., Mobilia, M. & Tuber, U.C. (2010). Spatial rock–paper–scissors models with inhomogeneous reaction rates. *Phys. Rev. E*, **82**, 051909. 17

He, Q., Mobilia, M. & Tuber, U.C. (2011). Coexistence in the two–dimensional May–Leonard model with random rates. *Eur. Phys. J. B*, **82**, 97–105. 15, 16, 17, 77

Hearn, A.C. (2004). *REDUCE User's Manual Version 3.8*. Rand Corporation. 22, 30, 35

Heilmann, S., Sneppen, K. & Krishna, S. (2010). Sustainability of virulence in a phage–bacterial ecosystem. *J. Virol.*, **84**, 3016–3022. 4

Hibbing, M.E., Fuqua, C., Parsek, M.R. & Peterson, S.B. (2010). Bacterial competition: surviving and thriving in the microbial jungle. *Nature Reviews Microbiology*, **8**, 15–25. vii, 6

Hoyle, R. (2006). *Pattern Formation: An Introduction to Methods*. Cambridge texts in applied mathematics, Cambridge University Press. 8, 11, 33

Huberman, B.A. & Glance, N.S. (1993). Evolutionary games and computer simulations. *PNAS*, **90**, 7716–7718. 38

[HumonComics] (accessed 21 Mar 2014). Humon Comics, Animal Lives. http://humoncomics.com/archive/animal-lives. vii, 5

Ince, D.C., Hatton, L. & Graham-Cumming, J. (2012). The case for open computer programs. *Nature*, **482**, 485–488. 49

Jiang, L.L., Zhou, T., Perc, M.c.v. & Wang, B.H. (2011). Effects of competition on pattern formation in the rock–paper–scissors game. *Phys. Rev. E*, **84**, 021912. 7, 16, 76

Jiang, L.L., Wang, W.X., Lai, Y.C. & Ni, X. (2012). Multi–armed spirals and multi–pairs antispirals in spatial rock–paper–scissors games. *Phys. Lett. A*, **376**, 2292–2297. 7, 16

Joppa, L.N., McInerny, G., Harper, R., Salido, L., Takeda, K., OHara, K., Gavaghan, D. & Emmott, S. (2013). Troubling trends in scientific software use. *Science*, **340**, 814–815. 66

Kareiva, P., Mullen, A. & Southwood, R. (1990). Population dynamics in spatially complex environments: Theory and data [and discussion]. *Phil. Trans. R. Soc. B*, **330**, 175–190. 13

Kernighan, B.W., Ritchie, D.M. & Ejeklint, P. (1988). *The C Programming Language, 2nd Edition*. Prentice–Hall Englewood Cliffs. 49

Kerr, B., Riley, M.A., Feldman, M.W. & Bohannan, B.J.M. (2002). Local dispersal promotes biodiversity in a real–life game of rock–paper–scissors. *Nature*, **418**, 171–174. 4, 69

Kerr, B., Neuhauser, C., Bohannan, B.J.M. & Dean, A.M. (2006). Local migration promotes competitive restraint in a host–pathogen 'tragedy of the commons'. *Nature*, **442**, 75–78. xii, 4, 80, 81

Kirkup, B.C. & Riley, M.A. (2004). Antibiotic–mediated antagonism leads to a bacterial game of rock–paper–scissors in vivo. *Nature*, **428**, 412–414. 4

Knuth, D. (1968). *The Art of Computer Programming: Fundamental algorithms*. Addison-Wesley. 43

Koch, A. & Meinhardt, H. (1994). Biological pattern formation: from basic mechanisms to complex structures. *Rev. Mod. Phys.*, **66**, 1481. 13

Krebs, K., Pfannmller, M.P., Simon, H. & Wehefritz, B. (1995). Finite–size scaling studies of one–dimensional reaction–diffusion systems. part II. numerical methods. *J. Stat. Phys.*, **78**, 1471–1491. 40, 41, 42

Li, H. & Petzold, L. (2006). Logarithmic direct method for discrete stochastic simulation of chemically reacting systems. *Technical report; Department of Computer Science, University of California*. 39, 43

Lipowski, A. (1999). Oscillatory behavior in a lattice prey-predator system. *Phys. Rev. E*, **60**, 5179–5184. 38

Lipowski, A. & Lipowska, D. (2000). Nonequilibrium phase transition in a lattice prey–predator system. *Physica A: Statistical Mechanics and its Applications*, **276**, 456–464. 38

[LizardLand] (accessed 21 Mar 2014). Virtual Reality Exploration of Lizardland. http://bio.research.ucsc.edu/~barrylab/lizardland/male_lizards.overview.html. vii, 4

Lotka, A.J. (1920). Analytical note on certain rhythmic relations in organic systems. *PNAS*, **6**, 410–415. 12

Lugo, C.A. & McKane, A.J. (2008). Quasicycles in a spatial predator–prey model. *Phys. Rev. E*, **78**, 051911. 8, 14, 39

Mathiesen, J., Mitarai, N., Sneppen, K. & Trusina, A. (2011). Ecosystems with mutually exclusive interactions self–organize to a state of high diversity. *Phys. Rev. Lett.*, **107**, 188101. vii, 3, 4

May, R.M. & Leonard, W.J. (1975). Nonlinear aspects of competition between three species. **29**, 243–253. 3

McCafferty, D. (2010). Should code be released? *Communications of the ACM*, **53**, 16–17. 49

McKane, A.J. & Newman, T.J. (2004). Stochastic models in population biology and their deterministic analogs. *Phys. Rev. E*, **70**, 041902. 8, 12

McKane, A.J. & Newman, T.J. (2005). Predator–prey cycles from resonant amplification of demographic stochasticity. *Phys. Rev. Lett.*, **94**, 218102. 12, 39

McKane, A.J., Biancalani, T. & Rogers, T. (2013). Stochastic pattern formation and spontaneous polarisation: The linear noise approximation and beyond. *Bull. Math. Biol.*, 1–27. 39

Merali, Z. (2010). Computational science: Error, why scientific programming does not compute. *Nature*, **467**, 775–777. 66

Miller, P. (2006). *Applied Asymptotic Analysis*. Graduate studies in mathematics, American Mathematical Society. 8, 11, 27

[MIT] (accessed 11 Apr 2014). The MIT License. http://opensource.org/licenses/MIT. 49

Mobilia, M., Georgiev, I.T. & Tuber, U.C. (2007). Phase transitions and spatio–temporal fluctuations in stochastic lattice Lotka–Volterra models. *J. Stat. Phys.*, **128**, 447–483. 38

Morin, A., Urban, J. & Sliz, P. (2012). A quick guide to software licensing for the scientist–programmer. *PLoS Computational Biology*, **8**, e1002598. 49

Morlon, H. (2012). Microbial cooperative warfare. *Science*, **337**, 1184–1185. 4

Mowlaei, S., Roman, A. & Pleimling, M. (2014). Spirals and coarsening patterns in the competition of many species: a complex Ginzburg–Landau approach. *J. Phys. A: Mathematical and Theoretical*, **47**, 165001. 83

Myers, N., Mittermeier, R.A., Mittermeier, C.G., da Fonseca, G.A.B. & Kent, J. (2000). Biodiversity hotspots for conservation priorities. *Nature*, **403**, 853–858. 3

Nahum, J.R., Harding, B.N. & Kerr, B. (2011). Evolution of restraint in a structured rock–paper–scissors community. *PNAS*, **108**, 10831–10838. 4

Ni, X., Wang, W.X., Lai, Y.C. & Grebogi, C. (2010). Cyclic competition of mobile species on continuous space: Pattern formation and coexistence. *Phys. Rev. E*, **82**, 066211. 14

Nowak, M.A. & May, R.M. (1992). Evolutionary games and spatial chaos. *Nature*, **359**, 826–829. 38

Nowak, M.A. & Sigmund, K. (2002). Biodiversity: Bacterial game dynamics. *Nature*, **418**, 138–139. 4

Nowak, M.A., Bonhoeffer, S. & May, R.M. (1994). Spatial games and the maintenance of cooperation. *PNAS*, **91**, 4877–4881. 38

Orszag, S.A. (1971). On the elimination of aliasing in finite–difference schemes by filtering high–wavenumber components. *Journal of the Atmospheric Sciences*, **28**, 1074–1074. 48

Ouyang, Q. & Flesselles, J.M. (1996). Transition from spirals to defect turbulence driven by a convective instability. *Nature*, **379**, 143–146. 66

Pálsson, E. & Cox, E.C. (1996). Origin and evolution of circular waves and spirals in dictyostelium discoideum territories. *PNAS*, **93**, 1151–1155. 51

Pálsson, E., Lee, K.J., Goldstein, R.E., Franke, J., Kessin, R.H. & Cox, E.C. (1997). Selection for spiral waves in the social amoebae dictyostelium. *PNAS*, **94**, 13719–13723. 51

Pekalski, A. (2004). A short guide to predator–prey lattice models. *Computing in Science Engineering*, **6**, 62–66. 38

REFERENCES

Peltomäki, M. & Alava, M. (2008). Three– and four–state rock–paper–scissors games with diffusion. *Phys. Rev. E*, **78**, 031906. 7, 16

Pennisi, E. (2005). What determines species diversity? *Science*, **309**, 90–90. 1

Phillips, N.A. (1959). An example of non-linear computational instability. *The Atmosphere and the Sea in Motion*, 501–504. 48

Press, W., Teukolsky, S., Vetterling, W. & Flannery, B.P. (2007). *Numerical Recipes 3rd Edition: The Art of Scientific Computing*. Cambridge University Press. 47

Prlić, A. & Procter, J.B. (2012). Ten simple rules for the open development of scientific software. *PLoS Computational Biology*, **8**, e1002802. 49

Provata, A., Nicolis, G. & Baras, F. (1999). Oscillatory dynamics in low-dimensional supports: A lattice Lotka–Volterra model. *J. Chem. Phys.*, **110**, 8361–8368. 38

Reichenbach, T. & Frey, E. (2008). Instability of spatial patterns and its ambiguous impact on species diversity. *Phys. Rev. Lett.*, **101**, 058102. 7, 16, 17, 32, 75

Reichenbach, T., Mobilia, M. & Frey, E. (2007a). Mobility promotes and jeopardizes biodiversity in rock–paper–scissors games. *Nature*, **448**, 1046–1049. 7, 12, 13, 16, 17, 73

Reichenbach, T., Mobilia, M. & Frey, E. (2007b). Noise and correlations in a spatial population model with cyclic competition. *Phys. Rev. Lett.*, **99**, 238105. 7, 16, 31, 32

Reichenbach, T., Mobilia, M. & Frey, E. (2008). Self–organization of mobile populations in cyclic competition. *Journal of Theoretical Biology*, **254**, 368–383. 7, 16, 22, 26, 31, 32

Reichl, L. (2009). *A modern course in statistical physics*. Wiley-VCH. 17

Roberts, E., Stone, J.E. & Luthey-Schulten, Z. (2013). Lattice microbes: High–performance stochastic simulation method for the reaction–diffusion master equation. *J. Comp. Chem.*, **34**, 245–255. 39

Rozenfeld, A. & Albano, E. (1999). Study of a lattice gas model for a prey–predator system. *Physica A: Statistical Mechanics and its Applications*, **266**, 322–329. 38

Rulands, S., Reichenbach, T. & Frey, E. (2011). Threefold way to extinction in populations of cyclically competing species. *J. Stat. Mech.*, **2011**, L01003. 17

Rulands, S., Zielinski, A. & Frey, E. (2013). Global attractors and extinction dynamics of cyclically competing species. *Phys. Rev. E*, **87**, 052710. xi, 7, 16, 17, 27, 75

Satulovsky, J.E. & Tom, T. (1994). Stochastic lattice gas model for a predator–prey system. *Phys. Rev. E*, **49**, 5073–5079. 38

Sinervo, B. & Lively, C.M. (1996). The rock–paper–scissors game and the evolution of alternative male strategies. *Nature*, **380**, 240–243. 4

Sinervo, B., Miles, D.B., Frankino, W.A., Klukowski, M. & DeNardo, D.F. (2000). Testosterone, endurance, and Darwinian fitness: natural and sexual selection on the physiological bases of alternative male behaviors in side-blotched lizards. *Hormones and Behavior*, **38**, 222–233. 4

Smith, J.M. (1996). The games lizards play. *Nature*, **380**, 198–199. 4

Smolka, L.B., Marts, B. & Lin, A.L. (2005). Effect of inhomogeneities on spiral wave dynamics in the Belousov–Zhabotinsky reaction. *Phys. Rev. E*, **72**, 056205. 51

Szczesny, B., Mobilia, M. & Rucklidge, A.M. (2012). Supplementary material: When does cyclic dominance lead to stable spiral waves? Figshare, http://dx.doi.org/10.6084/m9.figshare.96949. 7, 67, 69, 76, 77, 79

Szczesny, B., Mobilia, M. & Rucklidge, A.M. (2013). When does cyclic dominance lead to stable spiral waves? *EPL*, **102**, 28012. xv, 7, 16

Szczesny, B., Mobilia, M. & Rucklidge, A.M. (2014). Characterization of spiraling patterns in spatial rock–paper–scissors games. *Phys. Rev. E*, **90**, 032704. xv, 7, 16

Szolnoki, A., Mobilia, M., Jiang, L.L., Szczesny, B., Rucklidge, A.M. & Perc, M. (2014). Cyclic dominance in evolutionary games: A review. *Journal of Royal Society Interface (accepted)*. 7, 83

Traulsen, A., Claussen, J. & Hauert, C. (2005). Coevolutionary dynamics: from finite to infinite populations. *Phys. Rev. Lett.*, **95**, 238701. 12, 39

Twomey, A. (2007). *On the stochastic modelling of reaction–diffusion processes*. PhD Thesis, University of Oxford. 39

Tyson, J.J. & Murray, J.D. (1989). Cyclic AMP waves during aggregation of dictyostelium amoebae. *Development*, **106**, 421–426. 51

Van Kampen, N. (2007). *Stochastic Processes in Physics and Chemistry, (North-Holland Personal Library)*. North Holland. 8, 11, 12, 17, 19

van Saarloos, W. (2003). Front propagation into unstable states. *Physics Reports*, **386**, 29–222. viii, 8, 31, 32

Volterra, V. (1926). Fluctuations in the abundance of a species considered mathematically. *Nature*, **118**, 558–560. 12

Volterra, V. (1928). Variations and fluctuations of the number of individuals in animal species living together. *J. Cons. Int. Explor. Mer.*, **3**, 3–51. 12

Washenberger, M.J., Mobilia, M. & Tuber, U.C. (2007). Influence of local carrying capacity restrictions on stochastic predator–prey models. *J. Phys.: Condensed Matter*, **19**, 065139. 38

Weber, A., Kramer, L., Aranson, I. & Aranson, L. (1992). Stability limits of traveling waves and the transition to spatio–temporal chaos in the complex Ginzburg–Landau equation. *Physica D: Nonlinear Phenomena*, **61**, 279–283. 30, 35

Wilson, G., Aruliah, D.A., Brown, C.T., Chue Hong, N.P., Davis, M., Guy, R.T., Haddock, S.H.D., Huff, K.D., Mitchell, I.M., Plumbley, M.D., Waugh, B., White, E.P. & Wilson, P. (2014). Best practices for scientific computing. *PLoS Biology*, **12**, e1001745. 49

Wodarz, D., Hofacre, A., Lau, J.W., Sun, Z., Fan, H. & Komarova, N.L. (2012). Complex spatial dynamics of oncolytic viruses in vitro: Mathematical and experimental approaches. *PLoS Computational Biology*, **8**, e1002547. 39

Zaikin, A.N. & Zhabotinsky, A.M. (1970). Concentration wave propagation in two–dimensional liquid–phase self–oscillating system. *Nature*, **225**, 535–537. 51

Zamudio, K.R. & Sinervo, B. (2000). Polygyny, mate–guarding, and posthumous fertilization as alternative male mating strategies. *PNAS*, **97**, 14427–14432. 4

Ziff, R.M., Gulari, E. & Barshad, Y. (1986). Kinetic phase transitions in an irreversible surface–reaction model. *Phys. Rev. Lett.*, **56**, 2553–2556. 38